Functional Mapping of Three-Dimensional Electrical Activation in Ventricles

A DISSERTATION
SUBMITTED TO THE FACULTY OF THE GRADUATE SCHOOL
OF THE UNIVERSITY OF MINNESOTA
BY

Chenguang Liu

IN PARTIAL FULFILLMENT OF THE REQUIREMENTS
FOR THE DEGREE OF
DOCTOR OF PHILOSOPHY

Advisor
Dr. Bin He

February, 2010

Acknowledgements

I would like to express my sincere thanks to my advisor, Dr. Bin He, for his great guidance and help on every aspect of my PhD study. It is his consistent support and encouragement that help me make steady progress in research. I appreciate both strict training and warmest kindness received from Dr. He.

I also would like to thank Dr. Paul Iaizzo, who collaborated on animal studies with us. His enthusiasm on research and outstanding expertise are of great value to the success of animal studies, and I have learned a lot of useful knowledge from him. I also kindly thank the other members of my dissertation committee, Dr. Emad Ebbini and Dr. Alena Talkachova, for their time, support and valuable comments.

I would like to acknowledge many collaborators: Dr. Cory Swingen, Dr. Nicholas Skadsberg, Dr. Sarah Ahlberg, Dr. Michael Eggen, Dr. Jason Quill, Mr. Michael Bateman and Mr. Bill Gallagher for collaborating in animal studies.

I appreciate all the help on my thesis research from many lab colleagues. I would like to thank: Dr. Xin Zhang for his guidance and help in data acquisition/analysis in the early stage of my PhD study; Dr. Yingchun Zhang for his help on finite element method; Dr. Zhongming Liu for the help in animal experiments and a lot of useful discussions; Mr. Chengzong Han for great help in animal studies and discussions; Dr. Christopher Wilke and Dr. Dakun Lai for the help in animal studies. It has been my pleasure to work with those outstanding researchers in the Biomedical Functional Imaging and Neuroengineering Laboratory at the University of Minnesota.

Abstract

Ventricular arrhythmias account for nearly 400,000 deaths per year in the United States alone. Electrical mapping of the ventricular activation could facilitate the diagnosis and treatment of arrhythmias, e.g. guiding catheter ablation. To date, both direct mapping and non-contact mapping techniques have been routinely used in electrophysiology labs for obtaining the electrical activity on the endocardial surface. Non-invasive functional mapping methods are also developed to estimate the electrical activity on the epicardium or on both epicardium and endocardium from the body surface measurements. Though successful, the results using above methods are all limited on the surface of the heart and thus cannot directly characterize the cardiac events originating within the myocardial wall.

Our group's goal is to develop a functional mapping method to estimate the three-dimensional cardiac electrical activity from either non-invasive body surface potential maps or minimally-invasive intracavitary potential maps, by solving the so-called "inverse problem". Hence the information under the surface of the heart could be revealed to better characterize the cardiac activation. In the present thesis study, the previously developed three-dimensional cardiac electrical imaging (3DCEI) approach has been further investigated. Its function is expanded for not only estimating the global activation sequence but also reconstructing the potential at any myocardial site throughout the ventricle. New algorithms under the 3DCEI scheme are also explored for more powerful mapping capability. The performance of the enhanced 3DCEI approach is rigorously evaluated in both control and diseased swine models when the clinical settings

are mimicked. The promising results validate the feasibility of estimating detailed three-dimensional cardiac activation by using the 3DCEI approach, and suggest that 3DCEI has great potential of guiding the clinical management of cardiac arrhythmias in a more efficient way.

Table of Contents

List of Tables

List of Figures

List of Abbreviations

2D	Two-dimensional
3D	Three-dimensional
3DCEI	Three-dimensional cardiac electrical imaging
ANN	Artificial neural network
AP	Action potential
AS	Activation sequence
BE	Boundary element
BEM	Boundary element method
BR	Beeler-Reuter
BSPM	Body surface potential map
CC	Correlation coefficient
CT	Computed tomography
DT-MRI	Diffusion tensor magnetic resonance imaging
ECG, EKG	Electrocardiogram
EG	Electrogram
EKF	Extended Kalman filter
EP	Electrophysiology
FE	Finite element
FEM	Finite element method
GWN	Gaussian white noise
HF	Heart failure
ICPM	Intracavitary potential map
IS	Initiation site
KF	Kalman filter
LE	Localization error
LV	Left ventricle
LVA	Left ventricular apex
LVAn	Left ventricular anterior
LVLL	Left ventricular lower lateral

LVML	Left ventricular middle lateral
LWMN	Laplacian weighted minimal norm
MEA	Multi-electrode array
MR	Magnetic resonance
MRI	Magnetic resonance imaging
NCM	Non-contact mapping
NMZ	Necrotic myocardial zone
NURBS	Non-Uniform Rational B-Splines
RV	Right ventricle
RVA	Right ventricular apex
RVS	Right ventricular septum
SNR	Signal-to-noise ratio
TSVD	Truncated singular-value decomposition
UDB	Unidirectional block
VT	Ventricular tachycardia
WPW	Wolff-Parkinson-white

1. Introduction

1.1. Overview

Heart disease is the No. 1 killer in the world including the United States. For example, ventricular arrhythmias account for nearly 400,000 deaths per year in the United States alone [Myerburg et al 1993]. Management of the cardiac arrhythmias has long been a hot topic. The heart's activity is based on the electrical excitation of the cardiac cells, so the abnormal cardiac activities can be reflected in the electrical signals originating from the heart. Monitoring the electrical signal from the heart is critical for both diagnosing heart diseases and guiding the treatments to the arrhythmias. The easiest and most convenient monitoring method is recording the electrocardiogram (ECG, or EKG). ECG is the electrical potential over time which originates from the heart and are noninvasively captured on the human body. The standard 12-lead ECG is the most popular ECG recording method for representing the cardiac activities and diagnosing heart diseases. Since the ECG signals are smoothed and distorted when traveling from the heart to the surface, useful information may be smeared. In order to obtain meaningful electrical signals from the heart, people have applied invasive methods to record the electrograms (EG) on the epicardium, on the endocardium, inside the blood cavity or even from the intramural myocardium. If we could evenly put multiple electrical sensors on the heart's surface and inside the myocardium, the detailed spatial-temporal pattern of the electrical activity would be quantitatively characterized, which would be of great value for managing cardiac arrhythmias and more useful than single-channel recording. Unfortunately, such an invasive multi-electrode array is unrealistic in current clinical

application. On the other hand, a multi-electrode array can be easily put on the body surface. The development of the catheter technique also allows us to put a noncontact multi-electrode array inside the heart chamber in a minimally-invasive way. The signal recorded by each electrode from either the body surface array or the noncontact intracavitary array is the summation of the distorted source signals. The source signals inside the heart travel through the volume conductor and reach the recording sensors. Based on this knowledge, the following idea has been raised for decades: can we reconstruct the cardiac sources from the recordings in the volume conductor field?

Motivated by this goal, the cardiac inverse problem has been proposed and solved. In the inverse problem, people want to estimate the cardiac sources -- the generator of the

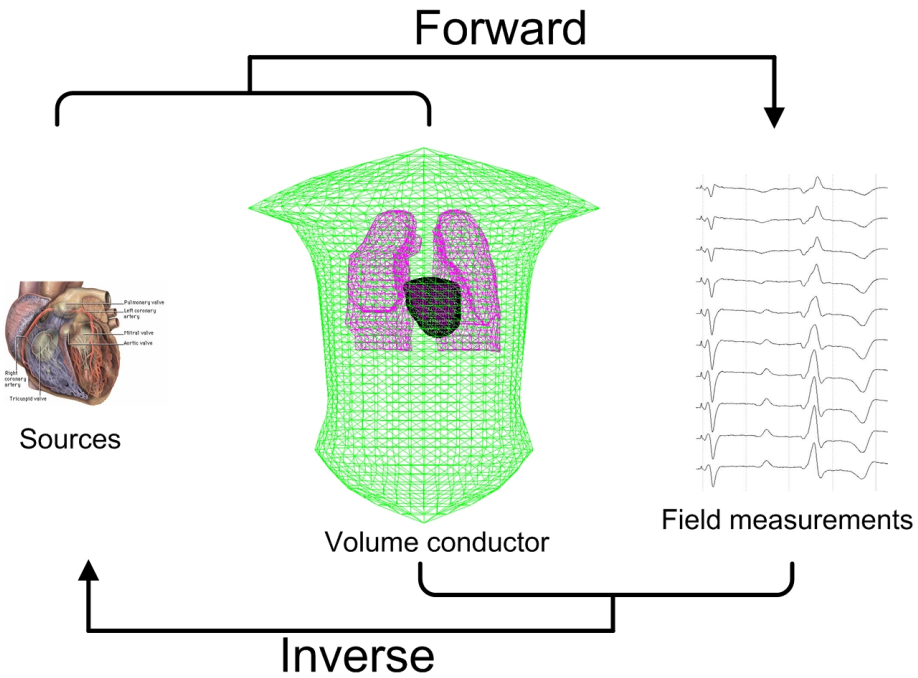

Figure 1.1. Schematic diagram of the forward/inverse problem

field potentials -- from the recorded field measurements (either on body surface or intracavitary) and the modeled volume conductor. The basis of the inverse problem is the

forward problem, where the field measurements are simulated from the known cardiac sources and the volume conductor model by solving the governing mathematical equations. In other words, the forward modeling must be completed before applying the inverse approach. The idea of forward/inverse problem is illustrated in Figure 1.1.

1.2. Specific aims

To date, many cardiac source models and inverse algorithms have been developed, which will be reviewed in Chapter 2. Our laboratory has rigorously investigated the three-dimensional cardiac electrical imaging (3DCEI) approach. A heart-model-based algorithm [He et al 2002] was previously proposed to noninvasively estimate the three-dimensional activation sequence from body surface potential maps (BSPMs) and this approach was validated in a rabbit model [Zhang et al 2005]. The specific aims of this dissertation project are as follows:

Aim 1: Evaluate the BSPM-based three-dimensional activation sequence imaging approach in large mammalian animals mimicking the clinical settings.

Aim 2: Refine and explore the heart-model-based algorithm, including 1) developing the algorithm for localizing the origin of reentry in a heart model; 2) exploring the method of estimating the cardiac intramural potentials using advanced numerical calculation.

Aim 3: Apply the modified 3DCEI approach to localize the origin of activation, estimate the global activation sequence and image the 3D intramural potentials from the

intracavitary potential maps (ICPMs) recorded by a noncontact multi-electrode array, and evaluate this method in large animals.

Aim 4: Develop a novel algorithm which is based on the extended Kalman filter to noninvasively image the 3D activation sequence.

1.3. Scope of the dissertation

In chapter 2, a review of the cardiac inverse methods is presented. The input of the inverse problem includes the BSPMs and ICPMs. The inversely estimated cardiac source includes the moving dipole(s), epicardial potentials, heart surface activation sequence, three-dimensional current densities and three-dimensional activation sequence. For each algorithm, the principle and merits are introduced.

In chapter 3, an animal study on a swine model is conducted to validate the heart-model-based 3DCEI approach, where the input is the body surface potentials. The estimated initiation of cardiac activation, as well as global cardiac activation sequences, are evaluated with the aid of the MRI scanning and the Ensite noncontact mapping system. Promising results are reported.

In chapter 4, a model study on simulating reentry and noninvasively estimating the origin of reentry is presented. An ion-channel-level cardiac model is employed, and reentry and corresponding ECG signals are successfully simulated. After applying the principle of the 3DCEI approach, the origin of reentry is accurately localized in simulation.

In chapter 5, the finite element method (FEM) is developed and used in the 3DCEI approach. The principle and technical details of FEM are introduced. The new function of estimating the cardiac intramural potentials by using FEM is incorporated into 3DCEI.

In chapter 6, the 3DCEI approach is modified to use ICPMs as input instead of BSPMs. This novel idea is rigorously evaluated in simulation, and then validated in experiments on a swine model. The functions of 3DCEI are rigorously validated, including estimating the intramural potentials by comparing to the output of the Ensite system. The characteristics of the ICPM-based 3DCEI approach are discussed.

In chapter 7, a new algorithm for estimating the 3D activation sequence from BSPMs is developed. The core operator of the proposed algorithm is the extended Kalman filter. This algorithm is evaluated in a series of simulation studies. The advantage of the new algorithm is discussed according to the simulation results.

In chapter 8, the contributions made in this dissertation are summarized. The scientific value of the present studies and the direction of research in the future are further discussed.

2. Background of cardiac inverse problem

In this chapter, the development of the cardiac inverse problem is reviewed. For decades, BSPM-based inverse problem has drawn a lot of attention because of its convenience and low cost. In recent years, ICPM-based inverse approaches have been investigated, owing to the improvement of the catheter technology. In general, the algorithms used in the ICPM-based approaches are also used in the BSPM-based approaches. So the review will first focus on the BSPM-based approaches, and the ICPM-based approaches will be introduced after that.

The reconstructed electrical sources could be in different configurations, as long as it can sufficiently represent the corresponding cardiac activity and has clear physiological meaning. The sources could be either focal or distributed. With the aim of extracting useful information regarding cardiac electrical activity, focal sources, such as equivalent moving dipole(s) [Mirvis et al 1977; Savard et al 1980; Okamoto et al 1983; Gulrajani et al 1984; Armoundas et al 2003], are reasonable approximation of the electrical sources in certain cases. On the other hand, distributed sources have gained more attention, because more meaningful electrophysiological information can possibly be disclosed. In the sense of spatially characterizing the distributed cardiac properties, the term "imaging" is conveniently used. A main trend of imaging distributed sources is restricting the sources on the heart surfaces. In the past decades, many efforts have been put on the inverse imaging of the epicardial potentials from measured BSPMs [Barr and Spach 1978; Shahidi et al 1994; Oster et al 1997; Greensite and Huiskamp 1998; Ramanathan et al 2004]. Seeking the activation sequence on the heart surfaces (both epicardium and

endocardium) from measured BSPMs is another important heart surface inverse approach [Cuppen and Oosterom 1984; Huiskamp and Greensite 1997, Tilg et al 2002]. The ICPM-based approaches have been reported to image the endocardial potentials[Khoury et al 1995, Schilling et al 1998; Gornick et al 1999; Berrier et al 2004]. Estimation of a limited number of dipoles in the 3D space has been reported in an early work [Barber and Fischman 1961], in which each dipole represents equivalent cardiac activity of a region. The idea of imaging three-dimensional (3D) cardiac distributed electrical sources has been proposed and rigorously pursued by He and coworkers. A 3D inverse approach was investigated to reconstruct the 3D equivalent current densities with a physical model [He and Wu 2001]. Global activation sequence imaging has been proposed by utilizing a heart model or physical model [He et al 2002, Liu et al 2006b].

Solving the inverse problem needs to tackle inherent mathematical and theoretical difficulties. The inverse problem does not possess a mathematically unique solution, because the electric field that the primary cardiac sources generate outside the closed heart surface can be duplicated by other equivalent sources, e.g. the double-layer dipole sources on the closed surface. In other words, different configurations of the cardiac sources may result in the same ECG signals. In order to obtain unique solutions, source models with implicit constraints have been introduced to represent the cardiac activity, such as equivalent dipoles and multipoles, epicardial potential, heart surface isochrone and excitable heart model with embedded physiological knowledge.

Another difficulty to be solved is the ill-posed nature of the inverse problem, which is due to the smoothing and attenuation effects inside the torso volume. This is because that human body is a very complex conductor. Some tissues, such as blood and muscle, are highly conductive; on the other hand, lungs, fat and bone are poor conductor for electrical signals. As results, the cardiac electrical signals are smoothed and attenuated when travelling through the volume conductor, and the distorted signals are eventually recorded on the body surface. These effects cause that the inverse solution is ill-posed and unstable. A slight measurement noise could induce large perturbation on the inverse solution. Specifically, the ill-posedness is more severe in distributed-source inverse problems, because the number of parameters in the solutions is much more than that in the focal-model inverse problems (such as single moving dipole or two moving dipoles). To overcome the ill-posedness, regularization methods or further constraints are required to obtain stable and meaningful inverse solution.

In the following sections, the representative inverse methods are introduced in details.

2.1. Moving dipole(s) source imaging

Certain cardiac electrical activities, such as ectopic beats, can be represented reasonably by one or two moving dipoles. An electric dipole is a separation of positive and negative charge, which can be characterized by a vector. Electrical activity produced by excitable cardiac media may be modeled by a combination of current dipoles, where a current dipole is a separation of current source and sink which is located in the vicinity to

the current source. The location, direction and magnitude of a current dipole (or dipoles) reflects the characteristics of cardiac electrical activity in an equivalent sense that the dipole(s) generated BSPM represents well the BSPM measured over a subject's torso surface. Notably, this representation is appropriate only when the cardiac activity has one or two centers, so that the characteristics of the underlying sources can be instant-by-instant tracked by estimating the location, magnitude and direction of the one or two moving dipoles inside the volume. For instance, the accessory pathway of the Wolff-Parkinson-white (WPW) syndrome can be tracked with the single-moving-dipole inverse solution. In this syndrome, an accessory pathway exists between the atria and ventricles, which results in the pre-excitation of the ventricles. The single-moving-dipole solutions may contribute to localizing the pathway during the early pre-excitation period. Besides, the moving-dipole solutions are also useful for localizing and tracking the migration of excitation during ectopic beats [Ideker et al 1977].

The mathematical principle of solving the moving-dipole inverse problem is to match the measured body surface potentials with those generated with the moving dipole(s) in the forward model. By adjusting the location, magnitude and orientation of the dipole(s), the dissimilarity between the measured and simulated body surface potentials is minimized. The dissimilarity can be quantified as follows:

$$R = \left\| \hat{V} - V \right\|^2 \tag{2.1}$$

$$V = AX \tag{2.2}$$

where $\hat{V}$ is the vector of the measured body surface potentials at one sampling instant, V is the simulated body surface potentials from the dipole(s) within a given volume conductor, $\| \|^2$ denotes the square of the Euclidean norm of a vector referring to the difference between the measured and model-predicted body surface potentials, X is the vector containing the unknown parameters of the moving-dipole inverse solution, and A is the transfer matrix relating the dipole sources to the body surface potentials. For a single-dipole model, the unknown parameters include three components of the dipole moment and three coordinates of the dipole location. For a two-moving-dipole model, the number of independent unknowns becomes 12. Notably, the relation between the simulated body surface potentials and the coordinates of a dipole is nonlinear. In an effort of minimizing equation (2.1), iterative methods are employed to solve this nonlinear optimization problem, such as the Levenberg-Marquardt algorithm [Gulrajani et al 1984]. The number of assumed moving dipoles depends on the number of excitation centers that need to be represented, normally no more than two, due to the sensitivity to measurement noise. [Okamoto et al 1983].

2.2. Heart surface distributed source imaging

2.2.1. Epicardial potential imaging

Noninvasive imaging of the epicardial potentials from body surface potentials is attractive for its potential clinical application. Intra-operative epicardial mapping has been conducted and proved useful for diagnosing cardiac arrhythmias and guiding intervention procedure [Parson et al 1984]. To overcome the extra cost and the inaccessibility to some patients, the noninvasive mapping method is desired as the

substitute of the invasive approach. The noninvasive imaging of the epicardial potentials has the potential of 1) diagnosing the mechanism of arrhythmias; 2) localizing the arrhythmogenic substrate to guide intervention, e.g. catheter ablation; 3) imaging the electrophysiological characteristics of normal/abnormal cardiac activities for clinical treatments and research, e.g. assist cardiac resynchronization therapy on patients with heart failure [Jia et al 2006]; 4) studying the activity of an intact heart without any affection, for instance, anesthesia.

In late 1970's it was demonstrated that the epicardial potentials and the body surface potentials can be related using a linear model with the aid of boundary element method, which can be used to incorporate realistic geometry of a subject [Barr et al 1977]. The mathematical equation can be represented as

$$V_B = AV_H \tag{2.3}$$

where V_B is an N x 1 column matrix containing the array of the body surface potentials, V_H is an M x 1 column matrix containing the array of the distributed epicardial potentials and A is an N x M linear transfer matrix. Usually M is larger than N.

Due to the large number of epicardial potentials in a distributed source model and the effect of the volume conductor, the inverse problem becomes very ill-posed, which means that a slight measurement noise may cause big disturbance on inverse solutions. Furthermore, the solution is usually non-unique and constraints need to be imposed. To

date, many refined techniques have been proposed, including truncated singular-value decomposition (TSVD) and Tikhonov regularization.

In brief, truncated singular-value decomposition removes the content which is sensitive to noise in transfer matrix A to obtain stable solutions. The TSVD approach is relatively simple and costs less computation load, but some details may be lost when using this method. Tikhonov regularization is a more advanced method. The Tikhonov regularization scheme minimizes the following equation:

$$\left\|\hat{V}_B - AV_H\right\|^2 + \lambda\left\|RV_H\right\|^2 \qquad (2.4)$$

where the first part is the norm of the residue, and the second part is the regularized norm of the inversely estimated epicardial potentials. By minimizing the two parts simultaneously, informative and stable solution is expected to be obtained. The balance between the two parts is determined by the regularization parameter λ. If λ is very small, the solution under Tikhonov regularization tends to approach the minimum-residual solution, and the solution would be unstable and very sensitive to the noise. If λ is large enough, stable solution will be obtained. But a too large λ value can make the solution overly smooth, because such the second part in equation (2.4) will dominate. So picking up a proper value of λ is critical for a stable and not excessively smooth solution. In order to find the best value of λ, the "L-curve" method is widely used [Hansen 1992].

Noninvasive epicardial potential imaging technique has been extensively investigated and validated in animal studies [Oster et al 1997], in normal human subjects

[Ramanathan et al 2006] and in patients with heart diseases [Ramanathan et al 2004; Jia et al 2006].

2.2.2. Heart surface isochrone imaging

Since the 1980's, parallel to the epicardial potential imaging, heart surface activation imaging has been pursued [Cuppen et al 1984], where the spatial distribution of activation time over the entire heart surface is reconstructed from the BSPM. Here the heart surface includes both the epicardium and the endocardium, and they form a closed heart volume in which the excitation happens. While the principle applies to both the ventricles and atria [Tilg et al 2002], most work has been dealing with imaging activation times over the surfaces of ventricles, including the endocardium and epicardium of the ventricles. Heart surface activation imaging is a promising tool for evaluating heart function in that it directly images electrophysiological properties of the heart (i.e. activation time), albeit on the surface of heart. Recent work has suggested its potential for clinical applications in assisting the diagnosis of cardiac abnormalities, such as Wolff-Parkinson-White syndrome [Berger et al 2006], bundle branch block [Fischer 2009] and ventricular tachyarrhythmias [Berger et al 2006].

Regarding the inverse problem, the source model is again constrained on the heart surface. In order to find the activation time at critical locations on the heart surface, the so-called "critical points" theory [Greensite 1995] has been used. The "critical points" are defined as the extrema sites (minima, maxima and saddle points, etc) on the heart surface activation map. The happening of the critical points will result in a changed slope in the

temporal time course of ECG, leading to a “jump” in the first derivative of the ECG time course corresponding to the activation time at critical points. By applying this principle, the critical points can be localized and the activation time at those critical points are determined by picking up the time instant when the "jump" happens [Huiskamp and Greensite 1997]. The activation times at the detected critical points are then used to determine the activation time distribution over the heart surface.

More recently, another heart surface activation imaging algorithm has been proposed by Tilg and co-workers [Tilg et al 2002]. In their method, building up the forward relation between the heart surface isochrone and the body surface potentials includes two steps. First, based on the bidomain theory, a linear relation between the heart surface transmembrane potentials and the body surface potentials exists [Geselowitz and Miller 1983]. Second, the nonlinear relation between the transmembrane potential and activation time at each heart surface source point is modeled with *a priori* physiological knowledge. By combining those two steps, a nonlinear relation between the activation time τ and the body surface potentials can be obtained as follows,

$$V_B = F\tau \tag{2.5}$$

where F is a nonlinear operator, τ contains the activation time on the heart surface and V_B is an N x N_t matrix containing the body surface potentials from N sensors at N_t time instants. To solve this nonlinear and ill-posed inverse problem, it is linearized by utilizing the derivative of F and then an iterative procedure is employed to update the value of τ in each step [Tilg et al 2002]. Notably, due to the nature of the linearization method, the

initial estimation of τ should be close to the real value to ensure the convergence and accuracy of the final solution. For instance, the activation time obtained with the "critical points" theory could be used as the initial value in the current iterative approach.

This approach has been evaluated on the patients under sinus rhythm [Tilg et al 2002] and under WPW syndrome [Berger et al 2006]. Promising results were reported.

2.3. Endocardial inverse solutions

Endocardial inverse imaging utilizes the intracavitary potential maps (ICPMs) recorded by a multi-electrode array (MEA) inside the heart chamber to estimate the potentials on the endocardial surface. Compared to the BSPM-based source imaging technique, endocardial inverse imaging has two significant advantages [Greensite 2004]. First, the recording electrodes are relatively close to the sources to be imaged (compared to the distance between the body surface and the epicardium), and so more details revealing the cardiac activities are expected to be recorded. Second, the volume between the electrodes and the sources is composed only of blood (opposed to multiple types of tissue/material between body surface and epicardium), and so the geometrical modeling becomes simple and less modeling error may exist in the transfer matrix.

The algorithms employed in the endocardial potential imaging are very similar with that used in epicardial potential imaging. A linear relationship is also set up as shown in equation (2.3) and then the algorithms introduced for epicardial potential imaging can be used on endocardial potential imaging. Pilot animal studies have been conducted [Khoury et al 1995, 1998]. The most impressive work was done on the Ensite® system (St Jude

Medical, Inc.). They developed an expandable a multi-electrode array (MEA) on a balloon catheter, applied the inverse approach and commercialized the entire system [Schilling et al 1998; Gornick et al 1999]. The Ensite system can image the endocardial potentials and the subsequent activation sequence from the MEA's recordings. It has been widely used in electrophysiological (EP) labs to assist diagnosing and treating heart diseases, e.g. guiding radiofrequency catheter ablation.

2.4. Three-dimensional cardiac source imaging

The real heart excitation propagates throughout the three dimensional (3D) space. Though successful, the heart surface inverse mapping approaches have limitation on characterizing intramural activities, e.g. intramural delay [Avari et al 2008]. As such, the 3D imaging of the intramural cardiac activation is expected to provide important pathoanatomic information: for example, ventricular arrhythmias may arise from transmural regions within the myocardial tissue. 3D mapping of cardiac activities could not only be a powerful tool for research on the mechanisms of arrhythmias but could also guide the clinical management of cardiac arrhythmias in a more efficient way.

The goal of 3D source inverse imaging is exciting, but it is more challenging than heart surface inverse problem. Recently, new 3D inverse methods have been investigated including imaging the distributed 3D dipoles with Laplacian weighted minimal norm (LWMN), the heart-model-based 3D cardiac source imaging and the physical-model-based 3D activation sequence imaging.

2.4.1. Inverse estimation of 3D dipole distribution

The first reported work on 3D cardiac electric imaging is with regard to the estimation of current dipole distributions [He & Wu, 2001]. The equivalent current dipoles are evenly distributed in the myocardium, and such the current density is approximated by the moment of the current dipoles. The forward relationship between the distributed dipoles and the body surface potentials is linearly modeled with the bidomain theory. This problem is under-estimated and ill-posed. The minimal-norm solution is prone to be biased and irregular, and advanced regularization method is required. In this sense, He and Wu have proposed to use Laplacian weighted minimal norm (LWMN) to tackle this challenging problem [He and Wu 2001]. In LWMN the Laplacian of the source signal is minimized in order to obtain an estimate. It can be anticipated that such 3D inverse solution is fairly smooth over the space. He and Wu used further an iterative approach to enhance the sources with large energy concentration, and showed reasonable results to localizing and imaging of focal sources.

2.4.2. Heart-model-based 3D activation sequence imaging

A possible way to tackle the ill-posed problem is employing an electrophysiological model incorporating the prior known physiological knowledge in the inverse approach. The heart excitation model with *a priori* electrophysiological knowledge can be deemed as explicit constraints on the inverse procedure so that the non-uniqueness of the solutions and the ill-posed nature of the inverse problem are circumvented. This method was proposed by He and coworkers and tested in a computer simulation study [He et al

2002]. The schematic diagram the heart-model-based inverse approach is shown in Figure 2.1.

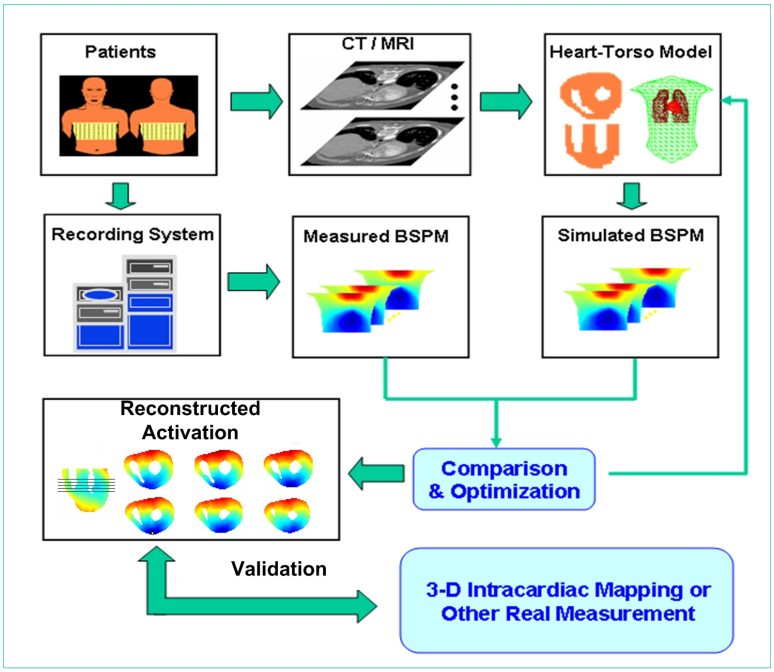

Figure 2.1. Schematic diagram of the heart-model-based 3D inverse approach. (Reproduced, with permission, from He B, Li G, Zhang X. Noninvasive three-dimensional activation time imaging of ventricular excitation by means of a heart-excitation model. Phys Med Bio 47:4063-78, 2002)

The heart-torso geometry of an individual subject is acquired by segmenting CT/MRI slices. Given the obtained heart geometry and the *a priori* physiological knowledge, a 3D heart-excitation model is built. The equivalent current dipoles are calculated during the simulated heart excitation based on the bidomain theory, and then are related to the body surface potentials. The global 3D activation sequence is estimated by the heart model after the parameters of the heart model are optimized by means of nonlinear estimation procedure. In brief, a previously developed preliminary classification system using artificial neural networks (ANN) is applied to initialize the

parameters of the heart-excitation model. The model parameters are iteratively adjusted in an attempt to minimize the dissimilarity between the measured and the heart-model-generated body surface potentials. The 3D activation sequence is produced by utilizing the adjusted heart model parameters when the simulated body surface potentials and the measured body surface potentials match well.

The heart-model-based 3D activation imaging approach has been rigorously validated in a closed-chest in vivo rabbit model using intra-operative needle electrodes, and promising results were reported [Zhang et al 2005; Liu et al 2006a].

2.4.3. Physical-model-based 3D activation sequence imaging

The above 3D activation sequence imaging method explicitly utilizes prior electrophysiological assumptions. Most recently, a novel approach which images the 3D ventricular activation sequence without an explicit physiological heart model has been proposed [Liu et al 2006b]. The proposed method is based on the physical modeling of the heart-torso volume conductor and the distributed equivalent current sources arising from the gradient of transmembrane potential throughout the ventricular myocardium. The equivalent current source distribution is firstly reconstructed from the body surface potentials at every time instant during the period of ventricular activation. The activation time at any given location within the 3D myocardium can be estimated as the time instant corresponding to the occurrence of the maximum value of the estimated current density at this location.

As mentioned in 2.4.1, a linear relationship exists between the distributed equivalent current dipoles and the body surface potentials at each time instant. Owing to the steepness of depolarization, these myocardial cells can only stay in the depolarization phase shortly (or virtually instantaneously); therefore, the excitation wavefront is expected to propagate by a given myocardial site only at its activation time. As a result, when one looks at the time-varying equivalent current dipole $j(r,t)$ at a fixed location r, its amplitude $|j(r,t)|$ reaches the maximum value exactly at its activation time $\tau(r)$ for the entire duration T of the ventricular depolarization. Thus the activation sequence throughout the 3D ventricular volume can be determined by evaluating the time course of local equivalent current dipole at every myocardial site. Therefore, the noninvasive estimation of the activation sequence from the body surface potential measurements consists of two steps: 1) imaging the 3D equivalent current sources; 2) detecting the temporal "marker" at which the inversely calculated source magnitude arrives at its maximum. The principle of this physical-model-based 3D inverse approach is illustrated in Figure 2.2. This novel algorithm has also been validated in a rabbit model with good performance [Han et al 2008].

2.5. Summary

The cardiac inverse problem have been investigated for decades, from focal sources to distributed sources, from heart surface imaging to three-dimensional imaging. To date, the heart surface distributed source imaging techniques have gained much attention and successfully proved the value in clinical application (the Ensite systemfor management of arrhythmias). On the other hand, the three-dimensional inverse imaging techniques can

overcome the limitation of the heart surface techniques and provide more comprehensive and insightful electrophysiological information, and will have great potential on not only clinical applications but also cardiac electrophysiological research.

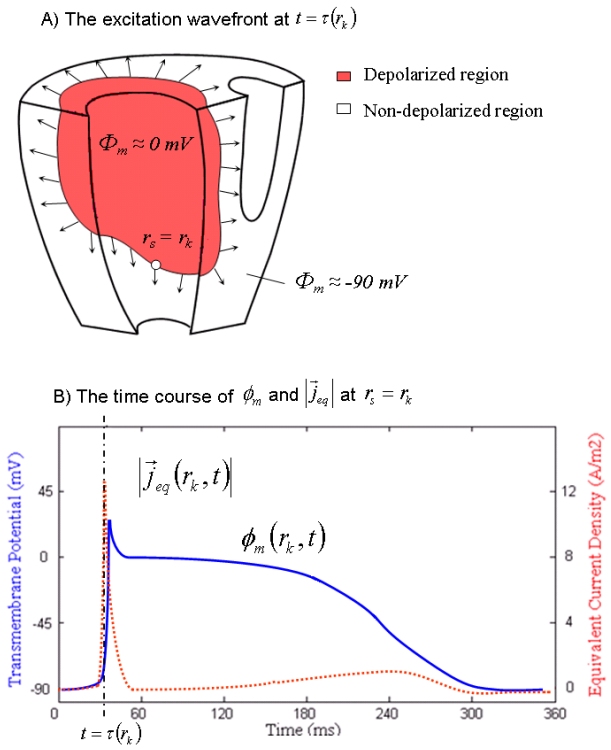

Figure 2.2. Principle of the physical-model-based 3D inverse approach. (A) Ventricles are shown at the instant $t = \tau(r_k)$ ($\tau(r_k)$ is the activation time at r_k) when the excitation wavefront is propagating by a given location r_k (marked by a circle). Over each point along this wavefront, the local equivalent current density field (appearing as a current dipole) arises from the sharp spatial variation of the transmembrane potential across the wavefront, which is much larger than any other non-wavefront location. Therefore, these dipoles dominate the instantaneous cardiac electrical activity that accounts for the measurable torso electrical potentials. (B) It shows the time courses of the transmembrane potential $\Phi(r_k)$ and the amplitude of the associated equivalent current density $|j_{eq}(r_k)|$. "Spike" of $|j_{eq}(r_k)|$ occurs exactly at $t = \tau(r_k)$, coinciding with the instant when the myocardial cells at r_k are undergoing steep depolarization. This relationship suggests that the activation time at a given myocardial site can be estimated by detecting the temporal peak of the magnitude of its local equivalent current density. (Reproduced, with permission, from Liu Z, Liu C, He B. Noninvasive reconstruction of three-dimensional ventricular activation sequence from the inverse solution of distributed equivalent current density. IEEE Trans Med Imaging 2006;25:1307-18.)

3. Estimation of global ventricular activation sequences by noninvasive 3-dimensional electrical imaging: validation studies in a swine model during pacing

3.1. Objective

The heart-model-based three-dimensional cardiac electrical imaging (3DCEI) approach was proposed by He and coworkers [He et al 2002], which can image the global activation sequence from noninvasive body surface potential maps (BSPMs). This technique has been validated in a rabbit model with the aid of intra-operative needle electrodes [Zhang et al 2005]. In order to evaluate the 3DCEI approach in a more rigorous environment, we aimed to further validate the 3DCEI approach by using a swine model, whose cardiac size, heart-torso geometry and electrophysiological characteristics were chosen to best approximate those of an adult human. In addition to the control animal investigations, a chronically induced heart failure (HF) model was also used to test the performance of 3DCEI under diseased conditions. The chest of the animal is intact to mimic the treatment on real patients. The contents in this chapter, including text, figures and tables were published in [Liu et al 2008], and reprinted here with permission.

3.2. Methods

3.2.1. Control and Chronic Heart Failure Swine Models

Control swine (n=2) and a single swine with chronically induced heart failure (HF) were employed in these investigations. The induced HF was achieved by high-rate pacing (VVI mode, 200 beats/min) for four week period. The surgical preparation of these animals for hemodynamic and electrical monitoring has been previously reported [Laske et al 2006]. During the comparative mapping studies, each animal was anesthetized with

a fentanyl infused at 0.75 mcg/kg/min; all were intubated and mechanically ventilated with 65% air and 35% O_2 to maintain a $PaCO_2$ of 40 ± 2 mmHg.

Active-fixation pacing leads were implanted in both the right ventricular apex (RVA) and the RV septum (RVS) (Model 3830, Medtronic, Inc., USA); intramural pacing. Endocardial surface pacing from either the left ventricular (LV) apex (LVA), LV lateral wall (LVL), or LV anterior (LVAn) sites was accomplished by a quadripolar EP catheter (MarinR, Medtronic, Inc.). The 3D locations of the endocardial pacing sites were recorded on the reconstructed LV geometry acquired with the NCM system.

For each animal, the pre-operative magnetic resonance imaging (MRI; ECG gated to end diastole) was acquired approximately 5-7 days before the *in vivo* mapping experiment so to obtain the needed anatomical geometry information. On the mapping study day, body surface potential mapping and intracavitary mapping (by the EnSite® NCM system) were simultaneously performed during the various pacing protocols. For the body surface potential mapping, up to 100 disposable electrodes were placed on the anterolateral chest (see Figure 3.1). The body surface electrodes were referenced to the Wilson central terminal. The 3D locations of the body surface electrodes and the fiducial points were digitized using a radio frequency localizer (Fastrak, Polhemus Inc.). After the completion of the data collection protocol, each heart was removed and fixed in formalin with the intramural pacing leads remaining in place. These isolated hearts were again MRI scanned to record the precise locations of the RV pacing sites.

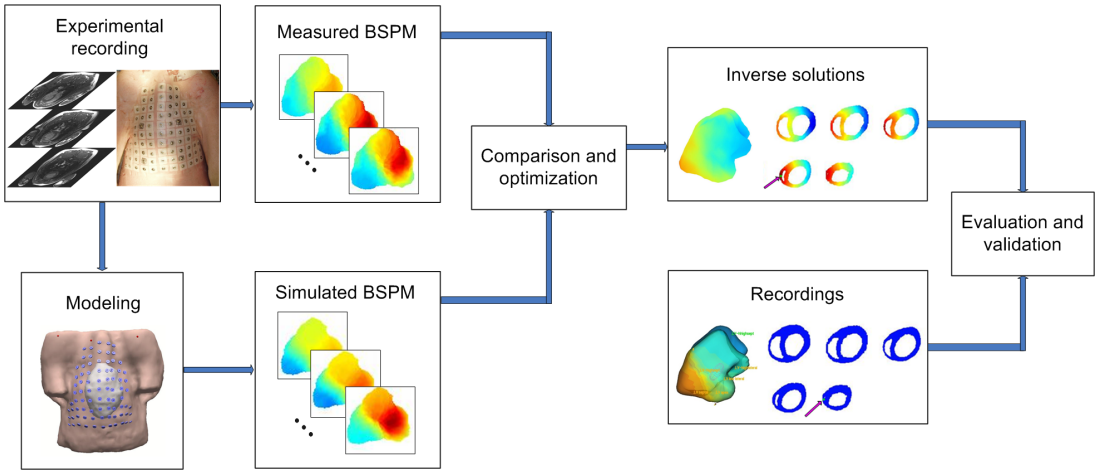

Figure 3.1. The schematic diagram of the noninvasive three-dimensional electrical imaging approach.

3.2.2. Principles of the 3D cardiac electrical imaging

The heart-model-based 3DCEI methodology was previously described in detail [Li et al 2001; He et al 2002; Zhang et al 2005]. A schematic diagram of 3DCEI is shown in Figure 3.1. In brief, for each animal, a heart-excitation model and the heart-torso volume conductor model were constructed based on the pre-operative MRI scans and the prior known physiological knowledge, specifically, of the swine heart. The MR images were segmented to obtain the detailed cardiac geometry and the cellular-automaton heart model. The entire heart excitation process could be simulated and the corresponding BSPMs were calculated by using the boundary element method. A preliminary classification system was employed to initialize the parameters of the heart-excitation model, and then the model parameters were iteratively adjusted in an attempt to minimize the dissimilarity between the measured and the heart-model-generated BSPMs until the convergent criteria were satisfied. In this study, for each pacing site, both the 3D location

of the initiation site for electrical activation and the corresponding activation sequence throughout the ventricles were noninvasively estimated by the above procedure.

3.2.3 Evaluation of the 3DCEI solutions

The relative performance of this 3DCEI approach was further validated by evaluating the localization errors of the initiation sites of activation and comparing the estimated activation sequences with that reconstructed by the endocardial NCM system.

The locations of the initiation sites of activation were inversely estimated in the heart-excitation models, which were obtained from the pre-operative MR images. The precise locations of the pacing sites in RV were obtained by locating the distal end of the pacing leads in the post-operative MR images of the isolated hearts; note that each heart was fixed in an end diastolic state. For the purposes of determining the precise 3D locations of the initiation sites in the resultant heart-excitation models, an image registration procedure between the isolated, fixed hearts and the beating hearts were performed. The epicardial surfaces of the fixed heart and the beating heart were extracted from the post-operative MR images and the pre-operative MR images, respectively, and then were registered by applying a multidimensional registration approach based on the Euclidean distance transform and the Marquardt-Levenberg optimization algorithm [Kozinska et al 1997]. The primary principle of this approach was to minimize the averaged distance between the two sets of special points. After the registration, the precise locations of the initial activation sites in RV were determined in the heart-excitation model and could be directly compared with the estimated locations.

Each heart was also paced at endocardial locations within the LV with an EP catheter. The endocardial geometries of the LV and the precise locations of the endocardial pacing sites were recorded by the NCM system. In order to determine the precise locations of the pacing sites reflected in the resultant heart-excitation models, the endocardial surface maps were extracted from the NCM recordings and then registered with the corresponding surface of the beating heart segmented from the pre-operative MR images. The registration approach used here was identical to that used on the epicardial surface registration described above. We defined the precise locations of the endocardial pacing sites within each heart-excitation model as the closest point on the endocardial surface of the beating heart to the corresponding pacing sites on the endocardial surface recorded by the NCM system.

In addition to the localization of the initiation sites of activation, the ability of the 3DCEI approach to estimate global, 3D activation sequences was also evaluated. The NCM system recorded the endocardial activation sequences of the LV, while the 3D activation sequences throughout the myocardium were noninvasively estimated by the 3DCEI approach. The endocardial activation sequences were extracted from the 3D solutions, and then projected from the endocardial surfaces of the heart models to the endocardial surface maps recorded by the NCM system; so that we could compare our results with the output of the NCM system based on the same geometrical surfaces.

3.3. Results

3.3.1. Experimentation and modeling

In these in vivo studies, the heart-model-based 3DCEI analyses were conducted on sets of data obtained from three swine (healthy controls, n=2, and another with chronically induced HF). The computational heart-torso geometries were constructed for each animal basis of their prior obtained individual MR images. Each model contained over 100,000 cellular units with the spatial resolution of 1.5 mm. Due to the large number of cellular units of these heart models, each heart was further sub-divided into 500-650 myocardial segments. Cardiac electrical activity at each myocardial segment was represented by a regional current dipole for evaluating the BSPM during ventricular activations. Pacing was conducted in each animal's heart from a number of intramural (RVA and RVS) and endocardial ventricular sites (LVA, LVL, LVAn). Although the HF animal was paced from the RVS, because the pacing lead shifted before the post-operative MR scan was performed, this pacing site was not included in the subsequent validation analyses. A summary of the modeling and experimental parameters can be found in Table 3.1.

Table 3.1 Experimental parameters

Pig No.	*Condition*	*Cellular units*	*Segments*	*Surface electrodes*	*Pacing sites*
1	control	110,294	536	84	RVA, RVS
2	control	120,439	586	81	RVA, RVS, LVA, LVL, LVAn
3	heart failure	130,679	645	100	RVA, LVA, LVL

3.3.2. Intramural RV Pacing

Intramural pacing was successfully completed in the RV in all three animals. Figure 3.2 demonstrates an example of the BSPM results during RVS pacing in a control animal. In panel (a), six beats are displayed, including two beats under sinus rhythm (the first two) and three beats when the heart is captured by pacing (the last three). In panel (b), the BSPMs are shown from the onset of pacing to the end of activation. The 3DCEI analysis was applied on the BSPMs collected (corresponding to the fifth beat in panel (a)) and the estimated location of the initiation site and the detailed 3D activation sequence are shown in panel (c). Figure 3.3(a) depicts an example of the imaging results when the HF swine was paced from RVA.

In total, 5 intramural sites in RV were paced, and 50 paced beats were analyzed (10 for each site). The evaluation of the estimation results are summarized in Table 3.2. Over the 50 beats analyzed, the averaged localization error (LE) of the initiation site of activation was 7.3±1.8 mm. It was observed that the depolarization propagation was similar between the estimated activation sequence by 3DCEI and those recorded on the NCM system for all pacing sites.

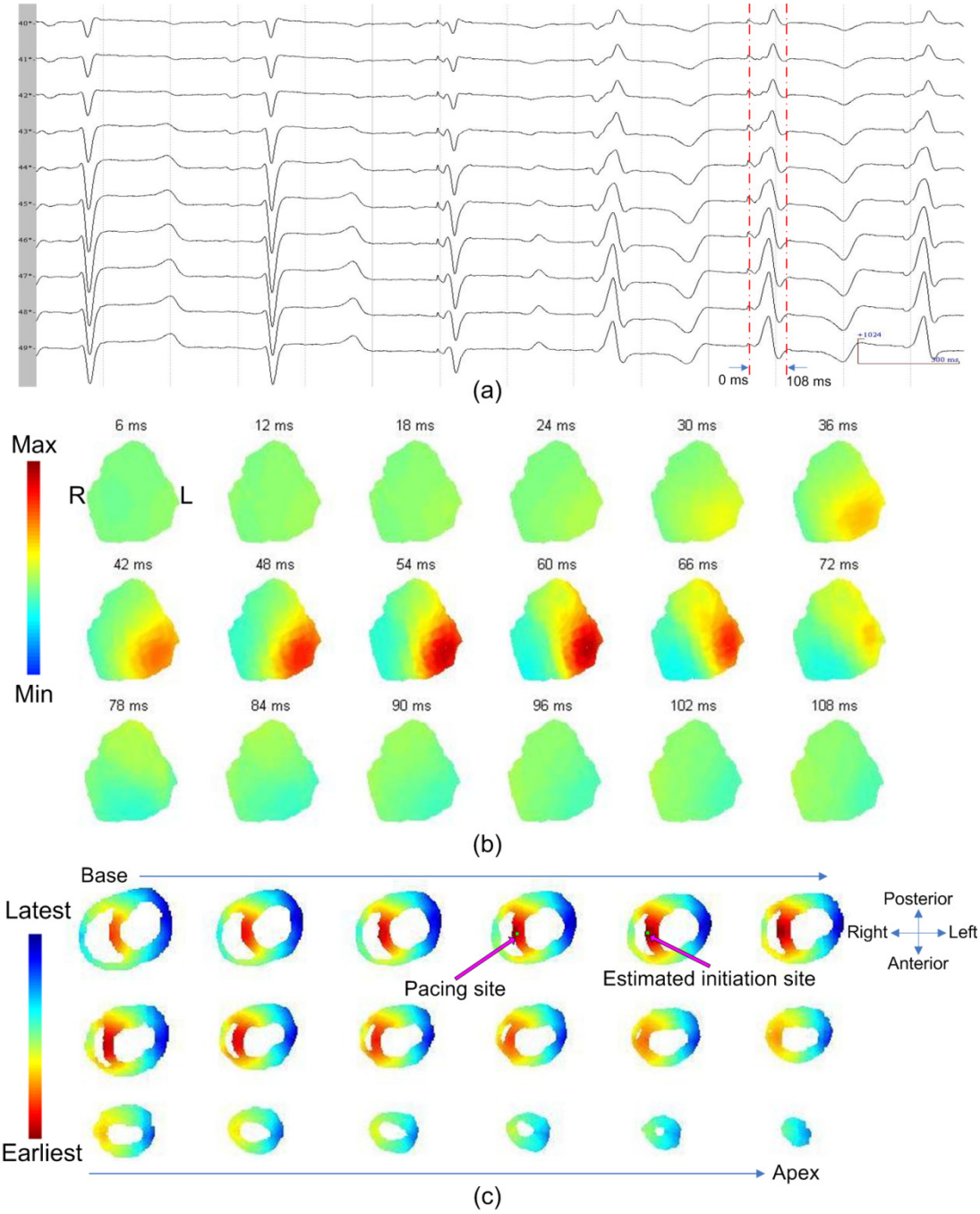

Figure 3.2. (a): The ECG waveforms recorded from the body surface electrodes with corresponding time intervals. (b): The body surface potential maps. (c): The location of the initiation site and the 3D activation sequence (AS). The relative geometry of the heart is shown by horizontal sections, arranged from base to apex. The precise location of the initiation site and the estimated location of the initiation site are indicated. The 3D AS is shown on the horizontal sections.

Table 3.2 Evaluation of the RV pacing results

Pig # and condition	*Pacing site*	*Localization error (mm)*										*Mean (mm)*
		1	2	3	4	5	6	7	8	9	10	
1, control	RVA	8.2	9.5	8.2	6.9	6.0	7.5	9.0	6.7	6.0	8.7	7.7±1.2
1, control	RVS	6.4	7.3	6.2	5.0	6.5	3.7	7.8	3.7	3.7	6.2	5.6±1.5
2, control	RVA	7.6	8.1	8.1	8.1	7.6	6.4	7.8	8.1	9.2	8.1	7.9±0.7
2, control	RVS	4.7	9.1	9.1	10.6	9.1	7.6	9.1	7.6	9.1	9.1	8.5±1.6
3, heart failure	RVA	3.7	4.2	5.4	5.6	10.2	7.3	7.3	5.6	6.7	8.7	6.5±2.0

3.3.3. Endocardial LV Pacing

Stable endocardial pacing within LV was successfully obtained in one control animal and in the HF animal (Table 3.1). Figure 3.3(b) represents an example of the imaging results that was observed when pacing a control animal from the LV anterior endocardial site, and Figure 3(c) represents another example when pacing the same animal from the LV apical endocardial site. In total, 5 endocardial sites in LV were paced, and 50 paced beats were analyzed (10 for each site). The evaluation of the estimation results are summarized in Table 3.3. Over the 50 beats analyzed, the averaged LE of the initiation site of activation was 7.0 ± 2.2 mm. Similar to the results when intramural pacing was conducted, the estimated endocardial activation sequence by 3DCEI demonstrated a similar depolarization wavefront to the recorded endocardial activation sequence generated by the NCM system.

Table 3.3 Evaluation of the LV pacing results

Pig # and condition	*Pacing site*	*Localization error (mm)*										*Mean (mm)*
		1	2	3	4	5	6	7	8	9	10	
2, control	LVA	9.7	11.7	11.0	11.7	9.7	7.5	9.7	11.2	8.6	9.7	10.1±1.4
2, control	LVL	3.4	5.4	6.4	5.4	4.7	4.5	3.4	4.7	4.5	4.7	4.7±0.9
2, control	LVAn	4.5	9.1	8.9	6.9	5.4	8.1	9.6	6.9	5.0	5.0	6.9±1.9
3, heart failure	LVA	7.6	4.7	6.2	7.6	9.1	7.6	4.7	4.7	6.2	7.6	6.7±1.5
3, heart failure	LVL	5.6	6.9	5.6	8.6	7.8	7.0	5.0	5.6	5.6	9.2	6.6±1.5

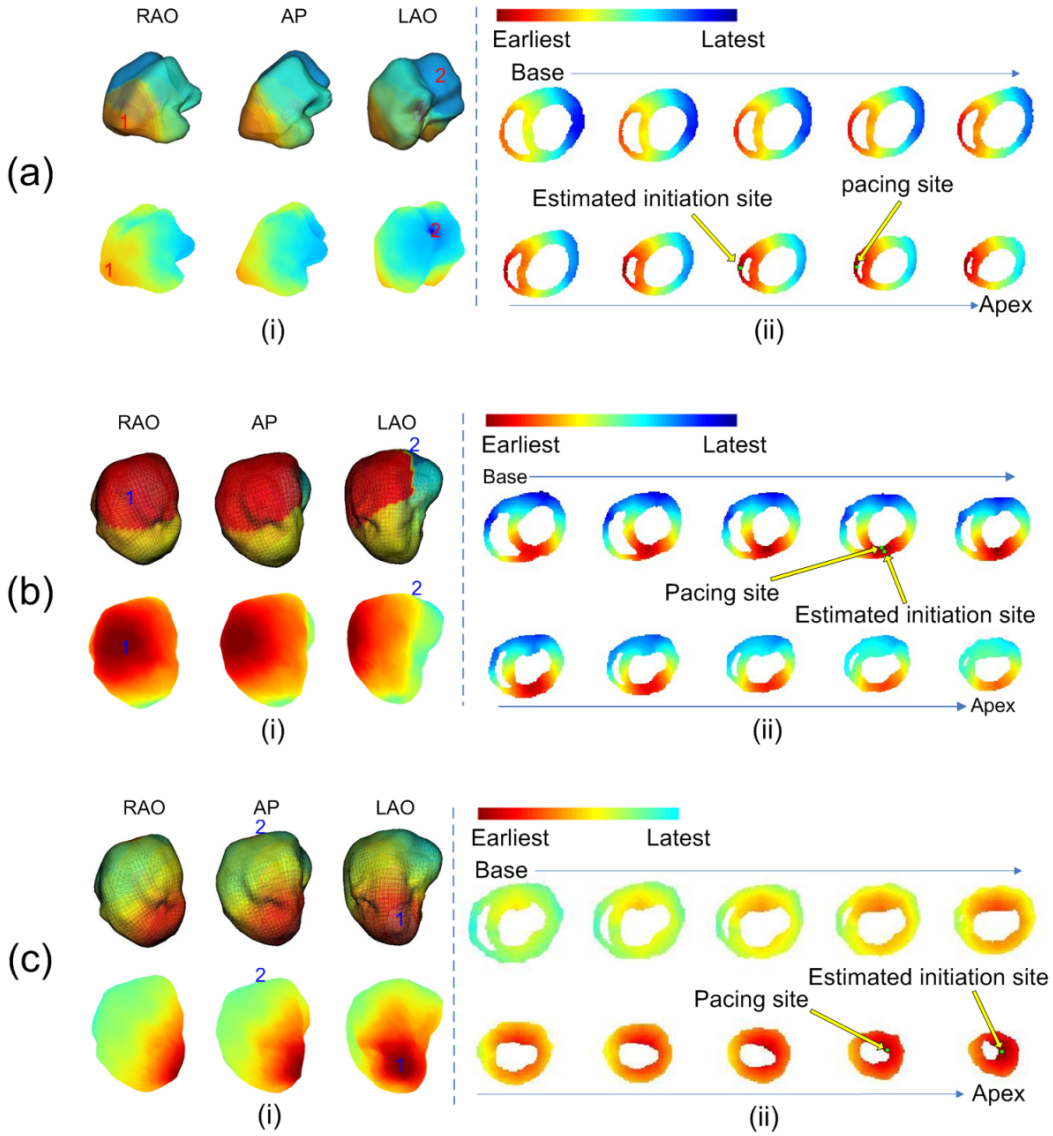

Figure 3.3. The evaluation of the inverse results when: (a) the HF animal was paced from the RV apex; (b) a control animal was paced from the endocardial LV anterior; (c) a control animal was paced from the endocardial LV apex. In each panel, (i): the activation sequence (AS) on the LV endocardial surface. The AS reconstructed by the NCM system is shown in the upper row in 3 views: RAO, AP and LAO. RED represents the earliest activated area and BLUE represents the latest activated area. The earliest activated site is indicated by the number "1" and the latest activated site is indicated by "2" on the figure. The corresponding AS estimated by 3DCEI is shown in the lower row. The earliest activated site and the latest activated site are also indicated by "1" and "2", respectively. (ii): the location of the initiation site and the 3D AS. The geometry of the heart is shown by 10 horizontal sections, arranged from base to apex. The precise location of the initiation site and the estimated location of the initiation site are indicated. The 3D AS is shown on the 10 sections.

3.4. Discussion

The present study has experimentally demonstrated the capability of our noninvasive 3D electrical imaging approach to localize the electrical initiation sites and estimate the resultant activation sequences. To our knowledge, the present study represents the first reported effort in literature to validate electrocardiographic inverse solutions using simultaneous body surface and intracavitary recordings in an *in vivo* animal, under both control and diseased conditions. The animal model chosen for these studies was the swine due to their close approximation to humans in their cardiac sizes, heart-torso geometries and electrophysiological characteristics. Swine have a non-compliant thorax which is more similar to the human (versus canine) condition and further has a relative thoracic surface mimicking an average adult. Therefore, we believe the validation employing a swine model provides stronger clinical significance than the previous validation in a rabbit model where an open-chest procedure was used [Zhang et al 2005]. Importantly, promising results were also demonstrated when investigating a disease heart model, which suggests the 3DCEI approach may be robust enough to account for complex, clinical conditions that may be found in a clinical setting.

The localization of the initiation site and/or arrhythmogenic substrate of various cardiac arrhythmias has direct clinical benefit for the guidance of catheter ablation procedures. Efforts have been made to find the earliest activated site(s) of cardiac events on the epicardium [Oster et al 1997], endocardium [Gornick et al 1999] or the entire heart surface (endocardium and epicardium) [Huiskamp et al 1997; Tilg et al 2002]. These methods define their solutions on the heart surface and beneficial results have been

reported. However, often times, the cardiac event occurs within the myocardial wall, thereby increasing the difficulty in locating the accurate location and depth for targeting the ablative therapy. The noninvasive 3D imaging methods provides for greater anatomical resolution and thus may provide a greater clinical benefit and efficacious therapy. In the present study, we consider that the successful localization of the initiation sites induced by pacing suggests the potential feasibility of localizing the initiation sites of focal ventricular tachycardia and/or other cardiac arrhythmias throughout the 3D myocardium. Pacing was performed within both ventricular chambers, from the endocardial surfaces and with implanted electrodes (intramural activation). We obtained minimal to relatively small localization errors for such pacing employing this 3DCEI approach. The averaged localization error of all pacing trials was approximately 7 mm, which suggests the potential of guiding catheter ablation procedures by applying 3DCEI.

In addition to localizing the arrhythmogenic focal trigger and/or substrate, importantly the 3DCEI approach can further estimate the global 3D electrical activation sequence in multiple cardiac chambers simultaneously. In the present study, we evaluated our estimated AS by comparing with the AS reconstructed by the NCM system. It was observed that the endocardial AS estimated by 3DCEI demonstrated a consistent propagation pattern to that reconstructed by the NCM system (examples shown in Figure 3), which is currently routinely used in the clinical setting for the guidance and navigation of atrial ablation procedures. The similarity in activation sequence provides evidence that the estimated endocardial AS extracted from the estimated 3D AS could prove clinically valuable and efficacious.

The present study further investigated an animal with high-rate pacing induced HF. Thereby, the heart was observed to have a larger geometry than the control animal (nearly a doubled diastolic volume), and associated increased durations of the QRS complexes. It should be noted that there were no regional cardiac dysfunctions in this animal (such as that due to an infarction). Yet, the high correlation between the simulated BSPMs and the recorded BSPMs provided further validation of our forward model. Specifically, in this animal, we successfully recorded the simultaneous mapping data when pacing from three different sites. The analyses of the obtained data proved that on this diseased swine model, the 3DCEI approach could generate adequate inverse solutions; as with the controls (shown in Table 2 and Table 3). This robust performance of 3DCEI indicates its ability to afford strong clinical utility in complex procedures.

To date, we have experimentally demonstrated the feasibility of localizing the initiation sites and image maps the global electrical activation sequences using 3DCEI techniques for single-site pacing. Future investigations will need to focus on more complex arrhythmic events, such as reentrant ventricular tachycardias, so to provide further clinical utility of such an approach.

Limitations

Although we have obtained the 3D activation sequence, we can only evaluate its endocardial propagation pattern under the present experimental protocol without using 3D intracardiac mapping procedure. Although employing non-contact mapping within the protocol provides many benefits for the testing of the 3DCEI methodology in a setting

similar to clinical studies in human patients, it also represents a limitation in such that we do not have direct measurements within the 3D ventricular volume. We used non-contact endocardial mapping results, as practiced in clinical cardiology, to validate our 3DCEI results and its ability to display activation sequence propagation. The NCM system does not provide the quantitative output of the activation sequence on the endocardial surface, so the quantitative comparison between our estimated activation sequence and the NCM results was not done in the present study. However, the present comparison study, although qualitative in nature, should still provide important experimental evidence to assess the performance of the 3DCEI, as the present protocol does not need an open-chest procedure.

As described in the Methods session, in order to determine the precise locations of the endocardial pacing sites in the heart-excitation model, the endocardial surface recorded by the NCM system was registered with the corresponding surface of the beating heart segmented from the pre-operative MR images. Although both of the endocardial surfaces correspond to diastole, they can not exactly match due to the complex positional and size changes that may occur during the cardiac and respiratory cycles. Because of this problem, error might be introduced when the registration procedure was applied. Such error is not unique to this Ensite/MRI registration. A similar case was reported to register the surface recorded by CARTO® system with the CT images [Dong et al 2006]. Their results showed that the registration accuracy could be significantly increased when multiple surfaces were involved in the registration

procedure. For instance, we might detect the geometries of both LV and superior vena cava for the purpose of registration in future study.

3.5. Conclusions

We have demonstrated the feasibility of localizing 3D initiation sites of activation and estimating the activation sequences within both healthy and diseased large mammalian models from noninvasive body surface potential measurements by using 3DCEI. These promising results suggest that the 3DCEI approach may provide a useful tool not only for basic cardiovascular research, but may have future utility for the clinical diagnosis and management of arrhythmias.

4. Localization of site of origin of reentrant arrhythmia from BSPMs: a model study

4.1. Objective

Reentry arrhythmias occur when an electrical impulse recurrently travels in a tight circle within the heart, rather than moving from one end of the heart to the other and then stopping [Allessie et al 1976]. Normally, the action potential impulse will spread through the heart quickly enough that each cell will only respond once. However, if conduction is abnormally slow in some areas, part of the impulse will arrive late and potentially be treated as a new impulse. Depending on the timing, this can produce a sustained abnormal circuit rhythm. Reentry circuits are responsible for atrial flutter, most paroxysmal supraventricular tachycardia, and dangerous ventricular tachycardia. Localizing the origin of reentry is of importance for treating the resultant arrhythmias, e.g. guiding catheter ablation to block the pathway of reentry.

The aim of the present study is to apply the principle of the heart-model-based 3DCEI approach to develop a electrocardiographic imaging algorithm for estimating the site of origin of reentrant arrhythmia from body surface potential maps (BSPMs), with the aid of a cardiac arrhythmia model. By using an ion-channel-level cardiac model, with which reentry can be simulated, it is anticipated that more accurate inverse solutions may be obtained in localizing the site of origin of reentrant arrhythmia from BSPMs. Computer simulation studies were conducted to test the feasibility of this approach. The contents in this chapter, including text, figures and tables, were published in [Liu et al 2005] and reprinted here with permission.

4.2. Methods

4.2.1. Cardiac model

The ion-channel-level cardiac simulation model was composed of 32×32×32 cellular units over a cube. The distance between adjacent cellular units is 3 mm. For each cardiac cellular unit, the Beeler-Reuter (BR) model [Beeler and Reuter 1977] was applied to simulate its action potential (AP). A rule-based excitation propagation model [Moe et al 1964] was applied to manage the propagation of cardiac excitation from the excited cell to its adjacent cells. An excited cell could propagate its activation to 6 adjacent cells. If a cell is activated, its adjacent cells will be activated after the time for propagation and start their excited phase if they are not only excitable but also in resting phase. The propagation time delay is controlled by the rule-based excitation propagation model. If a cell is detected eligible for excitation, an initial stimulation will be applied on it to trigger an action potential. If an adjacent cell is not excitable or is in refractory period, the activation will not propagate through it.

4.2.2. Reentry simulation

To simulate reentry, 2 abnormal conduction areas were set in the cardiac model. One is a necrotic myocardial zone (NMZ) in where all the cells were unexcitable, and another is a unidirectional block (UDB) cell wall on which the excited current of each cell could only propagate in one direction. To initialize an excitation process in the cardiac model, one or a group of cells was/were selected to receive the external stimulation current. At the beginning, all excitable cells were at the resting status. The S1 stimulation was applied on the bottom cells with a 20 microampere current of duration of 5 milliseconds.

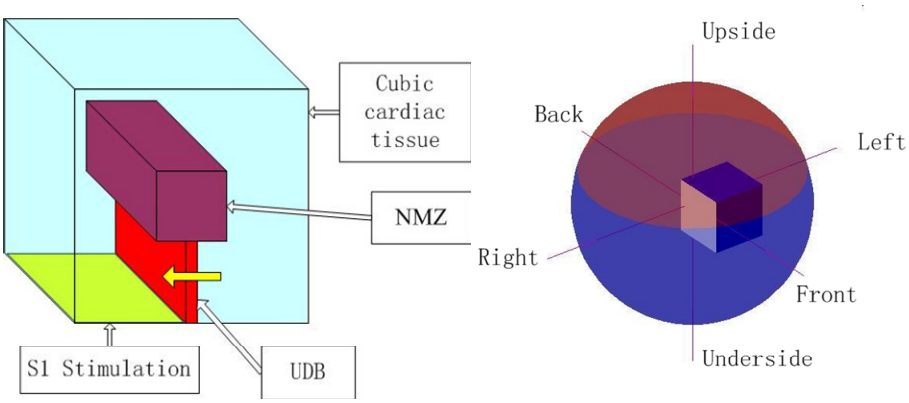

Figure 4.1. (a) Schematic diagram of reentry simulation setting in the cardiac model. (b) The relative heart-torso position. The cubic heart model is located within the spherical torso model with an eccentric distance of 5 cm.

Figure 4.1(a) shows the setting in the cardiac model, where the UDB was set beneath the NMZ. The size of the section of NMZ was 2.1×2.1 cm, and the thickness of UDB wall was 0.3 cm. As can be seen from Figure 4.1(a), the characteristics of the source setting were kept the same in one coordinate, so the source model is essentially a 2D model while occupying a 3D cube, by extending over the 3rd dimension.

4.2.3. BSPM simulation

The cubic heart model was placed within an infinite homogenous volume conductor with body surface electrodes being positioned over a spherical surface, to simulate the heart-torso geometric relationship. The radius of the spherical torso is 15 cm. To simulate the eccentricity of heart, the center of the cardiac model was set 5cm away from the center of the spherical torso (4cm rightward and 3cm ahead). The relative positions between the cardiac model and the spherical torso are showed in Figure 4.1(b). Electrical

potentials were evaluated at 200 or 64 sites uniformly distributed over the spherical surface to simulate the BSPMs.

4.2.4. Inverse estimation

A NMZ area incorporated with a UDB cellular wall was set in the cardiac model to simulate a reentry. BSPMs at different time instants (with 1 ms interval) were calculated at electrodes over the spherical surface, and Gaussian white noise (GWN) was added to the BSPMs to simulate the "measured" BSPMs. The noise level was 5%, corresponding to the ratio of the standard deviation and the maximum value of the calculated body surface potentials. Assuming the maximum potential being at 5 mV, this corresponds to a 250 μV standard deviation of noise. Apparently, the noise level used in the present simulation study is quite high, simulating the clinical setting at an electrophysiology (EP) lab when a patient is receiving EP test.

The central point of NMZ in the cardiac model is defined as the site of origin of a reentry, so the localization of NMZ was optimized by the optimization system. In the inverse approach, the size of NMZ was set as the same with that used in the forward approach. The site of origin of the reentry was estimated by minimizing dissimilarity between the "measured" and the simulated (forward) BSPMs. In the present study, the following two objective functions were used to reflect the similarity and dissimilarity between the "measured" and the simulated BSPMs.

1) E_{CC}, which was constructed with the averaged correlation coefficient (CC) between the "measured" and simulated BSPMs at N time instants, is defined as

$$E_{CC} = \sum_{i=1}^{N} CC(i) / N \qquad (4.1)$$

where $CC(i)$ is the CC between the "measured" and simulated BSPMs at the i^{th} instant. The BSMPs at N instants between 350 ms and 490 ms after initial activation were selected to construct the 1st objective function.

2) E_{RE}, which was constructed with the averaged relative errors (RE), is defined as

$$E_{RE} = \sum_{i=1}^{N} RE(i) / N \qquad (4.2)$$

where $RE(i)$ is the RE between the "measured" and simulated BSPMs at the i^{th} instant. Similarly, the BSMPs at N instants between 350 ms and 490 ms after initial activation were selected to construct the 2nd objective function.

This is a nonlinear optimization problem with 2 objective functions, and the Simplex Method [Kowalik and Osborne 1968] was used. To search for the solution of the optimization problem, the objective function of E_{RE} was considered as a constraint. By setting an initial NMZ area with a corresponding UDB in the cardiac model to induce a reentry, the "measured" BSPMs were simulated and objective functions calculated accordingly. In the cardiac model, four uniformly distributed sites were selected to calculate their corresponding objective functions and the one which had the largest E_{CC} was set as the estimated original site. Eight adjacent sites around the original site were checked to find the one with the largest E_{CC} which would be the next original site to

continue the search. If one site's E_{CC} was larger than the E_{CC} criteria, E_{RE} was calculated to see if it was smaller than the E_{RE} criteria. If yes, this site was chosen as the inverse solution of the site of origin of reentry; if not, the search would continue.

4.3. Results

4.3.1. Cardiac modeling and BSPM simulation

As mentioned above, the source model was actually simplified to 2D. Therefore we will use 2D coordinate to represent the model. Because the number of cellular units is 32×32×32, the range of coordinate was set from 1 to 32. We set the coordinate of the center of NMZ as (16, 16) and got the forward simulation results of cardiac excitation and BSPMs. In Figure 4.2, the propagation of action potential and formation of reentry are displayed. In Figure 4.3, BSPMs, propagation of action potential and ECG wave are displayed simultaneously.

From Figures 4.2-3, it can be seen that the action potential propagated around the NMZ and reentry initiated. The BSPMs reflected both the procedure of propagation of activation and the effect of eccentricity of the heart model. From about 350 ms after S1 stimulation, the ECG waves oscillated and showed characteristics of ventricular tachycardia (VT), which is a possible result of reentry [Josephson et al 1978; Stevenson et al 1993; Malmivuo and Plonsey 1995].

4.3.2. Inverse results for different reentry sites

In the present simulation study, the following parameters were used for the optimization system: 1) The BSPMs at 15 instants were selected to localize the site of

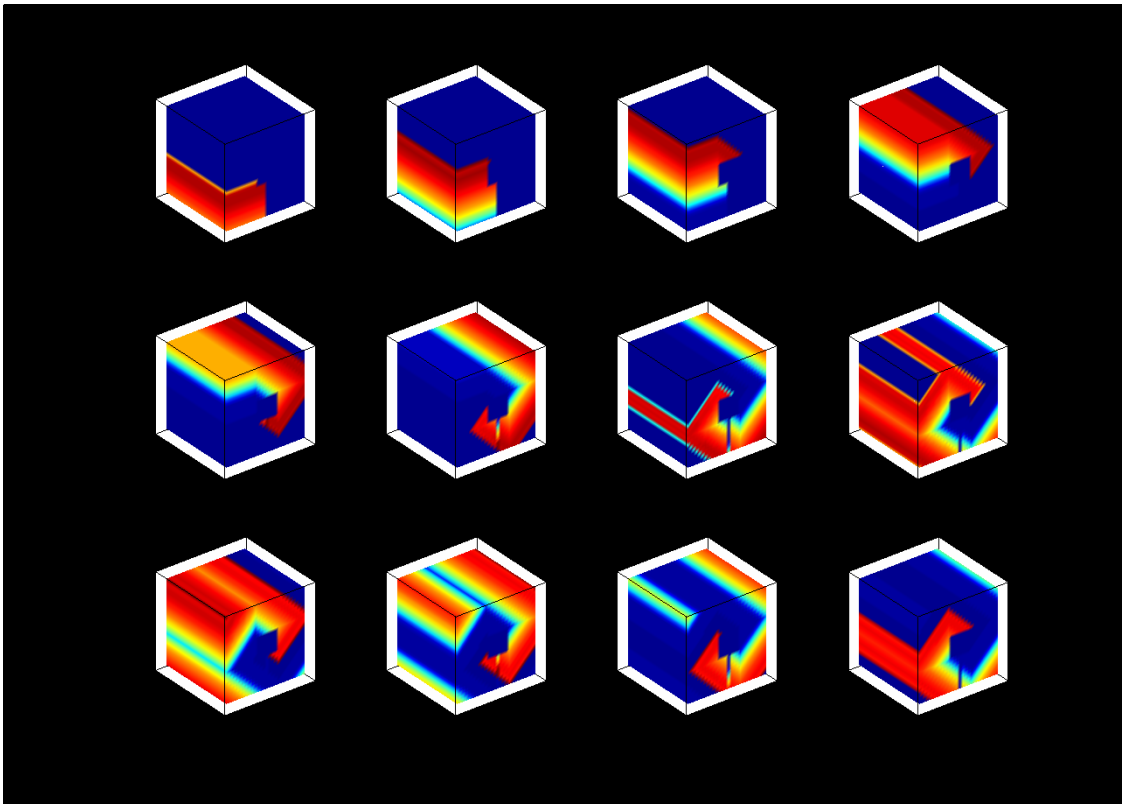

Figure 4.2. The propagation of action potential in the cubic cardiac model. The figures reflect the time instants from 100 ms to 650 ms after the S1 stimulation. The time interval between two adjacent figures is 50 ms.

origin of reentry. Because the ECG waveform became regular at about 350 ms after initial stimulation, 15 instants were selected from 350 ms to 490 ms after initial stimulation, and the time interval between two adjacent instants was 10 ms. 2) The convergence criteria of the optimization system was set as $E_{CC} \geq 0.985$, and $E_{RE} \leq 0.2$. 3) GWN with standard deviation of 5% of the maximum voltage of the BSPMs was added to the calculated BSPMs to simulate "measured" BSPMs.

We selected 11 different sites in the cardiac model as the true sites of origin of reentry. The results are shown in Table 4.1. The mean and standard deviation of E_{CC} is 0.9851 ± 0.0039 and the mean and standard deviation of E_{RE} is 0.170 ± 0.023. The mean

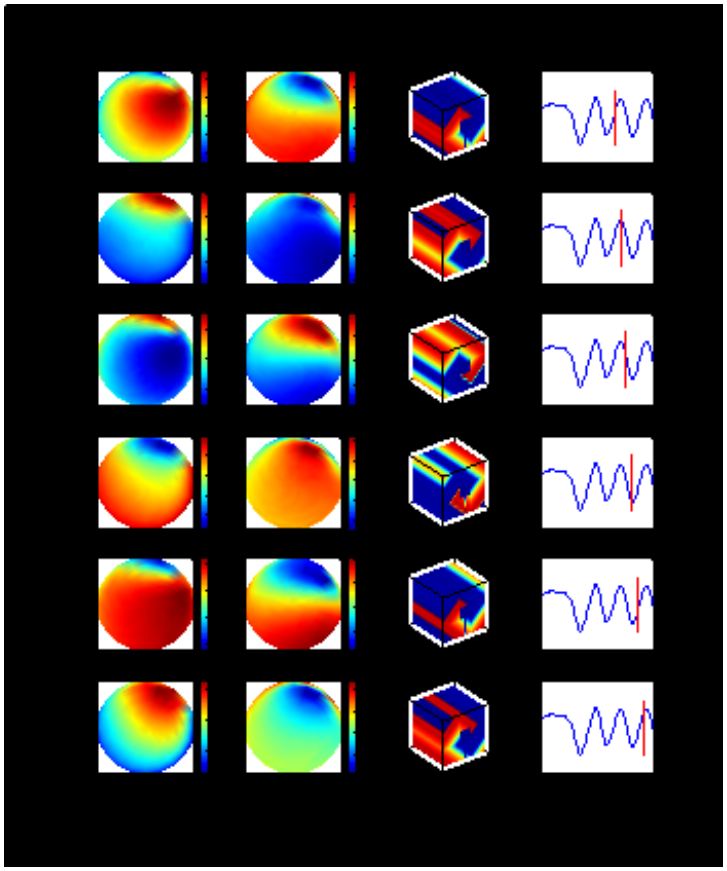

Figure 4.3. Activation maps of a simulated reentry and the corresponding simulated ECG waveforms and BSPMs. From left to right, the first 2 columns are the BSPMs at 6 instants over the superior and inferior hemispherical surfaces, respectively, the third column shows the activation maps in the cardiac model at 6 instants, and the right column shows the 1 sec ECG waveforms at a precordial electrode. The 6 instants are indicated by the red vertical lines shown in the ECG waveform of the right column.

of spatial difference between true sites and inverse solutions is 1.48 mm. The maximum value of spatial distance is 6 mm, and the minimum value is 0, which suggests the present inverse approach localized well the site of origin of reentry. These inverse results indicate the feasibility of localizing the site of origin of reentrant arrhythmia by means of the present model-based imaging approach with the aid of the ion-channel-model-based cardiac model.

Table 4.1. Localization errors when 200 body surface electrodes were used. 5% GWN was added to BSPMs but no geometry uncertainties were considered. The spatial distance between the true site and the inverse solution is shown. The iteration number is the times of search.

True site	Estimated site	Inverse solution	Spatial Distance(mm)	Iteration number
(16,16)	(21,21)	(17,16)	3	6
(16,24)	(11,21)	(15,24)	3	5
(16,9)	(21,11)	(16,9)	0	4
(9,16)	(11,21)	(9,16)	0	5
(24,16)	(21,21)	(24,16)	0	5
(8,8)	(11,11)	(8,8)	0	4
(8,24)	(11,21)	(8,24)	0	4
(24,24)	(21,21)	(22,24)	6	3
(24,8)	(21,11)	(24,8)	0	4
(16,26)	(11,21)	(15,25)	4.24	5
(16,7)	(21,11)	(16,7)	0	6

4.3.3. Effects of heart-torso geometry uncertainties

The effects of inter-subject torso-geometry variation on the performance of the present approach were initially evaluated by using modified torso models: 10% enlargement and 10% reduction of the spherical torso in the heart-torso model. The heart position uncertainty was simulated by moving the heart along the x-direction (from the left to the right), the y-direction (from the front to the back) and the z-direction (from the upside to the underside) of the torso. Six new heart positions (left, right, front, back, upside and underside) were considered by shifting a distance of 10 mm for each one.

Five sites of origin of reentry were selected from the 11 typical sites to test the effects of heart-torso geometry uncertainties on the performance of the present approach. After being modified to simulate geometry uncertainty, the heart-torso models were used in the forward BSPM simulation and the same GWN with standard deviation of 5% of the maximum voltage of the body surface potentials was added to simulate “measured”

BSPMs. Then the standard heart-torso model was used in the inverse procedure. By using the modified heart-torso models in the forward simulations and the standard model in the inverse calculation, the effect of heart-torso geometry variation on the present approach was initially evaluated.

Table 4.2 shows the inverse results of heart-torso uncertainties. It's clear that little effect of the heart-torso geometry uncertainty was observed on the localization of site of origin of reentry in the present simulation. Note that in case of torso enlargement or reduction, the value of E_{CC} was similar with that of standard model's inverse solution while the value of E_{RE} remarkably increased. The means of E_{RE} of the enlarged, reduced, and standard torso models were 0.376, 0.352 and 0.178, respectively. This is reasonable

Table 4.2. Effects of heart-torso uncertainties when 200 body surface electrodes were used. The site of inverse solution is shown in the first row, and the distance between the inverse solution and the true site is shown in the second row.

True sites	(16,16)	(9,16)	(8,8)	(8,24)	(16,26)
Standard model	(17,16) 3 mm	(9,16) 0 mm	(8,8) 0 mm	(8,24) 0 mm	(15,25) 4.24 mm
Torso+10%	(17,16) 3 mm	(9,16) 0 mm	(8,8) 0 mm	(8,24) 0 mm	(15,25) 4.24 mm
Torso-10%	(16,16) 0 mm	(9,16) 0 mm	(8,8) 0 mm	(8,24) 0 mm	(15,25) 4.24 mm
Left shift	(17,16) 3 mm	(9,16) 0 mm	(8,8) 0 mm	(8,24) 0 mm	(15,25) 4.24 mm
Right shift	(17,16) 3 mm	(9,16) 0 mm	(8,8) 0 mm	(8,24) 0 mm	(14,25) 6.71 mm
Front shift	(17,16) 3 mm	(9,16) 0 mm	(8,8) 0 mm	(8,24) 0 mm	(15,25) 4.24 mm
Back shift	(17,16) 3 mm	(9,16) 0 mm	(8,8) 0 mm	(8,24) 0 mm	(15,25) 4.24 mm
Up shift	(16,16) 0 mm	(9,16) 0 mm	(8,8) 0 mm	(8,24) 0 mm	(14,26) 6 mm
Down shift	(17,16) 3 mm	(9,16) 0 mm	(8,8) 0 mm	(8,24) 0 mm	(15,25) 4.24 mm

Table 4.3. Localization error when 64 body surface electrodes were used. 5% GWN was added to BSPMs but no geometry uncertainties were considered. The spatial distance between the true site and the inverse solution is shown. The iteration number is the times of search.

True site	Estimated site	Inverse solution	Spatial Distance(mm)	Iteration number
(16,16)	(21,21)	(17,16)	3	6
(16,24)	(11,21)	(15,24)	3	4
(16,9)	(21,11)	(16,9)	0	4
(9,16)	(11,21)	(9,16)	0	5
(24,16)	(21,11)	(24,16)	0	5
(8,8)	(11,11)	(8,8)	0	4
(8,24)	(11,21)	(9,24)	3	3
(24,24)	(21,21)	(22,24)	6	3
(24,8)	(21,11)	(24,8)	0	4
(16,26)	(11,21)	(15,25)	4.24	5
(16,7)	(21,11)	(16,7)	0	5

because with torso's enlargement or reduction, the patterns of BSPMs changed little while the amplitudes of BSPMs became smaller or larger, respectively. E_{CC} is not sensitive to the amplitude of BSPMs while E_{RE} is. E_{RE} was considered as a constraint in the non-linear optimization problem and contained supplementary information for E_{CC}.

4.3.4. Effects of number of recording electrodes

In the first stage of study, we used 200 uniformly distributed electrodes to compute BSPMs. The number of electrodes was reduced to 64 to test the feasibility of the present approach with a more realistic number of body surface electrodes. The same 11 sites were selected to verify the inverse approach for the standard heart-torso model, and then the effect of torso-geometry variation was also tested. The results are shown in Table 4.3 and Table 4.4.

Table 4.4. Effects of heart-torso uncertainties when 64 body surface electrodes were used. The site of inverse solution is shown in the first row, and the distance between the inverse solution and the true site is shown in the second row.

True sites	(16,16)	(9,16)	(8,8)	(8,24)	(16,26)
Standard model	(17,16) 3 mm	(9,16) 0 mm	(8,8) 0 mm	(9,24) 3 mm	(15,25) 4.24 mm
Torso+10%	(17,16) 3 mm	(9,16) 0 mm	(8,8) 0 mm	(9,24) 3 mm	(15,25) 4.24 mm
Torso-10%	(17,16) 3 mm	(9,16) 0 mm	(8,8) 0 mm	(9,24) 3 mm	(15,25) 4.24 mm
Left shift	(17,16) 3 mm	(9,16) 0 mm	(8,8) 0 mm	(9,24) 3 mm	(15,25) 4.24 mm
Right shift	(17,16) 3 mm	(9,16) 0 mm	(8,8) 0 mm	(9,24) 3 mm	(15,25) 4.24 mm
Front shift	(17,16) 3 mm	(9,16) 0 mm	(8,8) 0 mm	(9,24) 3 mm	(15,25) 4.24 mm
Back shift	(17,16) 3 mm	(9,16) 0 mm	(8,8) 0 mm	(9,24) 3 mm	(15,25) 4.24 mm
Up shift	(17,16) 3 mm	(9,16) 0 mm	(8,8) 0 mm	(9,24) 3 mm	(14,26) 6 mm
Down shift	(18,16) 6 mm	(9,16) 0 mm	(8,8) 0 mm	(9,24) 3 mm	(15,25) 4.24 mm

For the standard heart-torso model, the mean and standard deviation of E_{CC} is 0.9862 ± 0.0039 and the mean and standard deviation of E_{RE} is 0.161 ± 0.026 .The averaged distance between "true" sites and the estimated sites of origin of reentry is 1.75 mm. From Table 4.3 and Table 4.4, we can see that all the selected sites of origin of reentry were successfully localized using 64 electrodes and the precision was similar with that using 200 electrodes. Tables 4.3 and 4.4 suggest that using 64 electrodes we can achieve the similar results in localizing the site of origin of reentry as compared with that using 200 electrodes.

4.3.5. Effects of the location of UDB wall

UDB area is indispensable for inducing reentry in the present model. By setting the UDB beneath the NMZ as shown in Figure 4.1(a), reentry was successfully induced. In the inverse estimation, the location of UDB was kept the same with the forward approach as a priori knowledge. Since the location of UDB may not be known a priori, simulations were conducted to assess the effects of uncertainty in location of UDB. The location and direction of UDB was still set beneath the NMZ in the forward approach to simulate the "measured" BSPM, and then in the inverse procedure the location of UDB was changed to the right hand side of NMZ as an initial guess. In this case, the action potential can only propagate from underside to upside through UDB. The simulation was repeated five times at five sites of origin of reentry. The averaged localization error was 3.50 mm, which suggests that the present approach can tolerate uncertainty in the location of UDB.

4.4. Discussion

In the present simulation study, we have proposed a new approach of localizing site of origin of cardiac arrhythmia from BSPM, and tested the feasibility of localizing the site of origin of reentrant VT from noninvasive BSPMs with the aid of a computer heart model. The present study can be deemed as an extension of the heart-model-based 3DCEI approach. The new contents presented include 1) use of ion-channel-level cellular model; 2) simulation of reentrant arrhythmia and resultant BSPMs; 3) modified objective functions employed in the inverse approach. We have used a simple cardiac model consisting of 32 x 32 x 32 cardiac cellular units embedded in an infinite homogeneous medium of spherical shape. By incorporating the a priori information on

electrophysiological processes within the heart model, the site of origin of reentry has been successfully localized for various different initial sites within the simple ventricle model and with altered geometrical details with regard to the size of torso and position of the heart. The averaged localization error is 1.5mm for 11 testing sites of origin of the reentrant VT. The proposed use of a cardiac arrhythmia model plays an important role in achieving the present promising results by means of the model-based imaging approach.

The Beeler-Reuter (BR) model [Beeler and Reuter 1977] was applied to simulate the cardiac cells' action potential (AP). BR model is flexible to change the waveform of action potential easily by adjusting parameters in the ion-channel-level cellular model to simulate cardiac cells in different status. While one may simulate reentry without using an ion-channel-based cellular model, the ion-channel-based cellular model offers flexibility for developing more complex model in the future when we need to set various parameters for different cells in a more realistic heart model.

Of interest is that, despite of the simple ventricular model used in the present simulation study (a cube), we are able to simulate and maintain the reentrant VT. Figure 4.3 shows the rotating patterns of both the intracardiac activation sequence and the BSPMs. Although the present reentry simulation is essentially a 2D model, the simulated body surface ECG waveform shows clear characteristics of VT. This suggests that a simple reentry model may be able to simulate the main features of a reentrant VT. In the future investigation, the 3D reentry simulation should be conducted and corresponding inverse imaging performed. This 2D feature of the reentry simulation may explain the

small localization error, which may increase in a 3D reentry simulation. In the future investigations, more realistic heart models should be used to simulate reentrant arrhythmia. While it is beyond the scope of the work, realistic situations such as the anatomy and conduction system of the heart, as well as more realistic information regarding NMZ would need to be included in the modeling effort [Wei et al 1995].

Reentry is generally divided into three categories: (1) circus movement, (2) reflection, and (3) Phase 2 reentry [Antzelevitch, 2001]. The reentry we induced in the present study belongs to the first category. With different settings of anatomical or functional obstacles in cardiac models, various reentries can be simulated due to circus movement. While future investigations should include simulation of various types of reentry, the present promising results suggest the feasibility of localizing the site of origin of reentry with circus movement. If the site of origin of reentrant VT can be localized noninvasively, it will provide important information guiding catheter mapping in the vicinity of it to further determine the detailed structure of the reentry.

It is well known that the conductive medium between cardiac electrical sources and body surface electrodes is not the infinite homogenous conductor. The electrical potential is rather a summation of contributions from the primary cardiac sources and those by the secondary sources, reflecting the contribution from conductivity inhomogeneity. Therefore, the simple torso model we used merely represents the contributions from the primary cardiac sources. While a more realistic torso volume conductor model is desirable to obtain precise simulation of the torso volume conductor, we have adopted the

simple torso model in the present study for the purpose of initially testing the feasibility of the proposed approach to localize the site of origin of reentry. Future studies should address the effects of conductivity inhomogeneity and use more realistic torso models and heart model [Wei et al 1995], in order to obtain accurate quantitative simulation of BSPMs corresponding to cardiac arrhythmia. The present simulation results indicate that the simple heart-torso model used in this study is able to simulate the major characteristics of reentrant VT in both the space and time domains. Therefore, the present forward model offers a simplified yet reasonable computational setting to simulate the reentrant VT and provides an approximation of relationship between the reentrant VT and BSPMs.

The key hypothesis being tested in the present simulation study is whether such a model-based imaging approach can localize the site of origin of reentry from noninvasive BSPMs. While many efforts have been made to solve the cardiac inverse problem, including equivalent dipole solutions [Ideker et al 1977; Mirvis et al 1977; Savard et al 1980; Gulrajani et al 1984], epicardial potential solutions [Barr et al 1977; Frazone et al 1978; Shahidi et al 1994; Throne and Olson 1994; Oster et al 1997; Greensite and Huiskamp 1998; Cheng et al 2003], heart surface activation imaging [Cuppen and Van Oosterom 1984; Huiskamp and Greensite 1997; Tilg et al 2002], and the recently introduced 3D electrocardiographic imaging [He and Wu 2001; He et al 2002; Li and He 2001; Ohyu et al 2002; Skipa et al 2002; Liu et al 2006b], the present study represents, to our knowledge, the first report on localization of site of origin of reentry with the aid of a reentry-model. The unique feature of such approach is that the electrophysiological

properties are incorporated in the inverse approach, thus enhancing substantially the performance of the inverse solution. Also, the obtained inverse solutions are direct electrophysiological properties, instead of equivalent cardiac sources.

The location and size of NMZ are important parameters in generating reentrant VT. We have assessed the effect of location of NMZ and our simulations results (not shown) indicate that the present model-based imaging approach is not sensitive to the location of NMZ being simulated, if it is not too close to the heart surface. The size of NMZ is considered to be a priori knowledge in the present study, which may be obtained from non-electrocardiographic imaging modalities.

Note that we only altered the parameters for UDB in the inverse procedure as compared with in the forward procedure. While the result for UDB-alteration is promising and suggests the feasibility of the proposed approach, the basic characteristics of the cardiac model remain as the same in both the forward and inverse procedures. This is the limitation of computer simulations and the ultimate validation of the proposed approach will need to be demonstrated in an experimental setting.

In summary, the present study represents, to our knowledge, the first investigation with regard to the feasibility of localizing the site of origin of reentry with the aid of a reentry heart model. The promising results suggest that by taking a priori electrophysiological information into consideration in the model-based inverse estimation process, one can accurately localize the site of origin of reentrant ventricular tachycardia from noninvasive BSPMs. The availability of such information regarding the site of

origin of reentrant arrhythmia would provide important information aiding catheter based ablations of reentrant arrhythmias. The present study suggests the feasibility of characterizing more complex arrhythmias within the 3DCEI scheme.

5. Calculating the cardiac intramural potentials with finite element method

5.1. Objective

In our previous studies, the boundary element method (BEM) was employed to numerically solve the governing equations in the volume conductor, and thus to obtain the relationship between the cardiac sources and the field measurements. BEM requires less computational load with satisfactory accuracy. However, it has some limitations. First, the forward solutions must be on a surface defined in the boundary element model (That's why it is called boundary element method), for instance, the body surface. Second, the volume conductor must be assumed piecewise homogeneous. In other words, the anisotropic conductivity in the heart cannot be fully incorporated into the BEM calculation.

To overcome those limitations, the finite element method (FEM) is has been proposed. FEM is a volume numerical method which can handle both the inhomogenity of conductivity [Yan et al 1991] and the anisotropy of conductivity [Kim et al 2003]. FEM has been used in EEG forward modeling in our group to calculate cortical/scalp potentials from equivalent current dipoles [Zhang et al 2004]. Similarly, the cardiac activities can also be represented by distributed equivalent sources. The aim of the present study is to apply FEM in the cardiac forward calculation. Our goals includes 1) applying FEM to calculate the field measurements (body surface potentials, intracavitary potentials, etc) from equivalent current densities; 2) incorporating cardiac anisotropy into the forward calculation; 3) calculating the intramural potentials inside the myocardium

with the aid of FEM. Simulation studies are to be conducted to investigate the performance of FEM.

5.2. Methods

5.2.1. The construction of the finite element model

The first step of building a finite element (FE) model is obtaining the boundary element (BE) models of the needed surfaces, including the torso, the heart, the heart chambers and other related surfaces. The CT/MRI data of the subject is segmented and the surfaces of the torso, heart and heart chambers are detected. In our practice, Matlab and Curry 5 (Compumedics Neuroscan Inc., NC) are used for image segmentation. Then the surfaces are defined with the triangle meshes to obtain the BE models.

Those BE models are then transformed to the volume definition models, which are required for meshing the finite element model. This procedure is conducted by utilizing the software Rhinoceros 3.0 (Robert McNeel & Assoc., WA), in which the Non-Uniform Rational B-Splines (NURBS) is used to get the accurate mathematical description of 3D geometry. Finally, the 3D NURBS geometry of the torso-heart-catheter is meshed into tetrahedral elements to obtain the finite element (FE) model, by using the software Ansys 8.1 (ANSYS, Inc., PA). Figure 5.1 shows an example of meshed FE model of a pig, which includes torso, heart, blood cavities and a balloon catheter in the blood cavity.

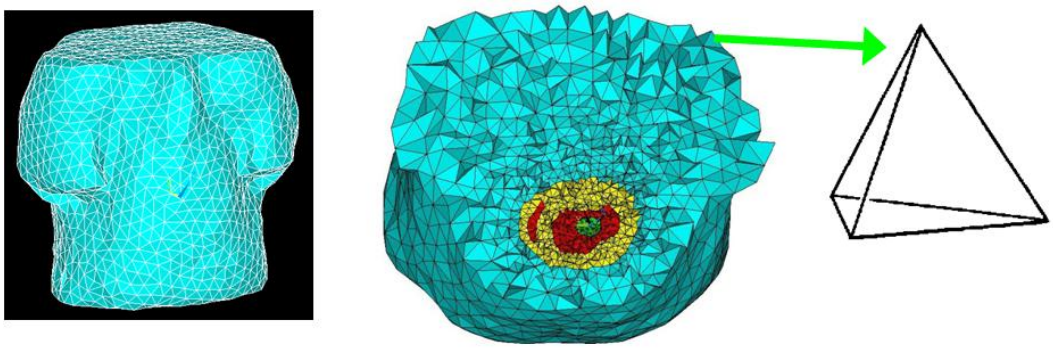

Figure 5.1. Finite element model of a pig.

5.2.2. The finite element calculation

By applying the bidomain theory, the extracellular electrical potential Φ within the thorax Ω can be solved from the following Poisson's equation:

$$\nabla \cdot [(\sigma_i + \sigma_e)\nabla\phi] = \nabla \cdot j \qquad \text{in } \Omega;\ \sigma(\nabla\phi)\cdot n = 0 \text{ on } S \tag{5.1}$$

$$j = -\sigma_i \nabla V_m \text{ in } \Omega \tag{5.2}$$

where σ_i and σ_e are the intracellular and interstitial conductivity tensor, j the equivalent current density, V_m the transmembrane potential, and n the outward unit normal to the surface S, which includes the body surface and the surface of the catheter (if a nonconductive catheter is included in the model).

By rewriting equation (5.1), we can get such a matrix equation

$$\nabla \cdot \left(\sigma \begin{bmatrix} \partial\Phi/\partial x \\ \partial\Phi/\partial y \\ \partial\Phi/\partial z \end{bmatrix} \right) = \nabla \cdot \left(\begin{bmatrix} \sigma_{11} & \sigma_{12} & \sigma_{13} \\ \sigma_{21} & \sigma_{22} & \sigma_{23} \\ \sigma_{31} & \sigma_{32} & \sigma_{33} \end{bmatrix} \begin{bmatrix} \partial\Phi/\partial x \\ \partial\Phi/\partial y \\ \partial\Phi/\partial z \end{bmatrix} \right) = -\sum_{\Omega} I_s \tag{5.3}$$

Where $I_s = -\nabla \cdot j$. Then (5.3) can be expanded as:

$$\sigma_{11}\frac{\partial^2\Phi}{\partial x^2}+\sigma_{22}\frac{\partial^2\Phi}{\partial y^2}+\sigma_{33}\frac{\partial^2\Phi}{\partial z^2}+(\sigma_{12}+\sigma_{21})\frac{\partial^2\Phi}{\partial x\partial y}+(\sigma_{13}+\sigma_{31})\frac{\partial^2\Phi}{\partial x\partial z}$$
$$+(\sigma_{23}+\sigma_{32})\frac{\partial^2\Phi}{\partial y\partial z}=-\sum_{\Omega} I_s \tag{5.4}$$

By using the variational principle, the variational equation is obtained from (5.4)

$$F(\Phi)=\iiint_{\Omega}\begin{pmatrix}\sigma_{11}\left(\frac{\partial\Phi}{\partial x}\right)^2+\sigma_{22}\left(\frac{\partial\Phi}{\partial y}\right)^2+\sigma_{33}\left(\frac{\partial\Phi}{\partial z}\right)^2+(\sigma_{12}+\sigma_{21})\frac{\partial\Phi}{\partial x}\frac{\partial\Phi}{\partial y}\\+(\sigma_{13}+\sigma_{31})\frac{\partial\Phi}{\partial x}\frac{\partial\Phi}{\partial z}+(\sigma_{23}+\sigma_{32})\frac{\partial\Phi}{\partial y}\frac{\partial\Phi}{\partial z}\end{pmatrix}d\Omega+2\iiint_{\Omega}\Phi I_s \tag{5.5}$$

Equation (5.5) can be restated in matrix form

$$F(\Phi)=\sum_{e=1}^{N_e}[\Phi]^T\left[S^e\right][\Phi]+\sum_{d=1}^{N_d}[\Phi]^T\left[G^d\right] \tag{5.6}$$

where N_e is the number of elements in the FEM model and N_d is the number of elements in which the equivalent current sources are placed.

$$S_{ij}^e=\iiint_{\Omega^e}\begin{pmatrix}\sigma_{11}\frac{\partial N_i}{\partial x}\frac{\partial N_j}{\partial x}+\sigma_{22}\frac{\partial N_i}{\partial y}\frac{\partial N_j}{\partial y}+\sigma_{33}\frac{\partial N_i}{\partial z}\frac{\partial N_j}{\partial z}\\+2\sigma_{12}\frac{\partial N_i}{\partial x}\frac{\partial N_j}{\partial y}+2\sigma_{13}\frac{\partial N_i}{\partial x}\frac{\partial N_j}{\partial z}+2\sigma_{23}\frac{\partial N_i}{\partial y}\frac{\partial N_j}{\partial z}\end{pmatrix}d\Omega$$

$$G_i^d=\sum_{\Omega^d} I_s N_i d\Omega \tag{5.7}$$

where N_i, N_j refer to the assumed shape functions, which are the polynomial approximation function defined in local coordinates.

According to the Galerkin method, we can get

$$\frac{\partial F}{\partial \Phi_i} = 2\sum_{j=1}^{n} s_{ij}\Phi_j + g_i = 0 \tag{5.8}$$

In matrix format:

$$2[S][\Phi] = -[G] \tag{5.9}$$

The electrical potential Φ can be obtained at every node of the finite element model by solving the set of linear equations given by equation (5.9). In this way, the potentials at the balloon catheter electrodes, on the body surface and inside the myocardium can be simulated after the equivalent current sources have been defined. In our algorithm, first-order finite element method is used.

5.2.3. Incorporating anisotropy into FEM

Since myocardial fiber exists in the heart, the conductivity in the myocardium is anisotropic. For this reason, anisotropy should be incorporated into the forward calculation. In equation (5.3), we already defined the conductivity σ as a tensor, and thus anisotropy is incorporated into the Poisson's equation. In practice, each element of the FE model is assigned with a conductivity tensor indicating the fiber orientation at the

location of the this element, and those local conductivity tensors are utilized in equation (5.5)-(5.9).

In local Cartesian coordinate system where the z axis is always oriented along the fiber orientation, the conductivity tensor can be described as

$$\sigma' = \begin{bmatrix} \sigma_t & & \\ & \sigma_t & \\ & & \sigma_l \end{bmatrix} \tag{5.10}$$

where σ_l is the conductivity along the fiber orientation and σ_t is the conductivity transverse to the fiber orientation. σ_l is much larger than σ_t. For each FE element, the conductivity tensor is first defined in the local Cartesian coordinates as shown in equation (5.10). Then the conductivity tensor needs to be transferred into the global coordinate system for further calculation, by employing a rotation matrix A:

$$\sigma = A\sigma' A^T \tag{5.11}$$

The matrix A is calculated in the following way. We assume the local coordinates are characterized by the unit vectors e_1, e_2, e_3, where e_3 is always oriented along the fiber orientation. The global coordinates are characterized by unit vectors e_x, e_y, e_z, and A can be expressed as

$$A = \begin{bmatrix} (e_1 \cdot e_x) & (e_2 \cdot e_x) & (e_3 \cdot e_x) \\ (e_1 \cdot e_y) & (e_2 \cdot e_y) & (e_3 \cdot e_y) \\ (e_1 \cdot e_z) & (e_2 \cdot e_z) & (e_3 \cdot e_z) \end{bmatrix} \tag{5.12}$$

Thus the conductivity tensor in the global coordinates is obtained and can be used in equation (5.3)-(5.9).

5.2.4. Calculation of intramural potentials

The equivalent current densities are distributed in the myocardium, so the calculation of intramural potentials is a near field problem -- the cardiac sources and the observation sites are very close to each other. Different with the far field calculation such as body surface potentials, the numerical approximation in the source model may largely affect the quality of the calculated near field solutions. As result, a very fine source model is required to ensure the accuracy of calculation. In practice, the heart is divided into thousands of small segments and the cardiac activity in each segment is represented by a regional equivalent current density as shown in equation (5.2).

The high density of the cardiac sources brings another concern. If the observation site is too close to the location of a cardiac source, singularity may occur due to nature of the forward calculation. So we only choose observation sites which don't overlap with the locations of the equivalent current densities. If we do want to calculate the potential where a current source exits, Gaussian interpolation is applied to obtain the approximated value instead of direct calculation. Figure 5.2 shows the density of the equivalent current densities and the picked observation sites in a realistic heart model.

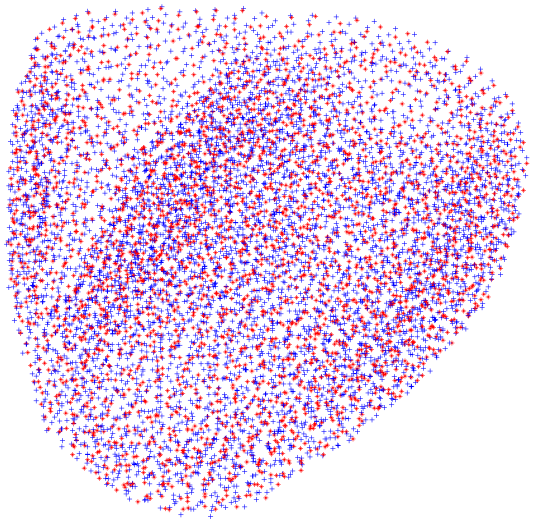

Figure 5.2. RED: locations of the equivalent current densities; BLUE: observation sites.

5.3. Simulation and results

The performance of the finite element method was first tested in a realistic human model which was described in [He et al 2007]. Both body surface potentials and intracavitaty potentials were simulated under the heart's sinus rhythm. The physiologically reasonable results shown in Figure 5.3 suggests the validity of FEM.

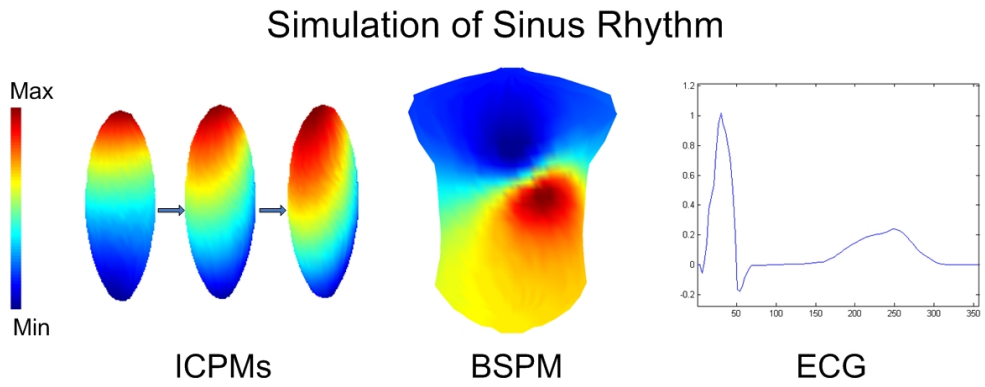

Figure 5.3. The simulated intracavitary potentials maps, body surface potential map and lead 2 ECG signal using finite element method. Extracted from [He et al 2007]

The extracullar potentials were also simulated and shown in Figure 5.4, where the heart is initially activated from the left ventricular posterior area. Figure 5.4(a) shows the simulation result when the anisotropy is considered. We can clearly see the wavefront of the propagation of the excitation and the continuous change of the potentials throughout the ventricles. The simulation result is physiologically reasonable. Figure 5.4(b) shows the simulation result when the heart is initially activated from the same location, but the anisotropy is neglected. By comparison, we can find that the conductivity anisotropy does affect the pattern of the excitation of the heart, especially in the later stage of activation. More results about reconstructing extracellular potentials will be presented and evaluated in chapter 6.

Finally, the simulated body surface potential maps are compared with the corresponding result calculated by using boundary element method. Since BEM cannot incorporate anisotropy into calculation, anisotropy is also neglected in FEM calculation. The averaged correlation coefficient between two sets of BSPMs over activation is as high as 0.99.

5.4. Conclusion

In the present study, finite element method is refined and applied in the cardiac numerical calculation. The simulation results suggest that the simulated body surface potentials, intracavitary potentials and extracellular cardiac potentials are physiologically reasonable. The simulated BSPMs by using FEM are consistent with the results by using

BEM. The cardiac anisotropy is also successfully incorporated into FEM. The application of FEM in 3DCEI approach will be presented in chapter 6.

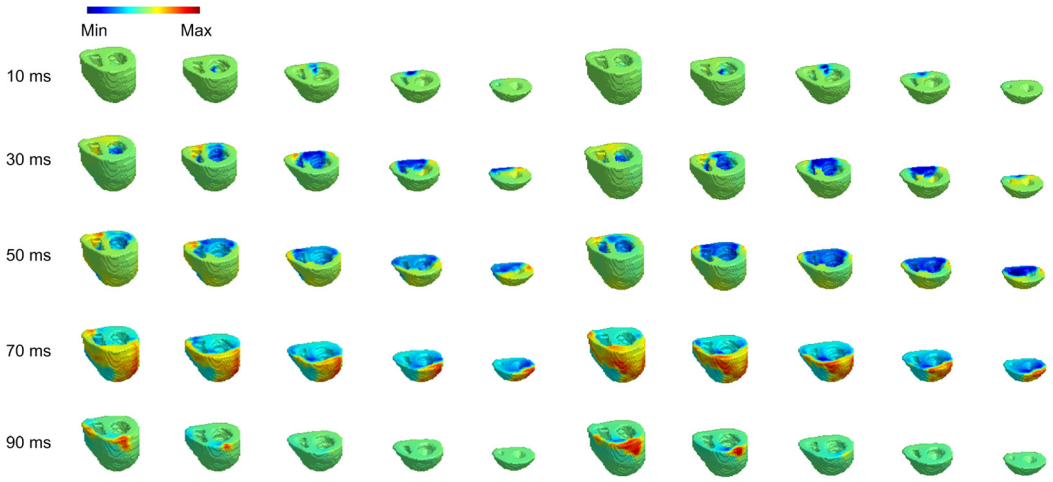

Figure 5.4. The simulated three-dimensional extracellular potentials when the heart is paced from left ventricular posterior when anisotropy is (a) considered; (b) neglected.

6. Estimation of three-dimensional cardiac activities from intracavitary potential maps

6.1. Objective

BSPM-based inverse approaches have been extensively investigated. Owing to the improvement of catheter technique, the intracavitary potentials have been utilized as the input of the inverse problem to estimate the endocardial potentials and subsequent activation sequence [Khoury et al 1995, 1998; Schilling et al 1998, Gornick et al 1999; Berrier et al 2004]. The endocardial inverse mapping technique is proved useful and has been commercialized in the Ensite system [Gornick et al 1999]. Compared to the direct mapping method used in CARTO system [Ben-Haim et al 1996; Gepstein et al 1997], the inverse mapping method is on beat-to-beat basis instead of sequential mapping, and so can better capture non-sustained arrhythmias. However, the mapping results are limited on the endocardial surface, which cannot directly characterize the intramural activities. While these endocardial mapping and inverse solutions show promise of offering a minimally invasive means of localizing and mapping cardiac electrical activity over the endocardial surface, no attempt has been made, to our knowledge, to image the three-dimensional cardiac electrical activity from the intra-cavity catheter recordings.

It has been reported that 3D mapping of cardiac activities could not only be a powerful tool for research on the mechanisms of arrhythmias [Witkowski and Corr 1984; Chung et al 1997; Zhang et al 2000; Chattipakorn et al 2003; Attin et al 2008] but could also guide the clinical management of cardiac arrhythmias in a more efficient way. Specifically, localization of the initial site of activation implies direct clinical benefits for

the management of arrhythmias caused by focal initiation, such as focal ventricular tachycardia and adenosine insensitive microreentry [Mittal 2008]. The localization of focal initiations has the potential of guiding ablative procedures. Secondly, mapping global ventricular activation sequence can provide an outlook of the cardiac activity as well as local details. Lastly, the estimated intramural electrograms could replace invasive intraoperative sensors to disclose the intrinsic characteristics of the heart excitation, in both spatial and temporal domains.

Clearly, the availability of a 3D tomographic imaging approach that could image cardiac electrical activity throughout the 3D myocardium will provide a much desired functional imaging means to assess cardiac electrical activity and provide an alternative guide to catheter ablation and other clinical applications. The goal of the present study is to a new approach for imaging 3D cardiac electrical activity from intracavitary electrical measurements, with the aid of the finite element method (FEM). The algorithm is developed from the BSPM-based 3DCEI approach, and its function and feasibility are evaluated in both simulation and animal studies in a control swine model. The first work is a series of simulation studies in a human model, regarding the capability of localizing the initiation site and estimating 3D activation sequence. The contents of the simulation studies including text, figures and tables were published in [He et al 2007]. Then studies are conducted in an animal model, including simulation on the function of estimating intramural potentials and animal validation on all the functions of the ICPM-based 3DCEI.

6.2. Principle of the inverse algorithm

Figure 6.1[He et al 2007] shows the schematic diagram of the inverse procedure. We adapted a heart-electrophysiological-model based inverse algorithm, which we have previously developed based on body surface potential maps (BSPMs) [He et al 2002]. A preliminary classification system which approximately determines cardiac status based on *a priori* knowledge and the measured intra-cavity potential maps (ICPMs) was used to estimate the initial pattern of myocardial activation by means of an artificial neural network [Li and He 2001]. According to the output of the preliminary classification system, the parameters of the heart computer model were initialized, and the corresponding ICPM was calculated using the FEM. The model's parameters were iteratively adjusted in an attempt to minimize the dissimilarity between the measured and the heart-model-generated ICPMs, employing a multi-objective nonlinear optimization procedure. The following equation:

$$\min_{x \in X}(E(x)) = \min_{x \in X} f(E_{CC}(x), E_{\text{int\_}CC}(x)) \tag{6.1}$$

was solved with the aid of the Simplex Method [Kowalik and Osborne 1968], where (a) $E_{CC}(x)$ is constructed with the average correlation coefficient (CC) between the measured and simulated ICPMs from instant T_1 to instant T_2 of the cardiac excitation after detection of initial activation and (b) $E_{int\_CC}(x)$ is constructed with the CC between the integral of the measured ICPMs and the integral of the simulated ICPMs. The x is a parameter vector consisting of heart model parameters to be optimized in the process. The iteration will stop when the convergence criteria are satisfied.

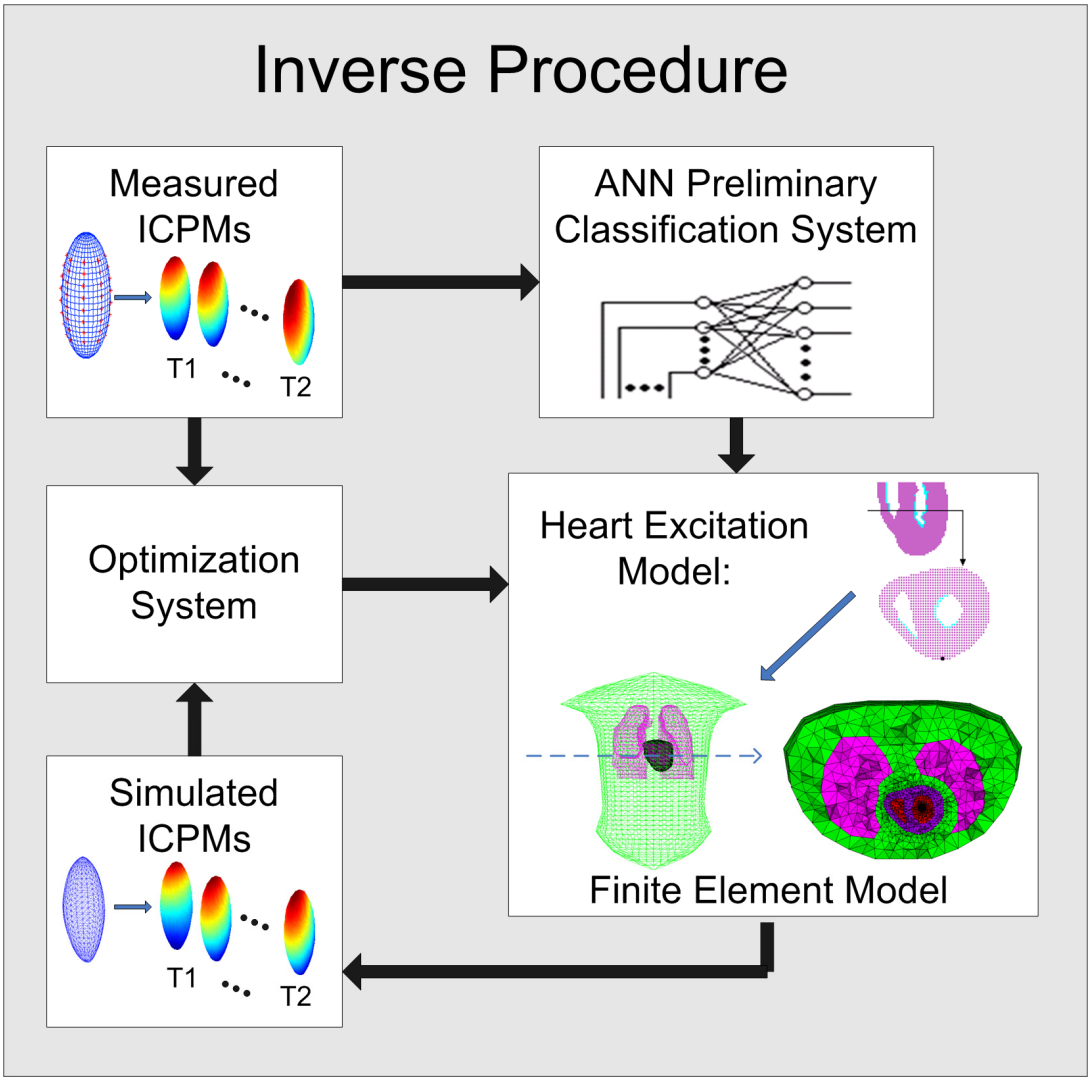

Figure 6.1. The schematic diagram of the three-dimensional cardiac electrical imaging approach from the intra-cavity recordings. ICPM: Intra-cavity potential map. BSPM: Body surface potential map. See text for details.

6.3. Simulation in a human model

In the present study, we evaluated the performance of the ICPM-based 3DCEI approach on localizing the initiation site of activation and estimating the global activation sequence. The robustness of the algorithm under large noise or geometrical uncertainties were also evaluated in simulation.. The results of estimating intramural potentials from

ICPMs will be presented in next session of the chapter, in both simulation and animal experiments.

6.3.1. Forward modeling

In the present study, the forward solution of intracavitary potentials was obtained by using the FEM with the aid of a cellular-automaton heart model [Li and He 2001; He et al 2002, 2003]. The heart model was constructed from CT scans of a human subject and contains about 65,000 myocardial cell units, at which an action potential is assigned. The anisotropic propagation of excitation in the ventricular myocardium is incorporated into this computer heart model [He et al 2002, 2003] according to literature [Nenonen et al 1991; Lorange and Gulrajani 1993; Wei et al 1995; Fischer et al 2000]. The myocardial fiber orientations rotated counterclockwise over 120^0 from the outermost layer (epicardium, -60^0) to the innermost layer (endocardium, $+60^0$) with identical increment between the consecutive layers. All the units on the same myocardial layer of ventricles had identical fiber orientations. The conduction velocity was 0.8 m/s along the fiber and 0.3 m/s transverse to the fiber. The heart model was made up of about 65,000 myocardial cell units spaced by 1.5 mm. Each myocardial unit's parameters, such as the pattern of action potential and the vector of local fiber orientation, were set individually. We considered the anisotropy of intracellular conductivities when calculating the instantaneous current sources in the cellular automaton model. The conductivity tensor at each cell unit was computed from the local fiber orientation. The three orthogonal components of the current source at each cell unit were respectively computed as the product of the negative spatial gradient of instantaneous transmembrane potential for

each of the three directions and the corresponding intracellular conductivity at the same direction. Based on the bidomain theory, the extracellular electrical potential Φ within the thorax Ω can be solved from equations (5.1) and (5.2).

Based on the CT images of a human subject, a finite element (FE) model was built to simulate the realistic geometry thorax volume conductor. The CT images were segmented, edge-detected, and contoured for the torso, lungs, epicardial and endocardial surfaces, respectively. The surface contours were meshed by triangles to build a boundary element (BE) model. The BE model of a balloon catheter in an inflated status was embedded into (located approximately in the center of) the cavity of the left ventricle. The triangulated surface models were then transformed to volume definition model by Rhinoceros software (Robert McNeel & Assoc., WA) using Non-Uniform Rational B-Splines (NURBS), which is an accurate mathematical description of 3D geometry, in order to generate FE meshes. The FE model was obtained by meshing the integrated NURBS geometry model. The heart-torso-catheter FE model was made up of 20,423 nodes and 118,660 first-order tetrahedral elements. The tetrahedral elements within the myocardium and the blood mass had finer resolution as compared to other areas. The torso, lungs and blood mass were assumed to be isotropic conductors. The anisotropy of cardiac tissue was incorporated into the computer model as described above. The conductivities of different tissues were set as follows in the FE model: torso (0.20 S/m), lungs (0.08 S/m), blood mass (0.6 S/m), cardiac tissue (interstitial: 0.6 S/m along the fiber orientation and 0.15 S/m transverse to the fiber orientation; intercellular: 0.3 S/m along the fiber orientation and 0.075 S/m transverse to the fiber orientation). The inside

of the catheter was assumed non-conductive, simulating the commercial balloon catheter produced by St Jude Medical.

The cardiac current sources j were simulated by means of a cellular-automaton heart model [Li and He 2001] via equation (5.1) and used to evaluate the electrical potential field in the FE mode via equation (5.2). The detailed FEM algorithm was described in Chapter 5. Sixty-four electrodes were uniformly distributed over the catheter surface and the electrical potentials at these electrodes were calculated according to a certain cardiac status (such as sinus rhythm or pacing).

6.3.2. Simulation protocol

Computer simulations using a pacing protocol were used to evaluate the performance of the present ICPM-based 3-D cardiac electrical imaging approach. Under such pacing protocol, the parameters x in equation (6.1) consisted of the pacing sites. Twelve sites were selected and paced individually from the following regions throughout the ventricles: BA: basal-anterior; BRW: basal-right-wall; BP: basal-posterior; BLW: basal-left-wall; BS: basal-septum; MA: middle-anterior; MP: middle-posterior; MLW: middle-left-wall; MS: middle-septum; AA: apical-anterior; AP: apical-posterior; AS: apical-septum.

For each pacing simulation, assuming the peak-peak value of the intra-cavity potential is 5 mV, Gaussian white noise (GWN) of standard deviation of 25-μV was added to the calculated ICPMs to simulate the noise-contaminated ICPM measurements, which served as the input of the inverse approach. Random noise (average value of

1.2mm) was also added to the electrode positions to simulate the electrode position uncertainty. Effects of catheter position shift were also evaluated by introducing 5 mm shift of the catheter. These parameter uncertainty and variation were introduced to test the robustness of the proposed approach. The parameters were chosen based on possible ranges of the values in an experimental setting.

The 3-D inverse solutions were quantitatively evaluated by two measures: localization error (LE) and relative error (RE). The LE is defined as the distance from the pacing site to the site of initiation of corresponding activation. The RE is defined as follows:

$$RE = \sqrt{\sum_{i=1}^{N} (t_i^{INV} - t_i^T)^2} \Big/ \sqrt{\sum_{i=1}^{N} (t_i^T)^2} \qquad (6.2)$$

where N is the number of the ventricular cell units, t_i^T is the true activation time of the i^{th} cell unit and t_i^{INV} is the inversely estimated activation time of the i^{th} cell unit.

6.3.3. Results

A typical example of the present inverse solution during single-site pacing is shown in Figure 6.2 (left panel). The ICPMs from T_1=21ms to T_2=48ms after the onset of pacing were used to inversely estimate the location of the pacing site and the ventricular activation sequence. The localization error (LE) was assessed by the distance from the localized site of origin of activation to the true pacing site. The estimation error for the activation sequence was assessed by relative error (RE) between the true and estimated

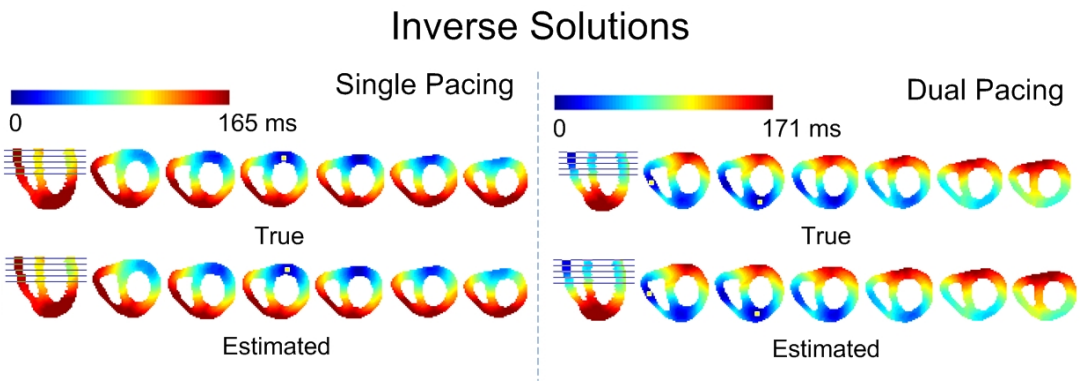

Figure 6.2. Two typical examples of the three-dimensional cardiac electrical inverse solutions from the ICPM, during single-site pacing (left) and dual-site pacing (right). The true and estimated activation sequences are shown by isochrones of one longitudinal section and six transverse sections, respectively. The locations of the true and estimated pacing sites are illustrated by yellow dots on the isochrone maps.

activation sequences. The simulation results during single-site pacing over 12 pacing sites are shown in Table 6.1. The mean and standard deviation of the LE and RE were 1.88±0.92mm and 0.03±0.01, respectively, when only additive measurement noise of 25-μV was considered. When both additive measurement noise and electrode position uncertainty with an average value of 1.2mm were considered, the mean and standard deviation of the LE and RE become 2.76±1.22mm and 0.04±0.02, respectively. When both additive measurement noise and catheter shift of 5mm were considered, the mean and standard deviation of the LE and RE became 4.84±0.63mm and 0.08±0.02, respectively.

Effects of number of recording electrodes over the catheter are shown in Table 6.2, where 32 and 128 electrodes were uniformly distributed over the catheter surface. Only measurement noise with standard deviation of 25-μV was considered in this case. The LE and RE became 2.18±0.73mm and 0.03±0.01 for 32-electrodes, and 1.71±1.22mm and 0.02±0.02 for 128 electrodes. Compared with the results using 64 electrodes, no

significant effects were observed when using 32 or 128 electrodes, considering other possible error sources, such as a possible shift in position of the catheter (5 mm shift led to an averaged localization error of 4.84mm).

Table 6.1. Localization error (LE) of the pacing site, and relative error (RE) of the reconstruction of activation sequence, from the 64-electrodes ICPMs during single site pacing.

Region	*25 μV Noise*		*25 μV Noise + Electrode Uncertainty*		*25 μV Noise + 5mm Catheter Shifting*	
	LE (mm)	RE	LE (mm)	RE	LE (mm)	RE
BA	3.35	0.04	1.50	0.02	4.74	0.07
BLW	3.35	0.04	3.35	0.04	5.61	0.08
BS	2.12	0.03	1.50	0.01	4.74	0.09
BRW	0.00	0.00	5.61	0.08	4.74	0.06
BP	1.50	0.02	3.00	0.04	3.35	0.07
MA	2.60	0.04	2.12	0.03	4.97	0.09
MP	2.12	0.03	3.67	0.04	4.97	0.09
MLW	1.50	0.02	2.12	0.04	4.74	0.07
MS	1.50	0.04	2.12	0.04	4.97	0.10
AP	1.50	0.03	3.67	0.05	6.00	0.11
AS	1.50	0.02	1.50	0.02	4.74	0.10
AA	1.50	0.03	3.00	0.06	4.50	0.08
Mean	1.88±0.92	0.03±0.01	2.76±1.22	0.04±0.02	4.84±0.63	0.08±0.02

Table 6.2. Localization error (LE) of the pacing site, and relative error (RE) of the reconstruction of activation sequence, from the 32-electrodes and 128-electrodes ICPMs during single site pacing.

Region	*32 electrodes*		*128 electrodes*	
	LE (mm)	RE	LE (mm)	RE
BA	3.35	0.04	3.35	0.04
BLW	3.35	0.04	3.35	0.04
BS	2.12	0.03	1.50	0.01
BRW	3.00	0.05	0.00	0.00
BP	2.12	0.04	1.50	0.02
MA	2.60	0.04	2.12	0.03
MP	2.12	0.03	2.12	0.03
MLW	1.50	0.02	1.50	0.02
MS	1.50	0.04	0.00	0.00
AP	1.50	0.03	0.00	0.00
AS	1.50	0.02	2.12	0.04
AA	1.50	0.03	3.00	0.06
Mean	2.18±0.73	0.03±0.01	1.71±1.22	0.02±0.02

The performance of the ICPM-based inverse approach was also evaluated by the dual-site pacing. Twelve pairs of myocardial cell units in a seven-layer myocardial region adjacent to the atrial-ventricular (AV) ring were randomly selected to simulate two localized regions of activation. The similar noise and uncertainty conditions were simulated as in the single pacing protocol. Figure 2 (right panel) shows a typical example of the inverse solutions during dual-site pacing with GWN of 25-μV being added to the forward-calculated ICPMs. Table 6.3 lists the LE and RE for all 12 pairs of pacing sites. On average, the RE of the activation sequence were 0.04±0.01, and the LE over 24 initial activation sites was 2.28±1.15mm, when only additive measurement noise with standard

Table 6.3. Localization error (LE) of the pacing sites, and relative error (RE) of the reconstruction of activation sequence, from the 64-electrodes ICPMs during dual site pacing.

Trial	25 μV Noise		25 μV Noise + Electrode Uncertainty		25 μV Noise + 5 mm Catheter Shifting	
	LE (mm)	RE	LE (mm)	RE	LE (mm)	RE
1	1.50&3.35	0.03	2.60&6.00	0.06	4.74&6.36	0.09
2	3.35&1.50	0.04	3.35&1.50	0.04	6.87&6.18	0.13
3	0.00&4.97	0.03	2.12&3.00	0.03	4.97&5.61	0.08
4	3.35&1.50	0.04	3.35&1.50	0.04	3.35&3.35	0.06
5	1.50&2.12	0.03	2.12&2.60	0.04	3.35&3.67	0.08
6	3.35&3.35	0.05	5.41&7.79	0.09	5.61&5.61	0.08
7	2.12&2.12	0.04	2.60&3.35	0.06	3.00&2.60	0.04
8	3.00&2.12	0.04	6.87&2.60	0.08	1.50&4.97	0.07
9	1.50&3.35	0.03	1.50&3.35	0.04	2.12&4.24	0.08
10	2.12&1.50	0.03	2.12&2.12	0.03	5.41&4.24	0.08
11	0.00&1.50	0.01	2.12&6.18	0.08	4.74&6.18	0.09
12	2.12&3.35	0.05	1.50&3.35	0.05	3.35&6.71	0.12
Mean	2.28±1.15	0.04±0.01	3.29±1.81	0.05±0.02	4.53±1.49	0.08±0.02

deviation of 25-μV was considered. When both additive measurement noise and electrode position uncertainty with an average value of 1.2mm were considered, the mean and standard deviation of the LE and RE increased to 3.29±1.81mm and 0.05±0.02, respectively. When both additive measurement noise and catheter shift of 5mm were

considered, the LE and RE were further increased to 4.53±1.49mm and 0.08±0.02, respectively.

Table 6.4. Localization error (LE) of the pacing sites, and relative error (RE) of the reconstruction of activation sequence, from the 32-electrodes and 128-electrodes ICPMs during dual site pacing.

Trial	*32 electrodes*		*128 electrodes*	
	LE (mm)	RE	LE (mm)	RE
1	1.50&3.35	0.03	1.50&3.35	0.03
2	3.35&1.50	0.04	3.35&1.50	0.04
3	1.50&4.74	0.05	1.50&4.74	0.05
4	3.00&2.12	0.04	3.00&2.12	0.04
5	2.12&2.60	0.04	2.12&2.60	0.04
6	3.35&3.35	0.05	3.35&4.50	0.05
7	2.12&0.00	0.02	2.12&0.00	0.02
8	3.00&2.12	0.04	3.00&2.12	0.04
9	1.50&3.00	0.05	2.12&1.50	0.04
10	3.35&3.00	0.05	2.12&1.50	0.03
11	0.00&1.50	0.01	0.00&1.50	0.01
12	2.12&3.35	0.05	2.12&3.35	0.05
Mean	2.40±1.11	0.04±0.01	2.30±1.16	0.04±0.01

Effects of number of recording electrodes over the catheter are shown in Table 6.4 during dual site pacing, where 32 and 128 electrodes were uniformly distributed over the catheter surface. Only measurement noise with standard deviation of 25-μV was considered in this case. The LE and RE were 2.40±1.11mm and 0.04±0.01 for 32-electrodes, and 2.30±1.16mm and 0.04±0.01 for 128 electrodes.

6.3.4. Discussion and conclusion

We have evaluated the performance of the proposed ICPM-based 3D inverse imaging approach in simulation. We used the FEM to solve the forward problem and a cellular-automaton heart model for simulating ventricular activation. The feasibility of imaging cardiac activation sequence and localizing the site of initiation of activation has been shown in computer simulations using single-site and dual-site pacing protocols. The

present promising simulation results (on average 2-3 mm localization error for single-site pacing, and 2.6-3.3mm localization error for dual-site pacing, when there is no catheter position shift; on average less than 5 mm localization error when there is catheter position shift), suggest the potential clinical applications of this new approach to accurately localize site of origin of ventricular activation from the widely used catheter procedure in a clinical setting.

The largest localization and reconstruction errors occurred when there is a shift in position of the catheter. For a 5 mm shift of catheter position, the resulting averaged localization errors are 4.84 mm and 4.53 mm, respectively, for single site and dual site pacing. This data suggest that there is a need to develop a technique to accurately determine the position and geometry of intra-cavity catheter in real time for clinical applications. On the other hand, the present simulation results also suggest that the intrinsic error of the present 3-D cardiac imaging approach from ICPMs is low, if there is no such systematic shift in probe position. Note that while we have evaluated effects of measurement noise and geometry and sensor location uncertainty in the present simulation study, we assumed that the forward transfer matrix represents well the lead field relating the electrical sources within the myocardium to the electrode sensors. The realistic effect of such possible distortion would have to be assessed in an experimental setting in either an animal model (e.g. [Zhang et al 2005]) or in human subjects (e.g. [Li et al 2003]).

Compared with the BSPMs which are measured over the torso surface, the ICPMs were simulated in the present study within the left ventricle. While the right ventricular wall had a larger source-to-sensor distance, the present simulation results indicated that the proposed approach can image electrical activity from both the left ventricle and the right ventricle. This shall be explained by the fact that electrode sensors record electrical potentials via volume conduction and there are no insulating materials separating the left ventricle from the right ventricle.

Compared to the body surface recordings, the intra-cavity recordings have the advantage of high signal-to-noise ratio (SNR), since the effect of environmental noise is smaller in the cavity than on the body surface and the signal is larger within the intra-cavity compared due to smaller distance from the cardiac sources to the sensors. The smoothing effect caused by the volume conductor also has less effect on the intra-cavity potentials, due to the vicinity of catheter probe and the myocardium [Velipasaoglu et al 2000]. Thus the ICPM-based cardiac electrical imaging, as a minimally invasive procedure, may offer higher spatial resolution, and maybe easier to be used in combination with the ablative catheter or catheters for other purposes in a single procedure. On the other hand, the BSPM-based cardiac electrical imaging is a complete noninvasive procedure, although the smearing effect of the torso volume conductor may be larger than the ICPM-based results. Future investigations should be made to compare the ICPM-based and BSPM-based imaging results.

As the catheter mapping is widely practiced in a clinical setting to aid catheter ablation, the ICPM based endocardial potential inverse solutions have been widely used in clinical electrophysiology labs to aid catheter ablation [Gornick et al 1999]. Currently such endocardial mapping based procedures are widely used for managing atrial arrhythmias, in which the thin wall of atria may explain the current clinical success of the surface approach. The present work is moving one step further from the endocardial surface mapping to the 3D cardiac imaging of electrical activity, based on the electrical potential recordings on a catheter. As the ventricular walls are much thicker than those of atria, the ability of performing 3D electrical imaging may have a significant impact on clinical practice to manage ventricular arrhythmias. The present computer simulation studies have demonstrated the feasibility of this new approach, and its performance in localizing and imaging site of activation and activation sequence during single and dual pacing.

The present study, to our knowledge, represents the first effort in localizing and imaging cardiac electrical activity within the 3D volume of the heart from intracavitary electrical signals. Note that while we demonstrated the feasibility of imaging 3D cardiac activation from ICPMs by means of the implementation of using heart electrophysiological computer model as regularization, what we proposed is not necessarily limited to this particular implementation. In other words, other inverse regularization schemes not using a heart electrophysiological computer model (e.g. [Liu et al 2006b]) may also be used to solve the 3D ICPM-based inverse problem. Due to the wide acceptance of catheter mapping in a clinical setting, we believe the present proposed

approach represents an important advance of cardiac electrical imaging research. Further experimental validation of this new approach may establish the approach as a clinically useful tool for guiding catheter ablation of a variety of cardiac arrhythmias, aiding rationale determination of optimal locations of leads for cardiac resynchronization therapy, and other applications to management of cardiovascular disorders.

6.4. Validation and simulation studies in a swine model

In the present study, we reported the results of the new function proposed in chapter 5: estimation of intramural electrograms. To our knowledge, this is the first report of indirectly mapping 3D extracellular potentials from the intracavitary recordings or any other non-contact recordings. This newly proposed function of inversely estimating the intramural extracellular potentials was evaluated in simulation; then animal studies were conducted to experimentally evaluate all the functions of the 3DCEI approach. Ventricular pacing at different locations was conducted to simulate focal arrhythmogenic activities. The 3D locations of the initiation sites, the resultant activation sequences and the intramural electrograms were estimated by employing the 3DCEI approach and the results were evaluated with the aid of magnetic resonance imaging (MRI) and the Ensite® system.

6.4.1. Materials and Methods

Swine model and data collection

Control pigs (n=2) were employed in the present study. For each animal, pre-operative magnetic resonance imaging (MRI; ECG gated to end diastole) data were

acquired approximately 5-7 days before the *in vivo* mapping experiment to obtain the anatomical geometry information. The surgical preparation of these animals are the same with that in Chapter 3. The intracavitary potential mapping was conducted by employing the EnSite® 3000 noncontact mapping (NCM) system (St Jude Medical, Inc., St. Paul, MN) which consists of a 64-multielectrode array (MEA) mounted on a 9-Fr balloon catheter. The balloon catheter and a standard EP catheter were put into the left ventricle (LV). The 3D location of the roving catheter's electrode relative to the fixed, known position of the expanded balloon was obtained by the NCM system. 3D reconstructions of the LV chamber's endocardial geometry were created by moving the roving catheter around the chamber, while the system accumulated anatomic reference points.

For each animal, active-fixation pacing leads were screwed into the right ventricular apex (RVA) and the RV septum (RVS) (Model 3830, Medtronic, Inc., USA) to deliver intramural pacing. Endocardial surface pacing was accomplished by a quadripolar EP catheter in the LV at the following areas: LV anterior (LVAn), LV middle lateral (LVML), LV lower lateral (LVLL) and LV apex (LVA). The 3D locations of the endocardial pacing sites were recorded on the reconstructed LV geometry acquired with the NCM system. ICPMs were recorded by the MEA when pacing was conducted. After the completion of the data collection procedure, the heart was removed and fixed in formalin with the intramural pacing leads remaining in place. These isolated hearts were again MRI scanned to record the precise locations of the RV pacing sites.

Volume conductor modelling and 3D electrical imaging

The schematic diagram of the ICPM-based 3DCEI approach is shown in Figure 6.3. For each animal, a cellular-automaton heart-excitation model with over 100,000 cellular units (spatial resolution of 1.5 mm) and a heart-torso volume conductor model were constructed based on the pre-operative MRI scans and prior known physiological knowledge. Based on the bidomain theory, the field potential within the thorax was simulated from the equivalent current sources by solving Poisson's equation [He et al, 2007] with the aid of the finite element method (FEM). A finite element (FE) model was constructed based on the MR images and the NCM system's recording. The geometries of the torso and heart were obtained by segmenting the MR images, while the geometries and relative locations of the MEA and LV were recorded by the NCM system. In order to obtain the accurate location of the MEA in the heart-torso volume conductor, a registration procedure between the LV's endocardial surface extracted from the MR images and the corresponding surface recorded by the NCM system was performed. The registration method was described in chapter 3. After the registration, the coordinates of the MEA were transformed to the coordinate system of the heart-torso volume conductor, based on which the torso-heart-catheter FE model was constructed. Theoretically, the electric potential at every node of the FE model can be calculated when the electrical source is known, as described in chapter 5. The potentials at 64 nodes corresponding to the locations of the intracavitary electrodes in the MEA were extracted to constitute the ICPMs at a given time.

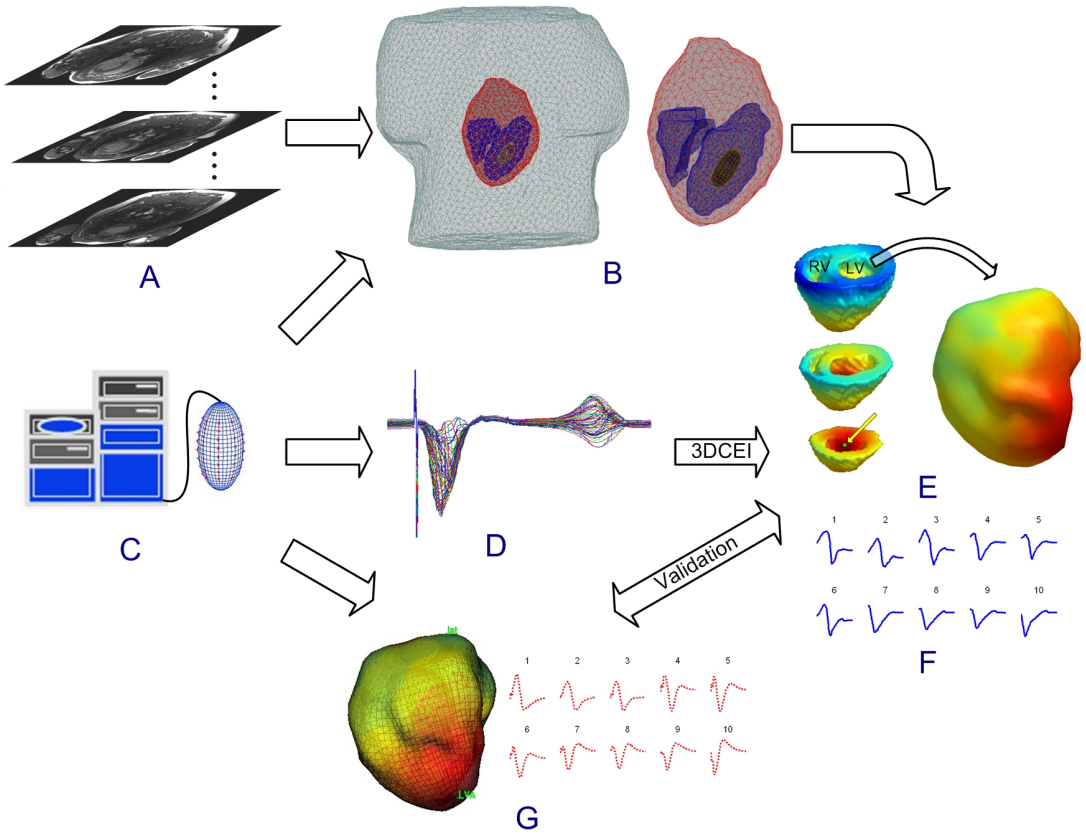

Figure 6.3. The schematic diagram of the ICPM-based three-dimensional electrical imaging approach. A: the MR images of the individual pig. B: the heart-torso model including the balloon catheter. C: the intracavitary mapping system. D: the butterfly plot of the intracavitary electrograms. E: the reconstructed activation sequence and the estimated initiation site by 3DCEI. F: the reconstructed electrograms by 3DCEI. G: the reconstructed cardiac activities by the intracavitary mapping system.

Based on the forward modeling described above, a heart-model-based estimation algorithm was optimized to derive the cardiac activation sequence from ICPMs [He et al 2007]. The parameters of the numerical heart model were initialized by using a preliminary classification system [Li and He 2001], and the corresponding ICPM was calculated by using FEM. The inverse method described in 6.2 was then applied in the data analysis.

The estimation of the 3D potentials/electrograms throughout the ventricles was based on the estimated 3D activation sequence with the above approach. A universal waveform of the action potential [Ohyu et al 2002] was assigned to every cellular unit in the ventricles, which starts with the very steep phase 0 and followed by the transient phase 1. Since only the activation of the heart was simulated and utilized in the present study, the diversity of phase 2 as well as phase 3 had little effect and so it was neglected in the present study. Once the estimated activation time τ at location k in the ventricles is obtained and the waveform of the trans-membrane action potential had been defined in the heart model, the equivalent current density at time instant t at the location k can be calculated as follows,

$$j^k(t) = -\sigma_i \nabla V^k(\tau, t) \tag{6.3}$$

where σ_i is the intracellular conductivity tensor, V the trans-membrane potential. Thus the equivalent current densities at thousands of uniformly distributed locations inside the myocardium were calculated representing the ventricular activities during activation. Based on the bidomain theory, the field potential Φ can be calculated from those current sources employing the Poisson's equation, shown in equation (5.1). This equation was then discretized and solved using the finite element method. When applying FEM, the intramural potentials were estimated using the method described in chapter 5.

Estimation of intramural potentials: simulation study

Computer simulations were conducted to evaluate the performance of the newly proposed three-dimensional imaging of the extracellular potentials throughout the ventricles. The volume conductor model and the heart excitation model of a pig were employed. In this simulation, pacing was performed in the ventricles and the simulated "true" 3D extracellular potentials in the activation cycle were forwardly calculated at 5,569 intramural sites using the finite element method. The ICPMs corresponding to the pacing were calculated and a 100 μV level Gaussian white noise (assuming the peak-peak value of the ICPMs was 10 mV) was added onto the ICPMs to simulate the noise contaminated measurements. The 3DCEI analysis as described above was then applied on the "measured" ICPMs, and the performance was evaluated by comparing the estimated potentials to the simulated potentials at thousands of intramural sites over the entire activation. The simulation was conducted in 24 pacing studies from different regions of the ventricles. The ventricular longitudinal section was divided into five regions: anterior, left wall, posterior, right wall and septum. Similar to the simulation studies in 6.3, the whole ventricle from base to apex was divided into three regions: basal, middle and apical. Thus the ventricles were segmented into 12 regions: basal-anterior (BA), basal-right-wall (BRW), basal-posterior (BP), basal-left-wall (BLW), basal-septum (BS), middle-anterior (MA), middle-posterior (MP), middle-left-wall (MLW), middle-septum (MS), apical-anterior (AA), apical-posterior(AP) and apical-septum (AS). Two pacing sites were chosen from each of the regions.

The effect of geometrical errors on the estimated 3D extracellular potentials was also evaluated under two conditions: 1) a random spatial noise with an averaged location

error of 1.2 mm was added onto the locations of the recording electrodes; 2) a 5 mm shift was assumed when measuring the location of the intracavitary multi-electrode array. Under each condition, studies were conducted at 24 pacing sites as well.

Evaluation of the imaging solutions in experiments

The performance of the 3DCEI approach was validated in terms of localization errors of the initiation sites of activation. The estimated activation sequences as well as electrograms (EGs) were analyzed and compared with those reconstructed by the endocardial NCM system over the endocardial surface.

The locations of the initiation sites of activation were estimated in the heart-excitation models which were obtained from the pre-operative MR images. The precise locations of LV pacing sites were recorded by the NCM system and were subsequently obtained in the heart-excitation model after the LV endocardial surface registration procedure described above. On the other hand, the precise locations of the RV pacing sites were obtained by locating the distal end of the pacing leads in the post-operative MR images of the isolated hearts (note that each heart was fixed in an end diastolic state). For the purpose of determining the precise 3D locations of the initiation sites in the resultant heart-excitation models, the surface registration procedure described in chapter 3 was performed between the isolated, fixed heart and the beating heart. After the registration, the precise locations of the initial activation sites in RV were determined in the heart-excitation model and could be directly compared with the estimated locations.

The mapped 3D ventricular activation sequences were evaluated by comparing with the results of the NCM system over the left ventricular endocardium. Though the reconstructed endocardial electrograms and activation sequence by the NCM system are not golden standards, those mapping results are still appreciable considering the broad clinical application. So the endocardial activation sequences were extracted from the 3DCEI solutions, and then projected from the endocardial surfaces of the heart models to the endocardial surfaces recorded by the NCM system for comparison. Similarly, the estimated electrograms were also evaluated by comparison to the output of the NCM system over the endocardial surface.

6.4.2. Results

Simulation: estimation of intramural potentials

The performance of intramural potential imaging was tested by pacing in 24 different sites throughout the ventricles. In order to quantitatively evaluate the performance of the proposed approach, the correlation coefficient (CC) was calculated. At each intramural site where potential was estimated, the potentials over all the time instants formed the electrogram. The CC between the estimated and the simulated electrograms during activation were calculated. Then the averaged value and the standard deviation of CC at all of the 5,569 intramural sites were calculated and summarized in Table 6.5. In summary, over the 24 pacing studies, the averaged CC was 0.94±0.03, which suggests that the proposed function of imaging intramural potentials in 3DCEI can reconstruct the potentials with reasonably high accuracy. Furthermore, when an averaged

location error of 1.2 mm was added to the locations of electrodes simulating geometrical errors in modeling, the averaged CC decreased to 0.93. When a 5 mm shift of the balloon catheter was assumed, the averaged CC was 0.90. The detailed results are shown in Table 6.5. Those results suggest the robustness of the proposed approach to the geometrical errors in modeling or measurements.

Table 6.5. The Averaged Correlation Coefficient (CC) of Electrograms

Heart region	BA	BRW	BP	BLW	BS	MA
CC*(Site 1)	0.96±0.05	0.98±0.04	0.97±0.05	0.98±0.02	0.86±0.14	0.97±0.03
CC#	0.95±0.05	0.95±0.05	0.94±0.04	0.95±0.04	0.86±0.11	0.95±0.05
CC+	0.88±0.12	0.90±0.12	0.89±0.13	0.92±0.09	0.85±0.14	0.93±0.06
CC*(Site 2)	0.93±0.10	0.96±0.05	0.88±0.16	0.97±0.05	0.95±0.06	0.91±0.08
CC#	0.95±0.04	0.95±0.07	0.90±0.07	0.94±0.06	0.93±0.05	0.91±0.05
CC+	0.89±0.11	0.89±0.13	0.84±0.16	0.90±0.10	0.92±0.08	0.90±0.11
Heart region	MP	MLW	MS	AA	AP	AS
CC*(Site 1)	0.98±0.03	0.93±0.09	0.97±0.04	0.91±0.11	0.98±0.03	0.93±0.09
CC#	0.95±0.04	0.93±0.08	0.96±0.06	0.87±0.12	0.95±0.05	0.91±0.09
CC+	0.92±0.07	0.89±0.12	0.92±0.10	0.92±0.09	0.93±0.08	0.89±0.12
CC*(Site 2)	0.92±0.09	0.92±0.10	0.96±0.05	0.95±0.07	0.95±0.09	0.91±0.12
CC#	0.94±0.06	0.91±0.10	0.95±0.05	0.91±0.09	0.92±0.06	0.89±0.11
CC+	0.90±0.10	0.90±0.10	0.94±0.08	0.94±0.07	0.89±0.12	0.88±0.14

*: 100 μV noise added; #: 100 μV noise and 1.2 mm location error added; +: 100 μV noise and 5 mm catheter shift added.
BA: basal-anterior; BRW: basal-right-wall; BP: basal-posterior; BLW: basal-left-wall; BS basal-septum; MA: middle-anterior; MP: middle-posterior; MLW: middle-left-wall; MS: middle-septum; AA: apical-anterior; AP: apical-posterior; AS: apical-septum.

Experimental evaluation: localization of the initiation site of activation

Pacing studies were conducted in 4 LV and 2 RV pacing sites with a total of 60 paced beats being analyzed (10 for each pacing site). The locations of the initiation sites and the localization error (LE) for each pacing site are summarized in Table 6.6. Over the 40 analyzed beats undergoing LV pacing, the averaged localization error was 5.6±1.6

mm. The averaged LE undergoing RV pacing was 9.4±1.6 mm due to farther distance from MEA to the pacing site.

Table 6.6. Localization Error

Pig #	*Pacing site*	*Localization error (mm)*										*Mean (mm)*
		1	2	3	4	5	6	7	8	9	10	
1	RVA	10.8	10.8	10.8	10.8	9.6	10.8	10.8	10.8	10.8	11.7	10.8±0.5
1	LVML	7.8	7.6	6.2	6.2	10.6	7.6	6.2	7.6	7.6	7.6	7.5±1.3
2	RVS	8.1	8.1	9.5	6.7	8.1	8.1	8.1	8.2	6.9	8.1	8.0±0.8
2	LVA	6.0	6.0	6.0	4.7	4.7	3.4	4.7	6.0	4.7	4.7	5.1±0.9
2	LVLL	4.5	7.5	4.2	4.2	5.4	3.4	5.4	4.2	4.2	4.2	4.7±1.1
2	LVAn	4.5	6.0	6.0	6.0	4.5	4.5	6.0	6.7	3.0	4.5	5.2±1.1

Experimental evaluation: estimation of the 3D activation sequence

The ICPM-based 3DCEI analysis was applied to those pacing data and the 3D activation sequences were functionally mapped. Figure 6.4 depicts an example of the mapped activation sequence when the heart was paced from the RV septum. In Figure 6.4, the activation wavefront initiated from the septum and propagated to LV and RV, respectively. The wavefront reached the LV endocardium (the breakthrough point is indicated with a green star) at the 9^{th} ms after initiation of activation and finally died out at the LV free wall. Another local maximum of activation time located at the RV free wall. It has been shown that both surface information and transmural information were included in our results and were straightforwardly illustrated. Physiologically reasonable activation sequences throughout the ventricles were obtained from all of the six pacing studies.

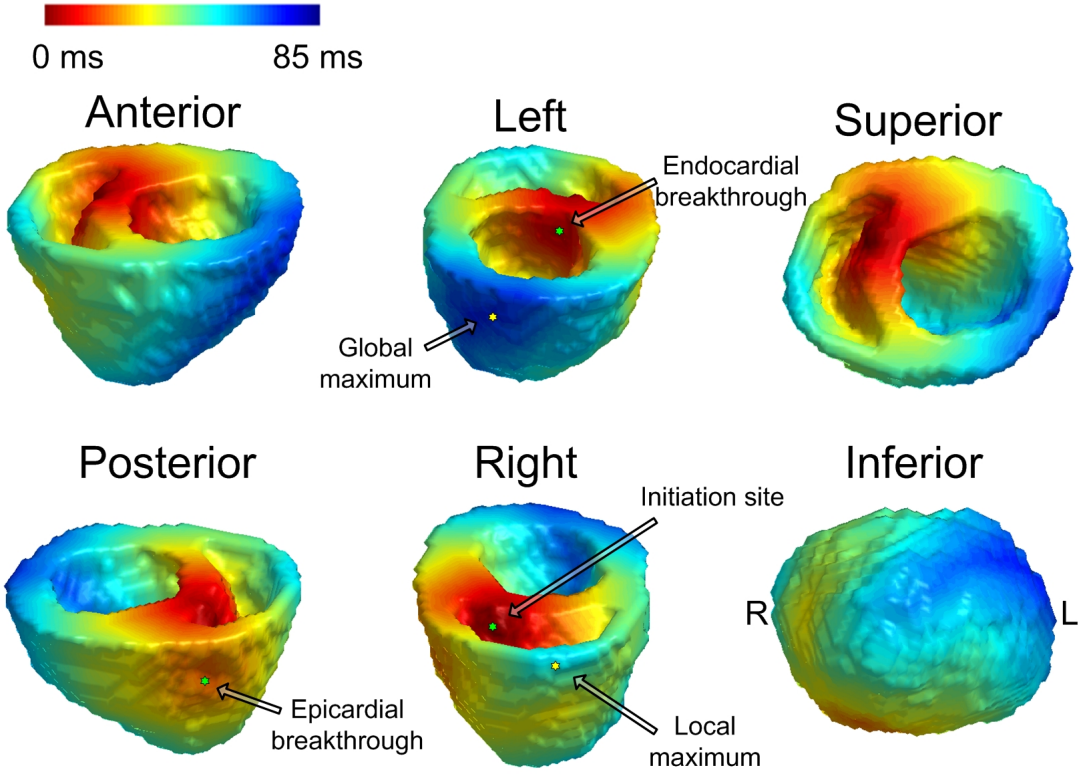

Figure 6.4. The imaged three-dimensional activation sequence when the heart was paced from the RV septum. The activation sequence is shown in six view angles. RED represents the earliest activated area and BLUE represents the latest activated area.

The endocardial activation sequences were then extracted from our 3D estimation results and compared with that of the NCM system. Since the NCM system's output regarding the endocardial activation sequence was a color-coded plot instead of quantitative data, qualitative comparison was made between the activation sequence estimated by 3DCEI and the NCM system's output. Figure 6.5(a) depicts the extraction of the endocardial activation sequence from our 3D results and the comparison between the two sets of endocardial activation sequences when pig #1 was paced from the RV apex. In the 3D results shown in the first column, the estimated initial area of activation is located at the RV apex. The activation wavefront propagated across the ventricles and

ended at the LV free wall. Regarding the extracted activation sequence on the LV endocardium, it was found that the mapping result by 3DCEI was consistent with the output of the NCM system for the general propagation pattern. The earliest endocardial activation site estimated by 3DCEI (indicated by number "1") was located at the apical-septal area, very close to the pacing site; the corresponding area illustrated by the NCM system was on the left side of LV apex, which might have an acceptable bias. On the other hand, the late activation areas indicated by 3DCEI and the NCM system were quite consistent.

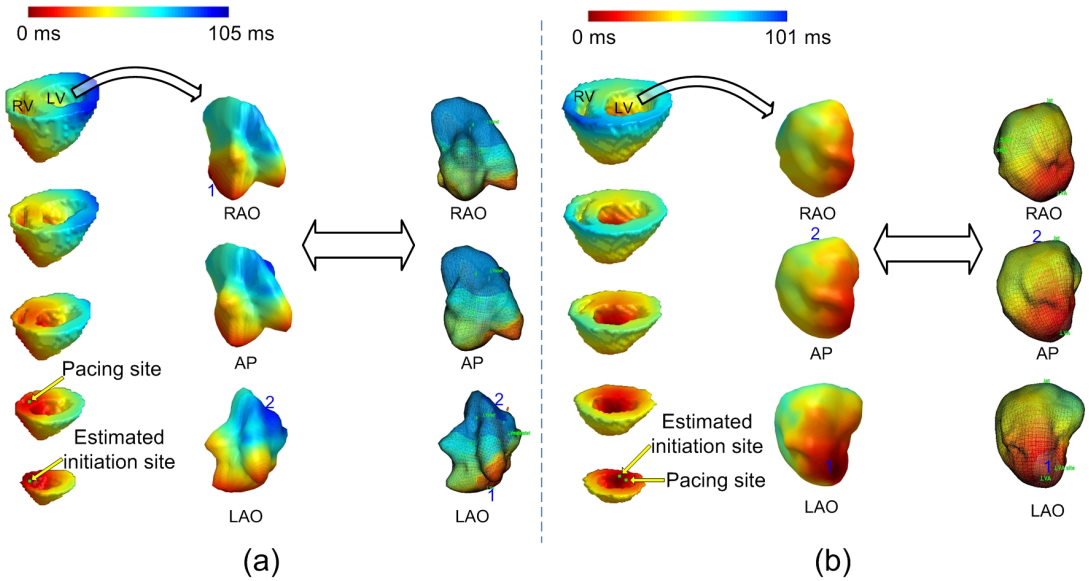

Figure 6.5. The evaluation of the estimated activation sequence when: (a) the pig #1 was paced from RV apex; (b) the pig #2 was paced from the LV apex. In each panel, the 3D activation sequence (AS) throughout the ventricles is shown in the left column. The precise location of the pacing site and the estimated location of the initiation site are indicated. The AS on the LV endocardial surface is extracted from the 3D solutions and shown in the middle column in 3 views: RAO, AP and LAO. The corresponding endocardial AS reconstructed by the intravitary noncontact mapping system is shown in the right column for comparison and validation. The earliest activated site is indicated by the number "1" and the latest activated site is indicated by "2" on the figure.

Figure 6.5(b) depicts another example when pig #2 was paced from the LV apex. It was observed that 3DCEI and the NCM system nicely supported each other regarding the depolarization propagation, illustrating reasonable consistency between these two sets of results.

Experimental evaluation: estimation of intramural electrograms

Figure 6.6 depicts an example of the reconstructed potentials/electrograms when the heart was paced from LV apex. Figure 6.6(a) shows the distribution of transmural potentials illustrating propagation of excitation throughout the 3D ventricles. Corresponding to the depolarization, the interstitial potential of a myocardial site decreased dramatically when the propagation wavefront arrived. The evolvement of the depolarization wavefront throughout the 3D myocardium can be clearly observed from the series of isopotential maps over time. The estimated series of 3D isopotential maps offered "virtual" electrograms should electrodes be placed intramurally. To evaluate the estimated EGs, ten different sites on the endocardial surface were selected and the reconstructed EGs by 3DCEI at those sites were compared with the EGs reconstructed by the NCM system as shown in Figure 6.6(c), where the consistency between the two sets of EGs was demonstrated by the averaged correlation coefficient of 0.73. Although the imaging results were consistent in general pattern, some discrepancies were observed. There was a timing shift in waveform 6, and the EGs reconstructed by 3DCEI showed slower recovery from the negative peak in waveform 7, 8, 9 and 10. The possible reason for this discrepancy will be discussed in the Discussion section below.

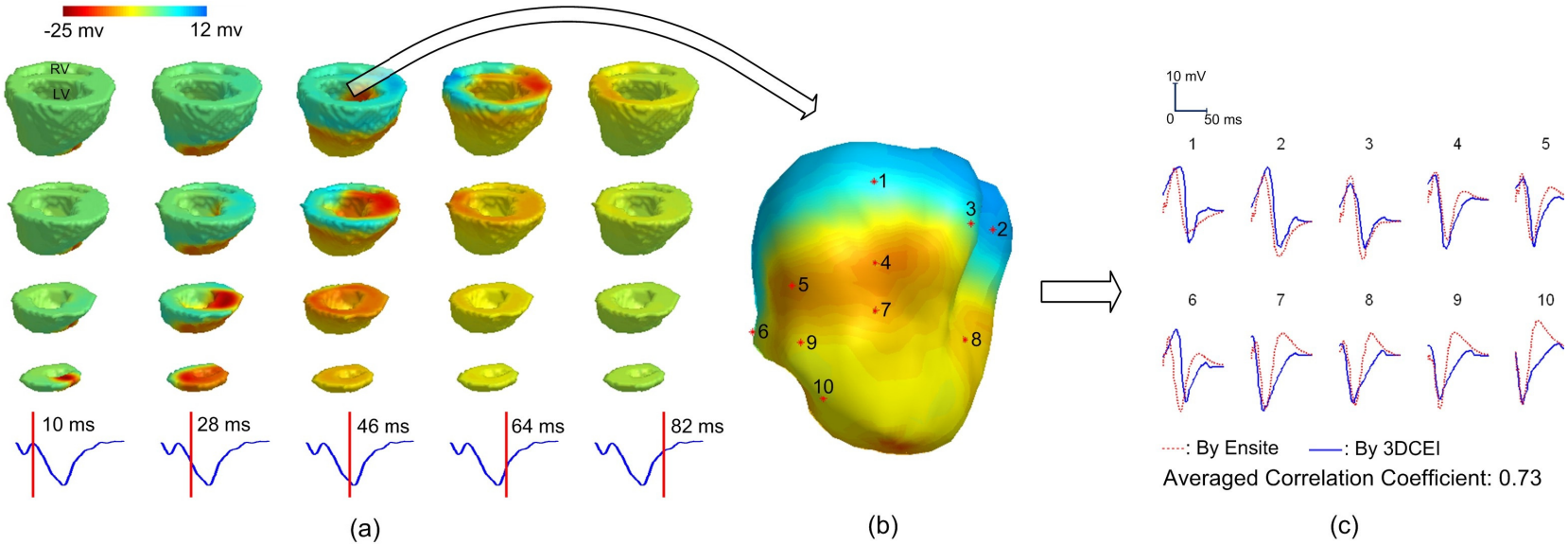

Figure. 6.6. The evaluation of the estimated electrograms when the heart is paced from the LV apex. (a) The 3D potential maps throughout the ventricles. The potential maps are shown on different horizontal levels from base to apex (each column), and in time sequence. The time instant after pacing corresponding to each column is indicated on the lead II ECG waveform. (b) The extracted endocardial potential map at the 46th ms after pacing and the locations of selected 10 sites on the endocardial surface. (c) The comparison of the reconstructed electrograms between the NCM system and the 3DCEI approach at 10 endocardial sites. The locations of the 10 sites are indicated in panel (b).

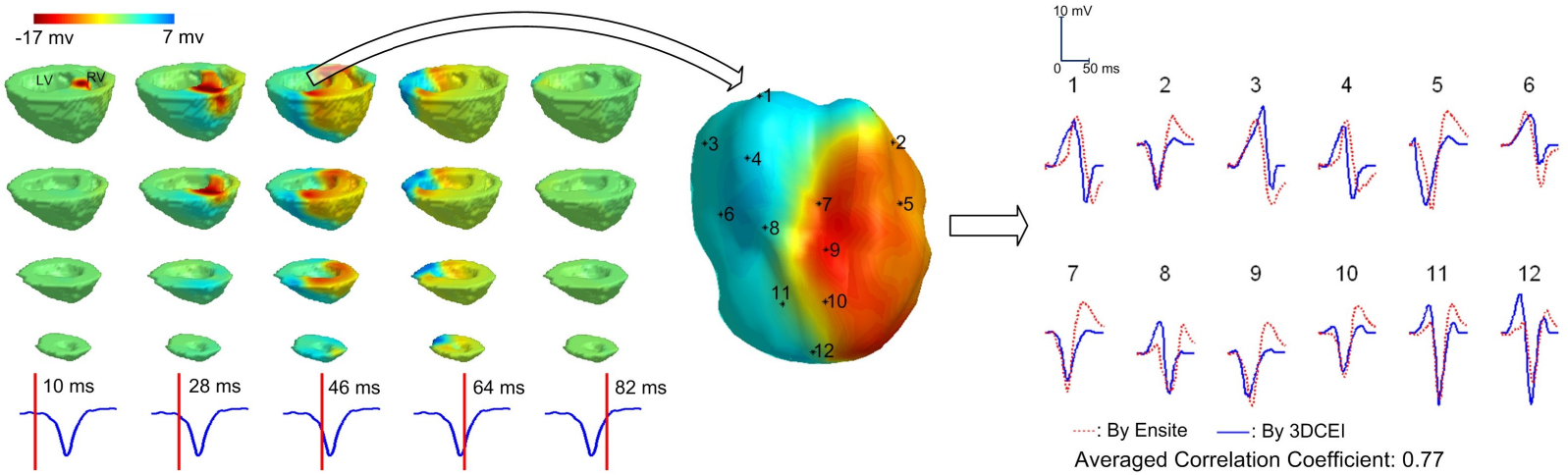

Figure. 6.7. The evaluation of the estimated electrograms when the heart is paced from the RV septum. (a) The 3D potential maps throughout the ventricles. The potential maps are shown on different horizontal levels from base to apex (each column), and in time sequence. The time instant after pacing corresponding to each column is indicated on the lead II ECG waveform. (b) The extracted endocardial potential map at the 46th ms after pacing and the locations of selected 12 sites on the endocardial surface. (c) The comparison of the reconstructed electrograms between the NCM system and the 3DCEI approach at 12 endocardial sites. The locations of the 12 sites are indicated in panel (b).

Figure 6.7 depicts another example of the reconstructed EGs when the heart was paced from RV septum. The averaged correlation coefficient between the waveforms of EGs at 12 typical sites shown in Figure 6.7(c) was 0.77.

6.4.3. Discussion

This pilot study, to our knowledge, provides the first experimental evidence with regard to the feasibility of tomographic imaging of the 3D cardiac electrical activities from intracavitary noncontact measurements. The feasibility of estimating the intramural potentials (proposed in chapter 5) is also evaluated, for the first time, in both simulation and animal experiments. Its ability of localization of the initiation site of activation has been rigorously validated. The estimated activation sequences and electrograms by 3DCEI were fairly consistent with the corresponding output of the NCM system on the LV endocardium. Though the mapping results by the NCM system are not necessarily a golden standard, they have been widely used in clinical EP labs, thus representing an important comparison study. The promising evaluation results suggest the potential of the novel 3DCEI technique to image 3D electrical activities from intracavitary recordings. Furthermore, the ICPM-based 3DCEI approach may take advantage of the short distance between the intracavitary recordings and the cardiac sources to reveal subtle cardiac events imperceptible from the body surface, and such studies are expected in the future

Localization of the initiation site of excitation and/or arrhythmogenic substrate is of importance for guiding catheter ablation. Efforts have been made to find the initiation sites of cardiac events on the heart surfaces by employing an inverse calculation [Gornick

et al 1999; Tilg et al 2002; Ramanathan et al 2004]. Compared to those surface imaging approaches, the 3DCEI approach has the potential of providing comprehensive 3D information of functional anatomy, which is of importance for characterizing and localizing arrhythmias of sub-endocardial or intramural origins. In the present study, the successful localization of the initiation site induced by pacing suggests the potential of localizing the initiation sites of focal ventricular tachycardia and/or other cardiac arrhythmias throughout the 3D myocardium.

An interesting phenomenon is that 3DCEI performed better when localizing the pacing sites in LV than in RV; that is, smaller localization error was observed when the pacing site was in LV. Corresponding to the pacing sites at LV lateral and LV apex in pig #2, the averaged LE were 4.7±1.1 mm and 5.1±0.9 mm, respectively. On the other hand, the averaged LE corresponding to the pacing site at RV apex in pig #1 was 10.8±0.5 mm. Due to the limited number of pacing sites in this pilot study, rigorous statistical analysis has not been performed. The difference in localization errors between LV and RV shall be attributed to the fact that the balloon catheter was placed in the LV, and the assumption can be made that the smaller distance between the MEA and the pacing site in LV resulted in smaller localization error. A recent study also supported this notion that in the NCM system, if the imaged source is farther from the balloon catheter, the accuracy of the mapping results will decrease [Abrams et al 2007]. Such results are consistent with our understanding that signals generated by closer sources are better reflected in the recordings and therefore the sources could be more accurately reconstructed in an inverse approach. In future practical applications, the MEA should be

put in the appropriate chamber to keep it relatively close to the region of interest. Nevertheless, even when the origin of activation is relatively far from the MEA, 3DCEI can still reconstruct reasonably good mapping results (see Figure 6.5 (a) and Figure 6.7).

Mapping the cardiac activation sequence is useful for revealing the underlying mechanism of arrhythmias and facilitating the subsequent treatment. Specifically, 3D activation sequence mapping provides a straightforward method to characterize the cardiac events originating from the subsurface substrates. The imaged 3D activation sequence by 3DCEI can provide detailed 3D information (see Figure 6.4 and Figure 6.5), which is especially useful for areas with thick myocardium, such as apical area and LV free wall. Considering that not all arrhythmogenic substrates are accessible from endocardium, the necessity of applying epicardial ablation needs to be determined in some cases. Accounting for its ability of providing global activation sequence, the 3DCEI approach may play an important role in detecting non-subendocardial arrhythmogenic substrates and selecting appropriate treatment options.

Direct intra-operative mapping can provide an important insight into the intrinsic characteristics of cardiac events [Chung et al 1997; Zhang et al 2000; Attin et al 2008]. The unique information provided by intramural EGs can increase our understanding of the mechanisms of arrhythmic events and aiding clinical management of arrhythmias. In the present study, we reported the first effort of estimating the EG at any intramural site throughout the ventricles. Such estimated intramural EGs can be considered as an approximation of extracellular potentials, which would be recorded should one put a

large number of electrodes within the ventricular volume. The simulation study suggests that the extracellular potential at any intramural site throughout the ventricles can be estimated with high accuracy. As results, the 3D isopotential maps shown in Figure 6.6 and Figure 6.7 reveal the ability of 3D potential mapping in providing spatio-temporal information regarding cardiac electrical activity, depicting that our technique can present 3D potentials in great detail. Most of the noninvasive or minimally-invasive mapping methods limit the results on the heart surface (endocardium, or epicardium, or both); the intra-operative mapping with needle electrodes can provide real 3D mapping results, but the procedure is inconvenient and the cardiac tissue has to be destroyed at some level. Compared to those mapping methods, the 3DCEI approach only needs minimally-invasive intracavitary recordings but can present 3D results transmurally like the intra-operative mapping.

It is known that the shape and duration of the trans-membrane action potential differ at different locations or at different heart rates. In the present study, a universal waveform of the action potential has been assigned to every cellular unit in the heart model. Though the simplified distribution of action potential was employed, the heart model is deemed to be appropriate in the present study, because we are focusing on ventricular depolarization following pacing. In this scenario, the phase 0, phase 1 and possibly the early part of phase 2 of the action potential were involved, because the activation of the entire ventricles lasts no longer than 110 ms. The duration of phase 2 and the shape of phase 3 would have little to do with the activation. Since most of the ventricular cells have very similar action potential during phase 0 and phase 1, we employed a universal action

potential to represent all the cells as our interest is on the activation. On the other hand, the heterogeneity of the action potentials plays an important role during repolarization or under some complicated arrhythmias, and it should be incorporated into our approach when investigating complicated arrhythmias in future investigation.

The fiber structure and related anisotropic conductivity of the myocardium have effects on the spread of excitation and the morphology of intramural electrograms [Taccardi et al 1994]. In the present study, the anisotropic nature of the heart was not considered and the heart model used in 3DCEI approach was assumed to be isotropic. In a previous study, it was reported that neglecting anisotropy does not automatically result in a poor quality of the solutions of the inverse problem [Modre et al 2006]. Our own experience from computer simulation also suggests that ignoring the anisotropy does not seem to affect significantly the inverse solutions of the 3D activation sequence imaging and extracellular potential imaging. However, incorporating anisotropy should benefit the accuracy of the inverse solutions and the reported localization error and estimation error may be further reduced if conductivity anisotropy is incorporated in the forward model. In this pilot study, we have reported the concepts and principles of the 3D intramural extracellular potential imaging, and the first experimental results of 3D intramural extracellular potential imaging and of the ICPM-based 3DCEI. In future investigations, conductivity anisotropy could be incorporated from information obtained by using diffusion tensor magnetic resonance imaging (DT-MRI) [Helm et al 2005]. DT-MRI can detect the fiber orientation in the 3D space based on the phenomenon that water diffuses more rapidly in the direction aligned with the fibrous structure. The fiber orientation at

any position of the heart could be obtained via a full magnetic resonance scan and so could be incorporated into the 3DCEI approach.

The number of animals (n=2) employed in the present pilot study is small. A larger population is needed in order to draw a statistically significant conclusion. Many experimental parameters have been involved in the present study, such as pacing location, pacing rate, pacing vector, pacing strength, balloon catheter's location, ventricular load, etc. The detailed effects of some of the experimental parameters on the performance of the 3DCEI approach shall need further investigations. For example, is there any effect when the pacing rate is changed? Furthermore, in the present study, the recording balloon catheter was put in the left ventricle. It would be interesting to know the performance of 3DCEI when the catheter is in the right ventricle. Nevertheless, the present pilot study for the first time reports the experimental validation of the ICPM-based 3DCEI, and the promising experimental results on intramural activation sequence and electrograms throughout the ventricular volume. The experimental results of six pacing sites and of 60 beats represent important data suggesting the feasibility of this novel technique in extending our ability to mapping cardiac electrical activity from endocardial to intramural domain. While beyond the scope of the present study, extensive evaluation on the performance of the proposed 3DCEI approach and the detailed effects of experimental parameters would be conducted in future studies with a larger number of employed animals.

We have experimentally demonstrated the feasibility of localizing initiation sites of activation, mapping the global activation sequences and estimating electrograms throughout the ventricles in a large mammalian model from noncontact intracavitary recordings using the 3-dimensional cardiac electrical imaging technique. The newly proposed 3D imaging of intramural extracellular potentials has been rigorously evaluated in simulation and promising results have been obtained; using a well-controlled pacing procotol, the 3DCEI results have been evaluated in comparison with results obtained from the clinical NCM system over the endocardial surface. The present simulation and experimental results suggest that the intracavitary-based 3DCEI approach can reconstruct important electrophysiological properties of cardiac activation during pacing, and may enhance our ability to map and manage focal ventricular arrhythmias.

7. Non-invasive estimation of global activation sequence using extended Kalman filter

7.1. Objective

One major difficulty of solving the inverse problem is its ill-posed nature, which is due to the smoothing and attenuation effects when the ECG signals travel through the torso volume conductor. As results, a slight measurement noise on the body surface potentials may induce large perturbation on the inverse solution. The ill-posedness in the 3D inverse problem is even more challenging. In our group, two inverse schemes have been proposed to solve the 3D cardiac sources and to tackle the ill-posedness. One way of circumventing this difficulty is employing an excitable heart model incorporating *a priori* physiological knowledge [He et al 2002]. The inverse scheme is iteratively optimizing the parameters of the heart model to obtain the expected physiological/pathological characteristics corresponding to the measured BSPMs. Alternatively, in our physical-model-based approach, regularization methods were employed to deal with the ill-posedness; the spatial-temporal equivalent current densities were inversely derived from BSPMs and then the spatial activation sequence were picked up from them. In the present study, we have further investigated the methodology of the 3D inverse problem. We try to build up the nonlinear relationship from the 3D activation sequence to the BSPMs and solve the nonlinear inverse problem using the extended Kalman filter.

The Kalman filter (KF) is a set of mathematical equations which estimate the state of a process in a recursive way by minimizing the estimated error covariance. It can incorporate all available information and provide an optimal estimation, even when the

precise nature of the modeled system is unknown. Regarding cardiac inverse problem, the Kalman filter has been applied to estimate the epicardial potentials from the recorded BSPMs [Joly et al 1993; El-Jakl et al 1995] and to estimate the endocardial potentials from the recorded intracavitary potentials by a noncontact multi-electrode array [Berrier et al 2004]. In their work, a linear relationship between the estimated sources and the recordings exists if the volume conductor is assumed quasi static.

The aim of the present study is to estimate the 3D activation sequence from the noninvasive BSPMs by using the Kalman filter. Noting that the transfer function from the 3D activation sequence to the BSPMs is nonlinear, the extended Kalman Filter (EKF) is to be employed in the algorithm to handle the non-linearity. The original contributions of the present study include: 1) defining the nonlinear relationship between the 3D activation sequence and the BSPMs and numerically modeling it; 2) Applying the EKF on this nonlinear inverse problem; 3) using a novel and cost-efficient regularization method in the EKF to handle the ill-posedness of the inverse problem. Simulation studies with a realistic human model are to be performed to evaluate the performance of the proposed inverse approach. The advantages of the proposed algorithm are to be discussed.

7.2. Methods

7.2.1. From three-dimensional activation sequence to body surface potentials

The relationship between the 3D activation sequence and the body surface potentials was defined in the forward problem. First, based on the bidomain theory [Miller and

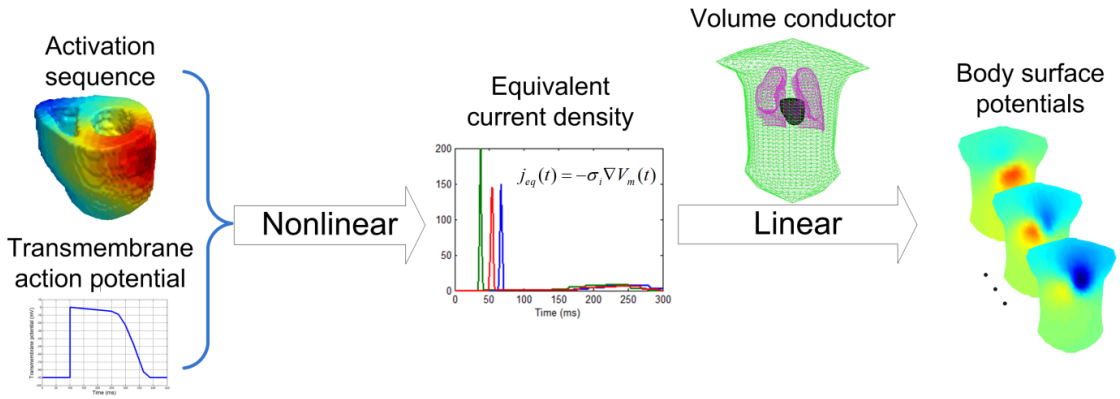

Figure 7.1. The nonlinear modeling from the 3D activation sequence to the body surface potentials.

Geselowitz 1978], the equations governing the quasi-static volume conductor were as follows,

$$\nabla \cdot [(\sigma_i + \sigma_e)\nabla \phi] = \nabla \cdot j_{eq} \qquad \text{in } \Omega;\ \sigma(\nabla \phi) \cdot n = 0 \text{ on } S \tag{7.1}$$

$$j_{eq}(t) = -\sigma_i \nabla V_m(t) \quad \text{in } \Omega \tag{7.2}$$

where σ_i and σ_e are the intracellular and interstitial conductivity tensor, Φ the field potential, $j_{eq}(t)$ the equivalent current density at time instant t, $V_m(t)$ the transmembrane potential at time instant t, and n the outward unit normal to the body surface S. By applying the finite element method [Zhang et al 2004], equation (7.1) was numerically solved and the linear relationship between the equivalent current density and the body surface potentials was built as

$$\phi_B(t) = AJ_{eq}(t) \tag{7.3}$$

where $\Phi_B(t)$ is an N x 1 vector containing the body surface potentials at time instant t, N is the number of recording electrodes on the body surface. $J_{eq}(t)$ is a $3M$ x 1 vector

containing equivalent current densities at M grid points in the myocardium at time instant t. Each of the equivalent current densities is represented by an orthogonal triple of dipoles. A is an N x $3M$ transfer matrix relating the equivalent current densities to the body surface potentials.

Second, based on the physiological knowledge about the cardiac transmembrane action potential, at location r in the myocardium, a nonlinear relationship between the activation time and the transmembrane potential could be defined as

$$V_m^r(t) = G(t - \tau^r) \tag{7.4}$$

where G represented the waveform of the transmembrane action potential at r. In the present study, A universal waveform of the action potential was assigned to every cellular unit in the ventricles, which starts with the very steep phase 0 and followed by a plateau, as shown in Figure 7.1. Since only the activation period of the heart was simulated and utilized in the present study, the diversity of phase 2 as well as phase 3 had little effect and so it was neglected in the present study. Substituting equation (7.4) into equation (7.2), and then substituting equation (7.2) into equation (7.3), we got

$$\phi_B = h(\tau) \tag{7.5}$$

where Φ_B is an N x N_t matrix containing the body surface potentials recorded by N electrodes at N_t time instants covering the entire activation of the heart, τ is the vector of activation times at M points in the 3D myocardium, and h is the nonlinear operator relating the activation sequence to the body surface potentials.

7.2.2. The state space model and the extended Kalman filter

In order to apply the Kalman filter to solve equation (7.5), a state-space model was established and governed by the following equations:

$$\tau_k = f(\tau_{k-1}) + w_{k-1} \tag{7.6}$$

$$\phi_{B,k} = h(\tau_k) + v_k \tag{7.7}$$

where τ_k is the state vector at step k and here it is the vector containing the activation sequence of the 3D heart, f is a processor that predict the current state from the previous state, $\Phi_{B,k}$ is the measured body surface potentials corresponding to the k^{th} state, h is the nonlinear operator defined in (7.5), and w, v are process noise and measurement noise, respectively, which are both assumed as independent Gaussian white noise with the following normal distribution:

$$P(w) \sim N(0, Q); P(v) \sim N(0, R) \tag{7.8}$$

It is noteworthy that in this approach, each step did not correspond to a time instant; instead, each step corresponded to an entire beat during activation. The input of each step was the measured body surface potentials over the activation of the heart. In practice, the body surface potentials during a series of beats recorded under the same condition were used as input. Then the inverse solution under this physiological condition was estimated with all those beats, one beat for each step. In other researchers' work regarding cardiac inverse problem, f can be defined linear, such as scalar multiple of the identity [Joly et al 1993; Berrier et al 2004]. The f can also be determined by using a regularized least-

square approach [Joly et al 1993] or using a maximum likelihood approach [El-Jakl et al 1995]. In the present approach, a nonlinear predicting procedure was utilized to regularize the inverse solutions, and the nonlinear f was determined by the following rule:

$$\tau_{j,k} = \begin{cases} \tau_{j,k-1}, when \left\| \tau_{j,k-1} - \frac{1}{n}\sum_{i=1}^{n} \tau_{i,k-1} \right\| \le \varepsilon \\ \frac{1}{n}\sum_{i=1}^{n} \tau_{i,k-1}, when \left\| \tau_{j,k-1} - \frac{1}{n}\sum_{i=1}^{n} \tau_{i,k-1} \right\| > \varepsilon \end{cases} \tag{7.9}$$

where τ_i is the activation time at the myocardial location whose distance to the location of τ_j is smaller than a certain threshold, and ε is a pre-defined threshold determining the method of updating τ_j.

The Kalman filter is a linear recursive estimator, while both f and h were nonlinear in the present study. Thus the extended Kalman filter (EKF) was employed to handle the non-linearity by liberalizing the estimation around the current estimate using the partial derivatives of the process function and measurement function. Equation (7.6) and (7.7) were rewritten as

$$\tau_k \approx \tilde{\tau}_k + F(\tau_{k-1} - \hat{\tau}_{k-1}) + W w_{k-1}$$

$$\tilde{\tau}_k = f(\hat{\tau}_{k-1}) \tag{7.10}$$

$$\phi_{B,k} \approx \tilde{\phi}_{B,k} + H(\tau_k - \tilde{\tau}_k) + V v_k$$

$$\tilde{\phi}_{B,k} = h(\tilde{\tau}_k) \tag{7.11}$$

where τ_k and $\Phi_{B,k}$ are the actual state vectors and measurement vectors, $\hat{\tau}_k$ is an *a posteriori* estimate of the state at step k, F is the Jacobian matrix of partial derivatives of f with respect to τ, H is the Jacobian matrix of partial derivatives of h with respect to τ, W is the Jacobian matrix of partial derivatives of equation (7.6) with respect to w, V is the Jacobian matrix of partial derivatives of equation (7.7) with respect to v.

The EKF then used (7.10) and (7.11) to recursively update the state vector in an attempt of minimizing the error covariance matrix. The error covariance matrix was defined as

$$P = E[(\tau - \hat{\tau})(\tau - \hat{\tau})^T] \tag{7.12}$$

where τ is the true activation sequence, and $\hat{\tau}$ is the estimated result. The EKF approach included "predict" and "correct". In "predict" procedure, the *a priori* estimate of the state vector and the error covariance matrix were projected from the estimate in last step:

$$\hat{\tau}_k^- = f(\hat{\tau}_{k-1}) \tag{7.13}$$

$$P_k^- = F_k P_{k-1} F_k^T + W_k Q_{k-1} W_k^T \tag{7.14}$$

In "Correct" procedure, the Kalman gain K was calculated, and then the *a posteriori* estimate of the state vector and error covariance matrix were updated with the measured body surface potentials and the Kalman gain:

$$K_k = P_k^- H_k^T (H_k P_k^- H_k^T + V_k R_k V_k^T)^{-1} \tag{7.15}$$

$$\hat{\tau}_k = \hat{\tau}_k^- + K_k(\phi_{B,k} - h(\hat{\tau}_k^-)) \tag{7.16}$$

$$P_k = (I - K_k H_k) P_k^- \tag{7.17}$$

For the above iterative procedure, the initial value of the error covariance matrix was set as $P_0 = I$. During the iteration, the estimated error covariance matrix would be updated and eventually converge. The initial value of the state vector could be obtained by using one of the following methods: 1) to get the initial guess on the activation sequence from the simulation using an excitable physiological heart model [Li and He 2001]; 2) to pick up the initial guess of the activation sequence using the inversely reconstructed current density [Liu et al 2006b]. In the present study, the second scheme was used.

7.2.3. Computer simulation

A realistic human heart-torso model built from the computed tomography (CT) images was employed in the present study [He et al 2007]. The torso, lungs and blood mass were assumed to be isotropic conductors. A generalized cardiac anisotropy was incorporated into the heart model as described in detail in [He et al 2002]. The "true" activation sequence was generated by a cellular-automaton heart model [Li and He 2001] and then the equivalent current densities were subsequently obtained using equation (7.4) and (7.2). An 128-electrode array were employed to represent the body surface potential map. The forward calculation from the equivalent current density to the body surface potentials were performed using the finite element method [He et al 2007].

In this simulation, pacing was performed in the ventricles and the simulated "true" 3D activation sequence in the activation cycle and the corresponding body surface potential maps (BSPMs) were calculated using the above method. A Gaussian white noise was added onto the BSPMs to simulate the noise contaminated measurements. The proposed inverse approach was then applied on the "measured" BSPMs, and the performance was evaluated by comparing the estimated activation sequences to the simulated activation sequences throughout the entire myocardial volume. The single-site-pacing study was conducted at 24 pacing sites from different regions of the ventricles. The ventricular longitudinal section was divided into five regions: anterior, left wall, posterior, right wall and septum. The whole ventricle from base to apex was divided into three regions: basal, middle and apical. Thus the ventricles were segmented into 12 regions: basal-anterior (BA), basal-right-wall (BRW), basal-posterior (BP), basal-left-wall (BLW), basal-septum (BS), middle-anterior (MA), middle-posterior (MP), middle-left-wall (MLW), middle-septum (MS), apical-anterior (AA), apical-posterior(AP) and apical-septum (AS). Two pacing sites were chosen from each of the regions.

Dual-site-pacing study was also employed to simulate the condition that the cardiac excitation originate from two centers in an ectopic beat. In each study, a pair of pacing sites were chosen from different regions and then pacing was conducted from both of the sites. The other settings were the same with the single-site-pacing study. In total, 6 pairs of pacing sites were chosen from the following regions: BA-MP, BRW-MLW, BP-MS, BLW-AA, BS-AP and MA-AS.

In order to evaluate the performance of the proposed approach, the correlation coefficient (CC) and relative error (RE) were calculated between the estimated and the "true" activation sequence. The CC was defined as

$$CC = \frac{\sum_{i=1}^{N}(\hat{\tau}_i - \bar{\hat{\tau}})(\tau_i - \bar{\tau})}{\sqrt{\sum_{i=1}^{N}(\hat{\tau}_i - \bar{\hat{\tau}})^2} \bullet \sqrt{\sum_{i=1}^{N}(\tau_i - \bar{\tau})^2}} \tag{7.18}$$

where $\hat{\tau}_i$ is the estimated activation time at the i^{th} myocardial location, $\bar{\hat{\tau}}$ is the averaged activation time over the N myocardial locations throughout the 3D heart, τ_i is the true activation time at the i^{th} myocardial location and $\bar{\tau}$ is the averaged true activation time. The RE was defined as

$$RE = \sqrt{\sum_{i=1}^{N}(\hat{\tau}_i - \tau_i)^2} \Big/ \sqrt{\sum_{i=1}^{N}(\tau_i)^2} \tag{7.19}$$

The CC can evaluate the similarity regarding the global pattern between the estimated and the true 3D activation sequence, while the RE quantify the dissimilarity in the estimated results.

Since single-pacing and dual-pacing protocols were used, the EKF's performance on localizing the origin(s) of the activation was evaluated by picking up the earliest activated site(s) according to the inversely estimated activation sequence. The localization error (LE) was reported.

7.3. Results

Both single-site-pacing and dual-site-pacing studies were conducted. In each of the studies, the iteration of the EKF always converged. Figure 7.2 shows the change of CC and RE between the estimated and the true 3D activation sequence during iteration when

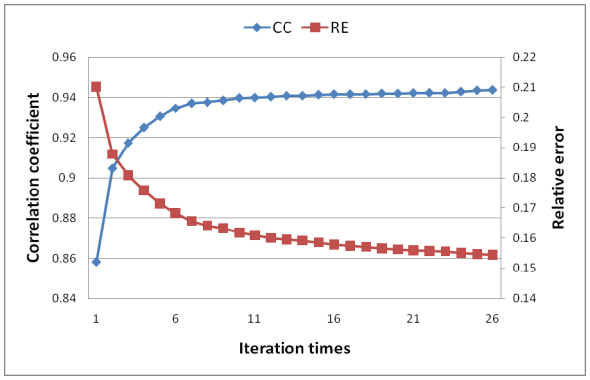

Figure 7.2. The change of the correlation efficient and the relative error between the estimated and the true activation sequence during iteration. The heart is paced in the basal-left-wall region.

the heart is paced at the BLW region. The increase of CC and decrease of RE indicate that the estimated activation sequence is optimized during iteration. Both CC and RE eventually converge because the error covariance matrix has converged and become stable after enough iteration steps.

The single-site pacing studies were first conducted at 24 sites throughout the ventricles when the measured BSPMs were contaminated with a 20 μV level Gaussian white noise (assuming the peak-peak value of the BSPMs was 3 mV) . Figure 7.3 (a) depicts an example of inversely estimated 3D activation sequence when the heart is paced at the MLW region. When using the activation sequence obtained by weighted minimal norm method (the second row) and the picking-up principle proposed in [Liu et al 2006b] as the initial value of the EKF iteration, the final output of EKF (the 3D activation

sequence shown in the third row) has shown significant improvement with higher consistency with the "true" activation sequence. The evaluation results of the 24 single-pacing studies are shown in Table 7.1. In summary, the averaged correlation coefficient (CC) between the estimated 3D activation sequence by EKF and the true results over the 24 pacing studies was 0.95±0.03, and the averaged relative error was 0.13±0.04. The earliest activated site was localized and compared to the true pacing site. Over the 24 pacing sites, the averaged localization error was 3.0±0.8 mm.

Table 7.1. Evaluation of inverse solutions during single-site pacing (20 μV noise)

Pacing region	BA	BRW	BP	BLW	BS	MA
(1) CC/RE	0.972/0.090	0.982/0.075	0.978/0.096	0.958/0.134	0.974/0.092	0.962/0.122
LE (mm)	1.87	1.54	3.12	2.79	3.87	2.38
(2) CC/RE	0.983/0.081	0.982/0.079	0.957/0.130	0.944/0.155	0.909/0.178	0.959/0.133
LE (mm)	3.48	3.85	3.82	3.60	1.62	3.75
Pacing region	MP	MLW	MS	AA	AP	AS
(1) CC/RE	0.980/0.096	0.910/0.198	0.936/0.147	0.945/0.154	0.908/0.194	0.941/0.142
LE (mm)	2.19	4.09	2.47	2.81	3.55	3.33
(2) CC/RE	0.975/0.116	0.982/0.083	0.891/0.218	0.965/0.147	0.973/0.120	0.898/0.196
LE (mm)	3.25	3.40	2.59	2.61	3.77	2.57

CC: correlation coefficient; RE: relative error; LE: localization error.
BA: basal-anterior; BRW: basal-right-wall; BP: basal-posterior; BLW: basal-left-wall; BS basal-septum; MA: middle-anterior; MP: middle-posterior; MLW: middle-left-wall; MS: middle-septum; AA: apical-anterior; AP: apical-posterior; AS: apical-septum.

Table 7.2. Evaluation of inverse solutions during single-site pacing (60 μV noise)

Pacing region	BA	BRW	BP	BLW	BS	MA
(1) CC/RE	0.968/0.094	0.978/0.080	0.976/0.102	0.957/0.141	0.973/0.093	0.956/0.134
LE (mm)	1.87	1.54	3.12	2.79	3.87	2.38
(2) CC/RE	0.982/0.082	0.981/0.081	0.953/0.139	0.939/0.165	0.899/0.190	0.956/0.138
LE (mm)	3.48	3.85	3.82	3.60	1.62	3.75
Pacing region	MP	MLW	MS	AA	AP	AS
(1) CC/RE	0.981/0.095	0.903/0.214	0.933/0.151	0.942/0.158	0.901/0.202	0.929/0.157
LE (mm)	2.19	4.09	2.47	2.81	3.55	3.33
(2) CC/RE	0.974/0.117	0.981/0.090	0.888/0.230	0.961/0.151	0.963/0.128	0.896/0.198
LE (mm)	3.25	3.40	2.59	2.61	3.77	2.57

In order to test the robustness of the algorithm regarding noise, a 60 μV level noise was also employed in the single-site-pacing studies. The other settings were the same. The results over the 24 pacing sites are summarized in Table 7.2. Though the noise level is 200% higher, the averaged CC slightly decreased by only 0.005 and RE increased by 0.006. The very similar results with that in Table 7.1 shows that the increased noise level has little effect on the inverse results.

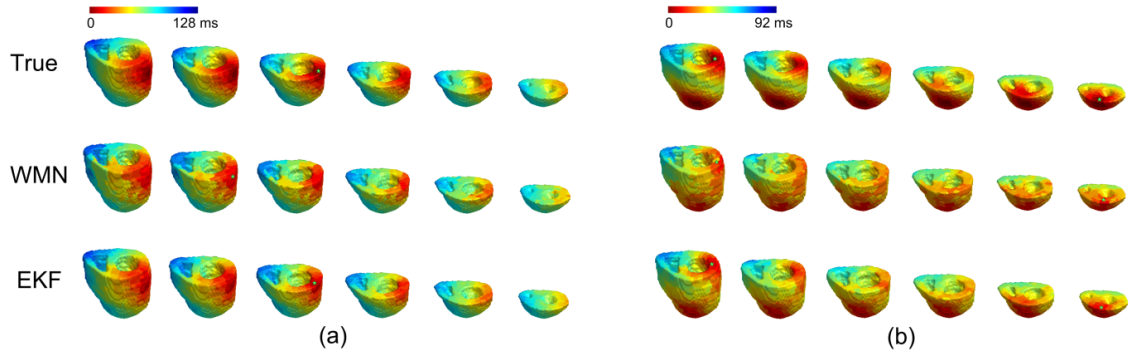

Figure 7.3. The inverse results in simulation when (a) single-site-pacing at middle-left-wall; (b) dual-site-pacing at basal-left-wall and anterior-apex. In each panel, the first row is the true 3D activation sequence shown by 6 horizontal sections, arranged from base to apex; the precise pacing site(s) is indicated with green star(s). The second row is the estimated 3D activation sequence picked up from the reconstructed current densities; the current densities are inversely calculated with the weighted minimal norm (WMN) method; the estimated origin(s) of activation is indicated by green star(s). The third row is the estimated 3D activation sequence with the extended Kalman filter (EKF); the estimated origin(s) of activation is indicated by green star(s).

In the dual-site pacing studies, the 20 μV level noise was added onto the simulated BSPMs. One example of dual-pacing studies is shown in Figure 7.3 (b), where the heart is paced from BLW and AA simultaneously. Compared to the initial value in the second row, the result obtained with EKF better localizes both of the earliest activated sites in the complex dual-pacing condition. The pacing site in BLW region is near the endocardium, while the other one in AA region is near the epicardium. In the second row of the figure,

it is hard to tell the depth of the earliest activated sites, but the result by EKF in the third row clearly indicate the depth of the localized sites, which proves the proposed algorithm's ability of revealing 3D information beyond the heart surface. The results of dual-site pacing studies are shown in Table 7.3. In summary, the averaged CC of the 6 studies was 0.93±0.02, and the averaged RE was 0.16±0.02. Both of the origins of activation in each study were localized, and the averaged localization error over 12 sites in 6 studies was 4.3±1.6 mm.

Table 7.3. Evaluation of inverse solutions during dual-site pacing

Pacing region	BA-MP	BRW-MLW	BP-MS	BLW-AA	BS-AP	MA-AS
CC	0.942	0.912	0.920	0.935	0.910	0.965
RE	0.158	0.161	0.180	0.141	0.192	0.129
LE (mm)	3.48/4.33	3.28/5.08	1.79/6.33	3.24/4.40	6.60/2.57	4.51/6.37

7.4. Discussion

In the present study, a novel method of inversely estimating the three-dimensional activation sequence has been proposed and evaluated in simulation studies. We have reported: 1) building up the nonlinear relationship between the three-dimensional transmural activation sequence and the body surface potentials; 2) employing the extended Kalman filter to solve the 3D activation sequence from the BSPMs; 3) applying a new nonlinear regularization scheme in the predicting procedure of EKF. Promising results have been reported.

Previously, the physiological heart-model-based method [He et al 2002] and the physical-model-based method [Liu et al 2006b] have been reported to estimate the 3D activation sequence. In the present new approach, the EKF has brought some interesting

features. First, the simulation shows that the EKF-based approach is robust to the measurement noise. When the noise level increased from 20 μV to 60 μV, the accuracy of the inverse solutions did not significantly become worse. That is because the information regarding noise level has been incorporated into the EKF calculation by setting up the noise covariance matrix. The advantage of EKF is, even if our estimate on the noise is not very accurate, the iteration can still find the optimal solutions, while the iteration speed may be affected. That means, when the measurements is severely contaminated by noise, the EKF-based inverse approach may still have good performance, especially when the noise is "white", as what we have assumed in the EKF.

Second, the EKF-based approach can incorporates all information that can be provided to it. The Kalman filter is theoretically an optimal data processing algorithm. It processes all available measurements to estimate the state of the system [Maybeck 1979]. Specifically, when estimating the activation sequence, the BSPMs covering the entire activation period of the ventricles have been used as input in the present approach. Thus the temporal information in the body surface measurements has been naturally incorporated into the EKF. Other methods have also been developed to take advantage of the temporal nature of the electrocardiographic inverse problem, such as using the Twomey regularization [Oster and Rudy 1992], using the structural constraints [Greensite 2003] or using the spatio-temporal multiple regularization scheme [Zhang et al 2005]. Improvement has been reported by using temporal regularization methods. The intrinsic characteristics of the Kalman filter already require the incorporation of temporal

information, and have benefited the present study with smooth inverse results in spatial-temporal domain.

Last, the ill-posedness of the inverse approach has been handled in the predicting procedure. Overcoming the ill-posedness of the inverse problem is critical for obtaining informative and physiological reasonable solutions. Many efforts have been reported. The truncated singular value decomposition method remove the very small singular values to minimize the effect of measurement noise. The popular Tikhonov regularization scheme balances the residual with a measure of some undesirable property of the solution, such as the unreasonable large value of the expected solution. The "critical points" theory determines the activation time at a critical point by looking for the "jump" from the first order derivative of the ECG signals, and such overcomes the ill-posedness [Huiskamp and Greensite 1997]. In the present study, a new regularization scheme has been incorporated into the predicting procedure. The activation time is updated from the estimated activation times in previous step at nearby sites, or at the original site only. The determination is made according to nonlinear criteria (details in equation (7.9)). By using this scheme, the updated activation times in the "correct" procedure is filtered: the oddly large change in the activation times is removed, while the reasonable update is remained. This regularization scheme ensures the convergence of the iteration and at the same time, the useful information obtained in the "correct" procedure is well remained in the updated results.

It worth noting that the EKF is a sub-optimal estimator which utilizes the first-order Taylor series of the system to transfer the nonlinear problem into linear, and the higher-order information is neglected. The efficiency of the EKF depends on the linearity of the system around the true value of the unknown state vector. As results, a high-quality initial value for the iteration can help the convergence to the expected solution. A guess far from the true value may result in incorrect solution. Regarding our problem, that doesn't mean the initial guess of the 3D activation sequence should be fairly accurate at every site; instead, the global pattern is more critical. In the present study, the activation sequence picked up from the inversely estimated equivalent current densities using weighted minimal norm method was used and satisfactory results were reported. On the other hand, the activation times obtained on the heart surface's critical points by using the "critical points" theory may also be a good initial estimate for the EKF approach.

8. Conclusions and future work

8.1. Conclusions

Three-dimensional cardiac functional mapping has great potential for revealing intramural cardiac activities and thus assisting diagnosis and treatment of cardiac arrhythmias. The three-dimensional cardiac electrical imaging (3DCEI) approach has been proposed by He and coworkers [He and Wu 2001, He et al 2002] to estimate the 3D cardiac activity (in the format of equivalent current density, activation sequence, etc) from noninvasive body surface measurement, and the noninvasive estimation of 3D activation sequence has been successfully validated in a rabbit model [Zhang et al 2005; Liu et al 2006a].

Based on the previous work, a new validation study is conducted in a large mammalian animal model (swine), since the pig's cardiac size, heart-torso geometry and electrophysiological characteristics can best approximate those of an adult human. The experimental protocols mimic the clinical settings in every step, and both control and diseased animal models are used. An intracavitary mapping system (Ensite 3000, St Jude Medical Inc.) is employed for the validation of our 3DCEI approach. Promising results are reported regarding the activation sequence and the location of the initiation site. Our results are consistent with the output of the Ensite system. The successful in vivo validation on the large animal suggests that the 3DCEI approach shows robust performance when the clinical settings are mimicked and thus is ready for future studies on real patients.

The function of the 3DCEI approach is further expanded and investigated. First, a new function of localizing the origin of cardiac reentry is developed and evaluated in a simplified heart-torso model, by simulating the reentrant arrhythmia with a focal origin. The results prove that 1) the cardiac reentry and the resultant body surface potentials under ventricular tachycardia/fibrillation can be simulated in a relatively simple heart-torso model with the aid of the ion-channel-level cellular model; 2) the origin of the reentry can be localized from the noninvasively recorded BSPMs within the 3DCEI scheme.

Another exploration is that the finite element method is incorporated into the 3DCEI approach. A direct benefit of using FEM is that the cardiac anisotropy can be incorporated into the numerical calculation and so the accuracy of the forward/inverse calculation could be improved. For instance, the accuracy of localizing the initiation site of activation by 3DCEI approach is expected to be improved in future studies by incorporating the anisotropic information into the inverse approach. Furthermore, by customizing the FEM in the cardiac near-field calculation, we can now estimate the intramural potentials, which have to be obtained by intra-operative recordings before. To our knowledge, this is the first report of estimating the intramural potentials by applying advanced numerical method.

The 3DCEI approach is then further modified to estimate the 3D cardiac activation from the intracavitary potentials maps recorded by a multi-electrode array in the heart chamber. Compared to the noninvasive BSPM-based 3DCEI approach, the intracavitary

recordings are closer to the cardiac sources to be estimated and so more meaningful information could be revealed. In this study, promising results are obtained in both simulation and experimental validation in a control swine model. Since FEM is used, the results of estimated intramural potentials are presented and for the first time validated in animal experiments by comparing to the output of the Ensite system. Both simulation and experimental results suggest that the intracavitary-based 3DCEI approach can reconstruct important electrophysiological properties of cardiac activation and may enhance our ability of mapping focal ventricular arrhythmias.

Different with the heart-model-based 3DCEI approach, a novel inverse algorithm is proposed to estimate the 3D activation sequence from noninvasive BSPMs by using extended Kalman Filter. The new algorithm is evaluated in simulation and shows improved estimation results (compared to the results by using the algorithm proposed in [Liu et al 2006b]) and advanced features, e.g. robustness to measurement noise. This new algorithm represents the latest exploration on the 3D inverse approach. It shows the potential of estimating complex cardiac events and is upon evaluation with animal/human data.

In summary, in the present dissertation study, the three-dimensional cardiac electrical imaging approach has been pushed forward in many aspects including performing validation studies in large animals, expanding its functions on localizing origin of reentry and estimating intramural potentials, refining the approach to estimate 3D cardiac activation alternatively from minimally-invasive intracavitary recordings

(results in both simulation and animal validation presented) and exploring novel algorithm for obtaining high-quality inverse solutions. The present dissertation study proves that the 3DCEI approach is highly promising and has great potential to provide meaningful electrophysiological information for diagnosis and treatment of cardiac arrhythmias.

8.2. Future work

In this thesis study, the three-dimensional cardiac electrical imaging approach has been extensively investigated. In the future investigation of the 3DCEI approach, efforts may be spent on following directions. First, more animal studies as well as human studies are needed to further evaluate and improve the 3DCEI approach. Second, the cardiac fiber orientation may be acquired with the diffusion tensor magnetic resonance imaging (DT-MRI) technique and incorporated into the inverse imaging approach, and the accuracy of the resultant inverse solutions are expected to be improved. Third, the newly proposed algorithm employing extended Kalman filter can be evaluated with physiological data from animal or human.

In conclusion, based on the solid work in the present thesis study, which includes algorithm development, computer simulation and animal validation, it can be foreseen that the three-dimensional ventricular activation imaging will play an important role in guiding the clinical management of cardiac arrhythmias in a more efficient way.

References

[1] Abrams DJ, Earley MJ, Sporton SC, Kistler PM, Gatzoulis MA, Mullen MJ, Till JA, Cullen S, Walker F, Lowe MD, Deanfield JE, Schilling RJ. Comparison of noncontact and electroanatomic mapping to identify scar and arrhythmia late after the Fontan procedure. Circulation 115: 1738-1746, 2007.

[2] Allessie MA, Bonke FI, Schopman FJ. Circus movement in rabbit atrial muscle as a mechanism of tachycardia. II. The role of nonuniform recovery of excitability in the occurrence of unidirectional block, as studied with multiple microelectrodes. *Circ Res* 39: 168–77, 1976.

[3] Antzelevitch C. Basic mechanisms of reentrant arrhythmias Curr Opin Cardiol 16: 1-7, 2001.

[4] Armoundas AA, Feldman AB, Mukkamala R, Cohen RJ. A single equivalent moving dipole model: an efficient approach for localizing sites of origin of ventricular electrical activation. Ann Biomed Eng 31: 564-576, 2003.

[5] Attin M, Ideker RE, Pogwizd SM. Mechanistic insights into ventricular arrhythmias from mapping studies in humans. Heart Rhythm 5(6 Suppl): S53-58, 2008.

[6] Avari JN, Rhee EK. Cardiac resynchronization therapy for pediatric heart failure. Heart Rhythm 5:1476-1478, 2008.

[7] Barr RC, Ramsey M 3rd, Spach MS. Relating epicardial to body surface potential distributions by means of transfer coefficients based on geometry measurements. IEEE Trans Biomed Eng 24:1-11, 1977.

[8] Barr RC, Spach MS. Inverse calculation of QRS-T epicardial potentials from normal and ectopic beats in the dog. Circ. Res., 42:661-675, 1978.

[9] Barber MR, Fischman EJ. Heart dipole regions and the measurement of dipole moment. Nature 192:141-2, 1961.

[10] Beeler GW, Reuter H. Reconstruction of the action potential of ventricular myocardial fiber. J Physiol 268: 177-210, 1977.

[11] Ben-Haim SA, Osadchy D, Schuster I, Gepstein L, Hayam G and Josephson ME. Nonfluoroscopic, in vivo navigation and mapping technology. Nature Med 2: 1393-1395, 1996.

[12] Berger T, Fischer G, Pfeifer B, et al. Single-beat noninvasive imaging of cardiac electrophysiology of ventricular pre-excitation. J Am Coll Cardiol 48:2045-52, 2006.

[13] Berrier KL, Sorensen DC, Khoury DS. Solving the inverse problem of electrocardiography using a Duncan and Horn formulation of the Kalman filter. IEEE Trans. Biomed. Eng. 51: 507–515, 2004.

[14] Chattipakorn N, Fotuhi PC, Chattipakorn SC, Ideker RE. Three-dimensional mapping of earliest activation after near-threshold ventricular defibrillation shocks. J Cardiovasc Electrophysiol 14: 65-69, 2003.

[15] Cheng LK, Bodley JM, Pullan AJ. Comparison of potential- and activation-based formulations for the inverse problem of electrocardiology. IEEE Trans Biomed Eng 50: 11-22, 2003.

[16] Chung MK, Pogwizd SM, Miller DP, Cain Me. Three-dimensional mapping of the initiation of nonsustained ventricular tachycardia in the human heart. Circulation 95: 2517–2527, 1997.
[17] Cuppen JJM, Van Oosterom A. Model studies with inversely calculated isochrones of ventricular depolarization. IEEE Trans Biomed Eng 31:652-659, 1984.
[18] Dong J, Calkins H, Solomon SB, Lai S, Dalal D, Lardo AC, Brem E, Preiss A, Berger RD, Halperin H, Dickfeld T. Integrated electroanatomic mapping with three-dimensional computed tomographic images for real-time guided ablations. Circ 113:186-194, 2006.
[19] El-Jakl J, Champagnat F, Goussard Y. Time-space regularization of the inverse problem of electrocardiography. in Proc 17th Ann Int Conf IEEE EMBS, Montréal, QC, Canada, 213–214, 1995.
[20] Fischer A. Optimization techniques in cardiac resynchronization therapy. Future Cardiol 5: 355-65, 2009.
[21] Fischer G, Tilg B, Modre R, Huiskamp G, Fetzer J, Rucker W, Wach P. A bidomain model based BEM-FEM coupling formulation for anisotropic cardiac tissue. Ann Biomed Eng 28: 1229-1243, 2000.
[22] Frazone PC, Taccardi B, Viganotti C. An approach to the inverse calculation of epicardial potentials from body surface maps. Adv Cardiol 21: 50-4, 1978.
[23] Gepstein L, Hayam G, Ben-Haim SA. A novel method for nonfluoroscopic catheter-based electroanatomical mapping of the heart: in vitro and in vivo accuracy results. Circulation 95: 1611-1622, 1997.
[24] Geselowitz DB, Miller WT. A bidomain model for anisotropic cardiac muscle. Ann Biomed Eng 11:191-206, 1983.
[25] Gornick CC, Adler SW, Pederson B, Hauck J, Budd J, Schweitzer J. Validation of a new noncontact catheter system for electroanatomic mapping of left ventricular endocardium. Circulation 99: 829-835, 1999.
[26] Greensite F. Remote reconstruction of confined wavefront propagation. Inv Prob 11:361-70, 1995.
[27] Greensite F, Huiskamp G. An improved method for estimating epicardial potentials from the body surface. IEEE Trans. Biomed. Eng., 45:98-104, 1998.
[28] Greensite F. The temporal prior in bioelectromagnetic source imaging problems. IEEE Trans Biomed Eng 50: 1152–1159, 2003.
[29] Greensite F. Heart surface electrocardiographic inverse problem. In He B(Ed): Modeling and Imaging of Bioelectric Activity Principles and Applications, Kluwer Academic / Plenum Publishers, 2004.
[30] Gulrajani RM, Roberge FA, Savard P. Moving dipole inverse ECG and EEG solutions. IEEE Trans. Biomed. Eng., 31:903-910, 1984.
[31] Han C, Liu Z, Zhang X, et al. Noninvasive three-dimensional cardiac activation imaging from body surface potential maps: a computational and experimental study on a rabbit model. IEEE Trans Med Imaging 27:1622-30, 2008.
[32] Hansen PC. Analysis of discrete ill-posed problems by means of the L-curve. SIAM Rev 34:561-80, 1992.

[33] He B, Wu D. Imaging and visualization of 3-D cardiac electric activity. IEEE Trans Inf Technol Biomed 5:181-86, 2001.
[34] He B, Li G, Zhang X. Noninvasive three-dimensional activation time imaging of ventricular excitation by means of a heart-excitation model. Phys Med Bio 47:4063-78, 2002.
[35] He B, Li G, and Zhang X. Noninvasive imaging of cardiac transmembrane potentials within three-dimensional myocardium by means of a realistic geometry anisotropic heart model. IEEE Trans Biomed Eng 50: 1190-1202, 2003.
[36] Helm RH, Byrne M, Helm PA, Daya SK, Osman NF, Tunin R, Halperin HR, Berger RD, Kass DA, Lardo AC. Three-dimensional mapping of optimal left ventricular pacing site for cardiac resynchronization. Circulation 115: 953-961, 2007.
[37] Huiskamp G, Greensite F. A new method for myocardial activation imaging. IEEE Trans Biomed Eng 44:433-46, 1997.
[38] Ideker RE, Bandura JP, Cox JW Jr, et al. Path and significance of heart vector migration during QRS and ST-T complexes of ectopic beats in isolated perfused rabbit hearts. Circ Res 41:558-64, 1977.
[39] Jia P, Ramanathan C, Ghanem RN, et al. Electrocardiographic imaging of cardiac resynchronization therapy in heart failure: observation of variable electrophysiologic responses. Heart Rhythm 3:296-310, 2006.
[40] Joly D, Goussard Y, Savard P. Time-recursive solution to the inverse problem of electrocardiography: A model-based approach. in Proc 15th Ann Int Conf IEEE EMBS, San Diego, CA, 767–768, 1993.
[41] Josephson ME, Horowitz LN, Farshidi A, Kastor JA. Recurrent sustained ventricular tachycardia, I: mechanisms. Circulation 57: 431-9, 1978.
[42] Khoury DS, Taccardi B, Lux RL, Ershler PR, Rudy Y. Reconstruction of endocardial potentials and activation sequences from intracavitary probe measurements. Localization of pacing sites and effects of myocardial structure. Circulation 91: 845-863, 1995.
[43] Khoury DS, Berrier KL, Badruddin SM, Zoghbi WA. Three-dimensional electrophysiological imaging of the intact canine left ventricle using a noncontact multielectrode cavitary probe: study of sinus, paced, and spontaneous premature beats. Circulation 97:399-409, 1998.
[44] Kim S, Kim TS, Zhou Y, Singh M. Influence of conductivity tensors on the scalp electrical potential: study with 2-D finite element models. IEEE Trans Nuclear Science 50: 133-139, 2003.
[45] Kowalik J, Osborne MR. Methods for uniconstrained optimization problems *Elsevier* New York 24-7, 1968.
[46] Kozinska D, Tretiak OJ, Nissanov J, Ozturk C. Multidimensional alignment using the euclidean distance transform. Graphical Models and Image Processing 59:373-387, 1997.
[47] Laske TG, Skadsberg ND, Hill AJ, Klein GJ, Iaizzo PA. Excitation of the intrinsic conduction system through his and intraventricular septal pacing. Pacing Clin Electrophysiol 29:397-405, 2006.

[48] Li G, He B. Localization of the site of origin of cardiac activation by means of a heart-model-based electrocardiographic imaging approach. IEEE Trans Biomed Eng 48:660-669, 2001.
[49] Li G, Zhang X, Lian J, He B. Noninvasive localization of the site of origin of paced cardiac activation in human by means of a 3-D heart model," IEEE Trans Biomed Eng 50: 1117-1120, 2003.
[50] Liu C, Li G, He B. Localization of site of origin of reentrant arrhythmia from BSPMs: a model study. Physics in Medicine and Biology 50: 1421-1432, 2005.
[51] Liu C, Zhang X, Liu Z, Pogwizd SM, He B. Three-dimensional myocardial activation imaging in a rabbit model IEEE Trans Biomed Eng 53:1813-1820, 2006a.
[52] Liu C, Skadsberg N, Ahlberg S, Swingen C, Iaizzo P, He B. Estimation of global ventricular activation sequences by noninvasive 3-dimensional electrical imaging: validation studies in a swine model during pacing. Journal of Cardiovascular Electrophysiology 19: 535-540, 2008.
[53] Liu Z, Liu C, He B. Noninvasive reconstruction of three-dimensional ventricular activation sequence from the inverse solution of distributed equivalent current density. IEEE Trans Med Imaging 25:1307-1318, 2006b.
[54] Lorange M, Gulrajani RM. A computer heart model incorporating anisotropic propagation. I. Model construction and simulation of normal activation. J Electrocardiol 26: 245-261, 1993.
[55] Malmivuo J, Plonsey R. Bioelectromagnetism - principles and applications of bioelectric and biomagnetic fields *Oxford University Press* New York, 1995.
[56] Maybeck PS. Stochastic models, estimation and control volume 1. Academic press, 1979.
[57] Miller WT, Geselowitz DB. Simulation studies of the electrocardiogram. I. The normal heart. Circ Res 43: 301–315, 1978.
[58] Mirvis DM, Keller FW, Ideker RE, Cox JW, Dowdie RJ, Zettergren DG. Detection and localization of multiple epicardial electrical generators by a two-dipole ranging technique. Circ Res 41:551-557, 1977.
[59] Mittal S. "Focal" ventricular tachycardia: insights from catheter ablation. Heart Rhythm 5(6 Suppl): S64-S67, 2008.
[60] Modre R, Seger M, Fischer G, Hintermüller C, Hayn D, Pfeifer B, Hanser F, Schreier G, Tilg B. Cardiac anisotropy: is it negligible regarding noninvasive activation time imaging? IEEE Trans Biomed Eng 53: 569-580, 2006.
[61] Moe GK, Rheinboldt WC, Abildskov JA. A computer model of atrial fibrillation Am Heart J 67: 200-220, 1964.
[62] Myerburg RJ, Dessler KM Castellanos A. Sudden Cardiac Death: Epidemiology, Transient Risk, and Intervention Assessment, Ann. Intern. Med., 119: 1187-1197, 1993.
[63] Nenonen J, Edens J, Leon LJ, Horacek BM. Computer model of propagated excitation in the anisotropic human heart: I. Implementation and algorithms. In: Computer in Cardiology, IEEE Society Press Los Alamitos, 545-548, 1991.

[64] Ohyu S, Okamoto Y, Kuriki S. Use of the ventricular propagated excitation model in the magnetocardiographic inverse problem for reconstruction of electrophysiological properties. IEEE Trans Biomed Eng 49: 509-19, 2002.
[65] Okamoto Y, Teramachi Y, Musha T. Limitation of the inverse problem in body surface potential mapping. IEEE Trans Biomed Eng 30: 749-754, 1983.
[66] Oster HS, Rudy Y. The use of temporal information in the regularization of the inverse problem of electrocardiography. IEEE Trans Biomed Eng 39: 65–75, 1992.
[67] Oster HS, Taccardi B, Lux RL, et al. Noninvasive electrocardiographic imaging: reconstruction of epicardial potentials, electrograms, and isochrones and localization of single and multiple electrocardiac events. Circulation 96:1012-24, 1997.
[68] Parson I, Downar E. Clinical instrumentation for the intra-operative mapping of ventricular arrhythmias. Pacing Clin Electrophysiol 7: 683-92, 1984.
[69] Ramanathan C, Raja NG, Jia P, et al. Noninvasive electrocardiographic imaging for cardiac electrophysiology and arrhythmia. Nature Medicine 10:422-8, 2004.
[70] Ramanathan C, Jia P, Ghanem RN, et al. Activation and repolarization of the normal human heart under complete physiological conditions. Proc Nat Acad Sci U S A 103:6309-14, 2006.
[71] Savard P, Roberge FA, Perry J, Nadeau RA. Representation of cardiac electrical activity by a moving dipole for normal and ectopic beats in the intact dog. Circ Res., 46:415-425, 1980.
[72] Schilling RJ, Peters NS, Davies DW. Simultaneous endocardial mapping in the human left ventricle using a noncontact catheter: comparison of contact and reconstructed electrograms during sinus rhythm. Circulation 98: 887-898, 1998.
[73] Shahidi AV, Savard P, Nadeau R. Forward and inverse problems of electrocardiography: modeling and recovery of epicardial potentials in humans. IEEE Trans Biomed Eng 41:249-256, 1994.
[74] Skipa O, Sachse NF, Werner C, Dossel O. Transmembrane potential reconstruction in anisotropic heart model. Int J of Bioelectromagnetism 4: 17-8, 2002.
[75] Stevenson WG, Khan H, Sager P, Saxon LA, Middlekauff HR, Natterson PD, Wiener I. Identification of reentry circuit sites during catheter mapping and radiofrequency ablation of ventricular tachycardia late after myocardial infarction. Circulation 88: 1647-70, 1993.
[76] Taccardi B, Macchi E, Lux RL, Ershler PR, Spaggiari S, Baruffi S, Vyhmeister Y. Effect of myocardial fiber direction on epicardial potentials. Circulation 90: 3076-3090, 1994.
[77] Throne RD, Olson LG. A generalized eigensystem approach to the inverse problem of electrocardiography. IEEE Trans Biomed Eng 41: 592-600, 1994.
[78] Tilg B, Fischer G, Modre R, et al. Model-based imaging of cardiac electrical excitation in humans. IEEE Trans Med Imaging 21:1031-39, 2002.
[79] Velipasaoglu EO, Sun H, Zhang F, Berrier KL, Khoury DS. Spatial regularization of the electrocardiographic inverse problem and its application to endocardial mapping. IEEE Trans Biomed Eng 47 :327-337, 2000.

[80] Wei D, Okazaki O, Harumi K, Harasawa E, Hosaka H. Comparative simulation of excitation and body surface electrocardiogram with isotropic and anisotropic computer heart models. IEEE Trans. Biomed. Eng 42: 343-357, 1995.
[81] Witkowski FX, Corr PB. An automated simultaneous transmural cardiac mapping system. Am J Physiol 247: H661-668, 1984.
[82] Yan Y, Nunez PL, Hart RT. Finite-element model of the human head: scalp potentials due to dipole sources. Medical & Biological Engineering & Computing 29: 475-481, 1991.
[83] Zhang S, Skinner JL, Sims AL, Rollins DL, Walcott GP, Smith WM, Ideker RE. Three-dimensional mapping of spontaneous ventricular arrhythmias in a canine thrombotic coronary occlusion model. J Cardiovasc Electrophysiol 11: 762-772, 2000.
[84] Zhang X, Ramachandra I, Liu Z, Muneer B, Pogwizd SM, He B. Noninvasive three-dimensional electrocardiographic imaging of ventricular activation sequence. Am J Physiol Heart Circ Physiol 289: H2724-2732, 2005.
[85] Zhang Y, Ghodrati A, Brooks DH. An analytical comparison of three spatio-temporal regularization methods for dynamic linear inverse problems in a common statistical framework. Inverse Problems 21: 357–382, 2005.
[86] Zhang Y, Zhu S, He B. A second-order finite element algorithm for solving the three-dimensional EEG forward problem. Phys Med Biol 49: 2975-2987, 2004.